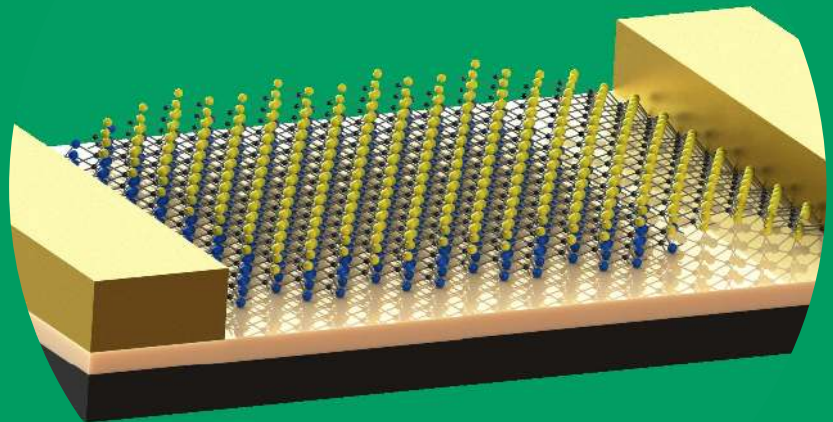


Fabrication of Optoelectronic Devices with Two-dimensional Layered Materials and Their Heterostructures

Hui Xue



Fabrication of Optoelectronic Devices with Two-dimensional Layered Materials and Their Heterostructures

Hui Xue

A doctoral dissertation completed for the degree of Doctor of Science (Technology) to be defended, with the permission of the Aalto University School of Electrical Engineering, at a public examination held at the Large Seminar Hall of Micronova on 17th of January 2020 at 12:00.

**Aalto University
School of Electrical Engineering
Department of Electronics and Nanoengineering
Photonics Group**

Supervising professor

Professor Kari Halonen, Aalto University, Finland

Thesis advisor

Professor Zhipei Sun, Aalto University, Finland

Preliminary examiners

Professor Matthieu Roussey, University of Eastern Finland, Finland

Professor Weida Hu, Shanghai Institute of Technical Physics, PRC China

Opponent

Professor Alberto G. Curto, Eindhoven University of Technology, Netherlands

Aalto University publication series

DOCTORAL DISSERTATIONS 1/2020

© 2020 Hui Xue

ISBN 978-952-60-8894-5 (printed)

ISBN 978-952-60-8895-2 (pdf)

ISSN 1799-4934 (printed)

ISSN 1799-4942 (pdf)

<http://urn.fi/URN:ISBN:978-952-60-8895-2>

Unigrafia Oy

Helsinki 2020

Finland



Author

Hui Xue

Name of the doctoral dissertation

Fabrication of Optoelectronic Devices with Two-dimensional Layered Materials and Their Heterostructures

Publisher School of Electrical Engineering

Unit Department of Electronics and Nanoengineering

Series Aalto University publication series DOCTORAL DISSERTATIONS 1/2020

Field of research Photonics

Manuscript submitted 7 August 2019

Date of the defence 17 January 2020

Permission for public defence granted (date) 29 November 2019

Language English

☐ **Monograph**

☒ **Article dissertation**

☐ **Essay dissertation**

Abstract

This thesis focuses on the fabrication of two-dimensional (2D) layered materials-based devices for optoelectronic applications, such as graphene-based modulators, WSe₂/MoSe₂ heterojunction and WSe₂/SnSe₂ heterojunction-based photodetectors. The thesis is divided into five parts. The first part gives an overview of the potential applications of 2D layered materials and their heterostructures in the field of optoelectronics. The second part introduces the fundamental properties of 2D layered materials, including graphene, transition metal dichalcogenides, and their van der Waals heterojunctions. The third part discusses the process methods that have been used for fabrication of optoelectronic devices. For example, mechanical exfoliation and chemical vapor deposition methods are used to obtain 2D layered materials, and electron beam lithography, atomic layer deposition and reactive ion etching are the most important methods during the device processing. The fourth part introduces the characterization methods of the fabricated devices. For example, Raman and photoluminescence spectroscopies are used to characterize the 2D layered materials, and Atomic force microscope is used to check the thickness of the exfoliated 2D layered material flakes. The electrical and photocurrent measurements are also presented for characterization of device performance. The fifth part presents the optoelectronic applications of the fabricated devices. First, two different kinds of graphene-based modulators are presented. Then, we demonstrate the WSe₂/MoSe₂ and WSe₂/SnSe₂ heterojunctions-based photodetectors with broadband photodetection and high photoresponsivity. Finally, I summarize the whole contents and give the outlook on the applications of the 2D layered materials-based optoelectronics.

Keywords Two-dimensional layered materials, van der Waals heterojunction, photodetectors, modulators

ISBN (printed) 978-952-60-8894-5

ISBN (pdf) 978-952-60-8895-2

ISSN (printed) 1799-4934

ISSN (pdf) 1799-4942

Location of publisher Helsinki

Location of printing Helsinki **Year** 2020

Pages 117

urn <http://urn.fi/URN:ISBN:978-952-60-8895-2>

Preface

The works present in this thesis were carried out in the photonics group of the Department of Electronics and Nanoengineering, School of Electrical Engineering, Aalto University, between 2014 and 2018. I still remember the autumn, Oct. 2013, when I first arrived in Finland. Everything was new to me, and I knew only a little about semiconductor physics and microfabrication skills. After several years, I have learned and gained a lot, not only knowledge about physics but also experimental ability. I must thank those people without whom this thesis would never be ready.

Firstly, I would like to thank Prof. Zhipei Sun, for giving me the opportunity to work in his group. He is an excellent supervisor by offering me the flexible working hours, nice working environment, funding for daily life and the cost of the cleanroom. He also gives me many supports and motivations on my way of doing scientific research. Then I would like to thank Prof. Kari Halonen who is my supervisor for helping me with my enrolment at Aalto University. I also need to acknowledge Dr. Henri Jussila for guiding me into the world of the semiconductor and teaching me by using the atomic force microscope. I will never forget the days when we were discussing my first paper and conducting the Kelvin probe force microscopy measurement. Dr. Yunyun Dai is acknowledged for guiding me after Henri left the group. Without her, my second paper will take longer time than expected.

Then I would like to thank Dr. Wonjae Kim for the guiding me of the nanofabrication when I was a beginner and great discussions about the characterizations of the fabricated devices. Yadong Wang who is the co-first author of my first paper should also be acknowledged. Without him, the setup at the telecommunication wavelength will never be made. I need to thank Xueyin Bai who helps me measure the thickness and the Raman spectrum when I was busy with writing the thesis.

In addition, I need to deeply thank other collaborators, Prof. Xiaomu Wang, Prof. Xuetao Gan, Prof. Tony Low, Prof. Harri Lipsanen, Prof. Ilkka Tittonen, Prof. Yixuan Zhou, Dr. Jannatul Susoma, Dr. He Yang, Dr. Nan Wei, Dr. Diao Li, Dr. Alexander Christian Pyymaki Perros, Dr. Ya Chen, Dr. Sami Kujala, Dr. Bo Fu, Dr. Luke Baker, Dr. Luojun Du, Dr. Minde Du, Libin Wang, John Ronn, Huan Wang, Hao Wu and Xuerong Hu. Thanks for all your contributions to discussion, data analyzing, measurements, as well as suggestions.

Finally, I would like to thank my parents for their encouragement, support, and everlasting love.

Espoo, July 30, 2019,
Hui Xue

Contents

- Preface 1**
- Contents2**
- List of Abbreviations.....5**
- List of Symbols.....7**
- List of Publications9**
- Author’s Contribution 10**
- 1. Introduction11**
- 2. Fundamentals of two-dimensional layered materials . 13**
 - 2.1 Graphene 13
 - 2.2 Transition metal dichalcogenides..... 15
 - 2.3 Heterojunctions 18
- 3. Fabrication of two-dimensional layered materials-based devices 20**
 - 3.1 Two-dimensional material synthesis methods.....20
 - 3.1.1 Mechanical exfoliation.....20
 - 3.1.2 Chemical vapor deposition 21
 - 3.1.3 Other synthesis methods 21
 - 3.2 Device fabrication 23
- 4. Characterization of two-dimensional layered materials-based devices 27**
 - 4.1 Atomic force microscope 27
 - 4.2 Raman spectroscopy.....28
 - 4.3 Photoluminescence spectroscopy.....30
 - 4.4 Electrical measurement..... 31
 - 4.5 Photocurrent measurement.....33
- 5. Optoelectronic devices with two dimensional layered materials and their heterostructures36**
 - 5.1 Graphene based modulators.....36
 - 5.2 Transition metal dichalcogenide heterostructures based photodetectors39
 - 5.2.1 WSe₂/MoSe₂ heterojunction based photodetector40

5.2.2	WSe ₂ /SnSe ₂ heterojunction based photodetector.....	46
6.	Summary and outlook.....	52
References	55

List of Abbreviations

2D	Two-dimensional
AFM	Atomic force microscope
ALD	Atomic layer deposition
APS	Ammonium persulfate
CCDs	Charge-coupled devices
CMOS	Complementary metal-oxide-semiconductor
CR	Contact resistance
CVD	Chemical vapor deposition
DFT	Density functional theory
DI	Deionized
EBL	Electron beam lithography
FETs	Field-effect-transistors
FWHM	Full width at half maximum
GEOMs	Graphene electro-optic modulators
h-BN	Hexagonal boron nitride
IPA	Isopropanol
LED	Light-emitting diodes
MBE	Molecular beam epitaxy
MoS ₂	Molybdenum disulfide
MoSe ₂	Molybdenum diselenide
NIR	Near-infrared
PDMS	Polydimethylsiloxane
PL	Photoluminescence
PVD	Physical vapor deposition

RIE	Reactive ion etching
SnSe ₂	Tin diselenide
TDMAH	Tetrakis (dimethylamino) hafnium
TFET	Tunnelling field effect transistors
TLM	Transfer length method
TMDs	Transition metal dichalcogenides
vdW	van der Waals
WSe ₂	Tungsten diselenide

List of Symbols

A	Fractional absorbance
c	Speed of light
C_i	Capacitance between flakes and the gate per unit area
D	Detectivity
dB	Decibel
e	Charge of the electron
E	Energy
E_f	Fermi level
E_{fm}	Fermi level of metal
E_{fs}	Fermi level of semiconductor
EQE	External quantum efficiency
G	Photo gain
\hbar	Planck constant
I_d	Drain to source current
I_{dark}	Dark current
I_{total}	Total current measured under the incident light
I_{ph}	Photocurrent
k	Wave vector
L	Channel length
n_e	Photon-excited carriers
n_s	Refractive index of the substrate
n_{total}	Total incident photon flux
NPDR	Normalized photocurrent-to-dark current ratio
P_{laser}	Incident laser power
R	Responsivity

R_c	Contact resistance
R_{ch}^s	Sheet resistance
R_s	Reflectance of the substrate
R_{total}	Total contact resistance
R_{TMD+s}	Reflectance of the TMDs on the substrate
t	Optical path
V_{BB}	Degree of the band bending
V_d	Drain to source voltage
V_F	Fermi velocity
V_g	Gate voltage
W	Channel width
$\Delta R/R$	Reflectance contrast spectra
α	Absorption coefficient
Γ	Absorbed number of photons per unit time
η	Efficiency of conversion of the absorbed photons to electrons
λ	Wavelength
μ	Mobility
$\tau_{carrier}$	Carrier lifetime
$\tau_{transit}$	Transit time
ν	Frequency of the incident light
ϕ_m	Metal work function
ϕ_s	Semiconductor work function
ϕ_{SB}	Schottky barrier
χ_s	Electron affinity of the semiconductor

List of Publications

This doctoral dissertation consists of a summary of the following publications which are referred to in the text by their numerals

1. Hui Xue, Yunyun Dai, Wonjae Kim, Yadong Wang, Xueyin Bai, Mei Qi, Kari Halonen, Harri Lipsanen, and Zhipei Sun. High photoresponsivity and broadband photodetection with a band-engineered WSe₂/SnSe₂ heterostructure, *Nanoscale*, vol. 11, pp.3240-3247, 2019.

2. Hui Xue, Yadong Wang, Yunyun Dai, Wonjae Kim, Henri Jussila, Mei Qi, Jannatul Susoma, Zhaoyu Ren, Qing Dai, Jianlin Zhao, Kari Halonen, Harri Lipsanen, Xiaomu Wang, Xuetao Gan, and Zhipei Sun. A MoSe₂/WSe₂ Heterojunction-Based Photodetector at Telecommunication Wavelengths. *Advanced Functional Materials*. vol. 28, pp. 1804388, 2018.

3. Jakub Bogusławski, Yadong Wang, **Hui Xue**, Xiaoxia Yang, Dong Mao, Xuetao Gan, Zhaoyu Ren, Jianlin Zhao, Qing Dai, Grzegorz Sobon, Jarosław Sotor, and Zhipei Sun. Graphene Actively Mode-Locked Lasers. *Advanced Functional Materials*, vol. 28, no. 28, pp. 1801539, 2018.

4. Wonjae Kim, Sanna Arpiainen, **Hui Xue**, Miika Soikkeli, Mei Qi, Zhipei Sun, Harri Lipsanen, Ferney A. Chaves, David Jiménez, and Mika Prunnila. Photoresponse of Graphene-Gated Graphene-GaSe Heterojunction Devices. *ACS Applied Nano Materials*. vol. 1, no. 8, pp. 3895-3902, 2018.

5. Diao Li, **Hui Xue**, Yadong Wang, Mei Qi, Wonjae Kim, Changfeng Li, Juha Riikonen, Zhaoyu Ren, Jintao Bai, Harri Lipsanen, and Zhipei Sun, Active synchronization and modulation of fiber lasers with a graphene electro-optic modulator, *Optics Letters*, vol. 43, no. 15, pp. 3497-3500, 2018.

6. Diao Li, **Hui Xue**, Mei Qi, Yadong Wang, Sinan Aksimsek, Nikolai Chekurov, Wonjae Kim, Changfeng Li, Juha Riikonen, Fangwei Ye, Qing Dai, Zhaoyu Ren, Jintao Bai, Tawfique Hasan, Harri Lipsanen, and Zhipei Sun. Graphene actively Q-switched lasers. *2D Materials*. vol. 4, no. 2, pp. 025095, 2017.

Author's Contribution

Publication 1: High photoresponsivity and broadband photodetection with a band-engineered $\text{WSe}_2/\text{SnSe}_2$ heterostructure

The author wrote the manuscript of this publication. The author designed the experiment, fabricated the device and did all characterization and measurement.

Publication 2: High-sensitivity broadband photodetector with $\text{MoSe}_2/\text{WSe}_2$ van der Waals heterojunction at telecommunication wavelength

The author wrote the manuscript of this publication. The author designed the experiment, fabricated the device and did all characterization and measurement.

Publication 3: Graphene Actively Mode-Locked Lasers

The author designed and fabricated the graphene modulator.

Publication 4: Photoresponse of Graphene-Gated Graphene-GaSe Heterojunction Devices.

The author contributed to the manuscript preparation and did the photoresponse characterizations of the device at 730, 1330 and 1550 nm.

Publication 5: Active synchronization and modulation of fiber lasers with a graphene electro-optic modulator

The author fabricated the graphene modulator. The author also conducted the electrical characterization of the graphene modulator.

Publication 6: Graphene actively Q-switched lasers

The author fabricated the graphene modulator. The author also conducted the electrical characterization of the graphene modulator. The author also contributed to the manuscript preparation.

1. Introduction

Graphene, the first isolated two-dimensional (2D) layered material in 2004, has drawn unprecedented attention due to the new applications enabled by its prominent physical properties.[1, 2] The high Young's modulus (1 Tpa for defect-free graphene [3]) and excellent thermal conductivity (5000 W/mK at room temperature [4]) make graphene as a potential candidate for the next-generation electronics.[5, 6] Especially in the fields of photonics and optoelectronics, graphene offers several advantages compared with other materials.[7, 8] For example, it has excellent electrical conductivity, high transparency and flexibility.[9] In this manner, it is a promising candidate as the replacement of indium tin oxide which is widely used for displays and touchscreens but not applicable in flexible devices.[10, 11] Also, The gapless nature of graphene also yields another promising future in optoelectronics. It is widely known that each traditional semiconductor typically has a transparency window to the light with photon energy smaller than its intrinsic bandgap. In this case, the zero-bandgap nature of graphene results in its extremely broadband absorption, i.e., from ultraviolet to the microwave regions, which has been utilized in many optoelectronic devices, such as ultrafast lasers, modulators, and photodetectors.[12-51]

Besides graphene, layered transition metal dichalcogenides (TMDs), another kind of 2D layered materials, are also extensively studied. Atoms within each layer are held together by the covalent bonds, and each layer is bonded together by van der Waals (vdW) interactions.[52] The diversity and tunability of the band structures of TMDs, covering the semiconducting to the metallic range, suggest them to be a powerful platform for building various functional devices.[53] The significant properties of TMDs different from graphene are their possible sizeable bandgap. As semiconductors with non-zero band gap, TMDs based field-effect-transistors (FETs) with high on-off ratio have been demonstrated, offering a new material platform for electronics.[54, 55]

Moreover, due to the quantum confinement effect, the band structure of TMDs can transit from indirect bandgap to direct bandgap when they become thinner from the bulk to the monolayer, which results in significantly strong photoluminescence (PL) in monolayer TMDs compared with their bulk counterparts.[53] This excellent property makes TMDs significantly different from their bulk counterparts in electronic, optical, thermal and mechanical properties. Comparing with graphene which shows absorption of 2.3% in visible and near-infrared (NIR) spectral range, monolayer TMDs can exhibit much higher absorption at the excitonic resonances (>10%).[56] Such strong light-matter interaction, as well as the sizable bandgap and mechanical flexibility, make TMDs promising for a large range of optoelectronic applications.[57-77]

van der Waals heterostructures, in which different 2D layered materials are stacked laterally or vertically together, not only overcome the inherent limitations of the composed materials

but also provide novel properties and offer another avenue for assembling high-performance photonic devices.[58, 78, 79] Different with those conventional semiconductor heterostructures which require similar lattice structure, the vdW heterostructures typically are covalently bonded in-plane and held together out-of-plane by vdW force, which are easily exfoliated and transferred to arbitrary substrates or stacked together to form the heterojunctions despite lattice mismatch.[80] Moreover, the big family of 2D layered materials which have various carrier densities and electron affinities allows us to select the desired band alignments to meet the need of the photonic devices.[81, 82] Depending on their energy band alignments, the vdW heterojunctions can be classified into three types: straddling gap (type-I), the staggered gap (type-II) and broken gap (type-III).[83] The type-I heterojunctions are usually utilized in light emitting diode (LED) devices as for their fast recombination rate of electrons and holes, type-II heterojunctions are the building blocks for many photovoltaic devices, while for type-III heterojunctions, they are desirable for designing field effect transistors.[84, 85] An excellent application example of vdW heterojunctions is the photodetection. Owing to the high efficiency of photon-excited carrier generation and collection, the vdW heterojunction based photodetectors with TMDs exhibit not only high photoresponsivity and detectivity but also the increased speed of the response.[86-90] Specifically, by properly gating and biasing the device, the broadband photodetection can be achieved.[91] All these remarkable properties suggest them for implementing novel electronic and optoelectronic devices.

In this thesis, various graphene, TMDs and their heterostructures based optoelectronic devices are presented in the following way: Chapter 2 briefly reviews the fundamentals of 2D layered materials, i.e., the structure, electrical and optical properties of graphene, TMDs, and their heterostructures. The material synthesis methods of 2D layered materials (such as mechanical exfoliation and chemical vapor deposition (CVD)) and the device process methods (i.e., electron beam lithography, atomic layer deposition, and reactive-ion etching) of TMDs based optoelectronic devices are introduced in Chapter 3. The characterization methods and tools for 2D layered materials and their devices are presented in Chapter 4. Afterward, the most crucial part of the thesis, the 2D layered materials-based optoelectronics devices, i.e., graphene-based modulators, and TMD heterojunctions based broadband photodetectors, are discussed in Chapter 5. Chapter 6 summarizes the work and outlooks 2D layered materials-based optoelectronics.

2. Fundamentals of two-dimensional layered materials

2D layered materials have been intensively studied as the ideal candidates for future optoelectronics devices, due to their unique properties. In this chapter, we introduce the band structure, optical properties and the electrical properties of graphene, TMDs as well as heterojunctions. In addition, potential applications for photonics devices are discussed in brief.

2.1 Graphene

Graphene, a crystalline allotrope of the carbon, is a building block for graphitic materials of many different dimensionalities, such as 0-dimensional (D) fullerenes, 1D nanotubes and 3D graphite (Figure 2.1).[1] Although graphite has been widely used for writing since it was discovered in the 16th century, the 2D graphite (graphene), was presumed not to exist, due to the thermodynamical instability.[92] Whereas, in 2004, the conventional wisdom was flaunted by the first discovery of graphene by utilizing the Scotch-tape method from its bulk graphite. In graphite, each graphene layer is connected by the vdW force with a distance of 0.34 nm, and atoms within each graphene layer are bonded covalently.[93] Since the vdW force is much weaker than the interatomic bonding, once the graphite is scratched, the exfoliated graphene can be easily transferred to the target substrates.

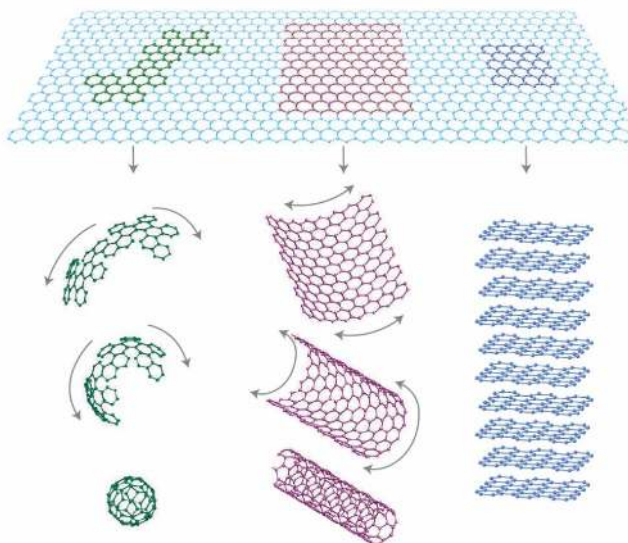


Figure 2.1. Graphene can be wrapped into 0D fullerenes, 1D nanotubes, and 3D graphite.[1]

Graphene is made of hexagon honeycomb carbon structure with a C-C bond length of 1.42 Å, as shown in Figure 2.2 (a).[94] The structure of graphene lattice can be seen as a triangular lattice with two atoms per unit cell (Figure 2.2 (b)).[94] The high-symmetry points k and k' which at the corners of the graphene Brillouin zone are quite important. Near these two points, the bands show a linear dependence of electronic energy to the wave vector. The k and k' are known as charge neutral points (Dirac point), where the conduction band and valence band of graphene meet each other (Figure 2.2(c)), suggesting the zero bandgap nature of graphene.[94] This zero bandgap results in graphene as a promising material for broadband applications. However, the zero bandgap also hinders its application in the field of field-effect transistors, i.e., graphene-based FETs always show large switch-off current. To overcome this shortcoming, several attempts have been made, such as applying strain to graphene, biasing double-layer graphene or put quantum dots on graphene.[2, 95-97] Electrons in graphene behave as massless Dirac fermions, which follow the equation $E = \hbar k v_F$, where E is the energy spectrum, \hbar is the plank constant, k is the wave vector and v_F is the Fermi velocity ($v_F \approx c/300$, c is the speed of light).[94] This indicates the ballistic transport of electrons in graphene moving with a constant velocity. In the defect-free graphene, the recorded mobility of exfoliated suspended layer of graphene reaches 200,000 cm²/Vs.[98] These values are much exceeding those of transitional semiconductors, such as silicon.

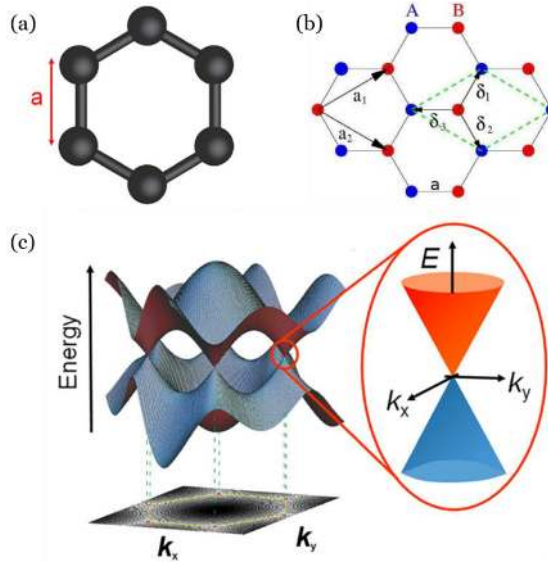


Figure 2.2. (a) Honeycomb lattice of graphene. a is the C-C bond length (b) The lattice structure of graphene. a_1 and a_2 are the lattice unit vectors, and δ_1 , δ_2 and δ_3 are the nearest-neighbour vectors. (c) Electronic dispersion in the honeycomb lattice. Left: The 3D bandstructure of graphene. Right: zoom in of the energy bands close to one of the Dirac points. [94, 99]

Another distinguishing feature of graphene is its ambipolar electric field effect, which means the type of carrier can be controlled through an external electric field (see Figure 2.3).[1, 94] A positive gate voltage (V_g) raises the Fermi level (E_F) above the Dirac point by propelling the electrons to the conduction band, while a negative V_g pulls down the E_F below the Dirac point by promoting the holes in the valence band. Beneficial from the excellent carrier mobility and ambipolar transport property, graphene has been widely explored in high-speed electronic devices.[100]

Due to its gapless nature, graphene can absorb photons in a wide spectral range, e.g., from ultraviolet (UV) to terahertz (THz) regions. Figure 2.4. shows two photo-excitation modes: interband transition and intraband transition.[101] If the energy of the incident photon is larger than $|2E_F|$, the electron will be excited to the conduction band, and the hole will be created in the valence band. This process is dominated by the interband transition. Thus, as has been mentioned, by applying an external electric field, the E_F of graphene can be tuned, which will result in the adjustable absorption in graphene. This outstanding property shows the potential for utilizing the graphene as the optical modulators, which will be discussed in Chapter 5.

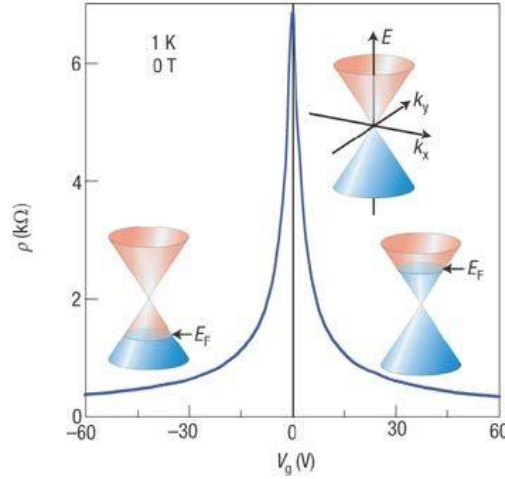


Figure 2.3. Ambipolar electric field effect in graphene. The insets show the low-energy dispersion of graphene, where the external V_g can efficiently modify the position of the E_F . [1]

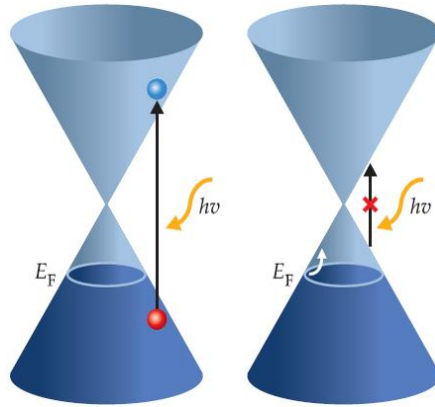


Figure 2.4. Illustration of the various optical transition processes. Left: interband transition and right: intraband transition. [101]

2.2 Transition metal dichalcogenides

Apart from graphene, 2D TMDs also exhibit extraordinary electronic, optical and mechanical properties that have been extensively studied in recent years.[52, 53, 101-104] They are typically with the formula MX_2 , where M stands for transition metal (elements from group IV, V

and VI, such as Mo, W, and Re), X stands for dichalcogenides, such as Se, S or Te. TMDs can be seen as a layered structure of covalent bonded X-M-X layer, with the X atoms in two hexagonal planes separated by a plane of M atoms, as shown in Figure 2.5.[105] Adjacent layers are held together by the vdW force to form the bulk crystals. Thus, same as graphene, monolayer TMDs can be exfoliated from their bulk crystals.

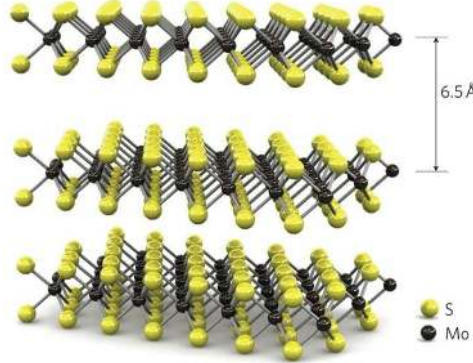


Figure 2.5. MoS₂ crystal structure.[105]

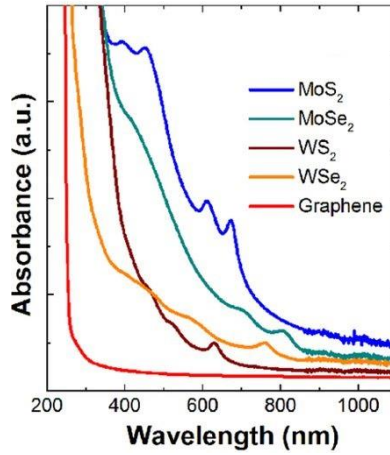


Figure 2.6. Absorption spectra of four different TMDs monolayers and graphene.[106]

Despite the thickness of the TMDs monolayers is less than 1 nm, their absorbance is several times larger than graphene in the visible wavelengths. Figure 2.6 shows the absorption comparison of monolayer MoSe₂, MoS₂, WS₂, WSe₂, and graphene.[106] The absorbance (A) of TMD monolayers can be expressed by the equation :

$$A = 1 - e^{-\alpha L}$$

where α is the absorption coefficient, and L is the thickness of the TMDs.[14] Thus, for example, the calculated absorption of monolayer MoS₂ ($\alpha = 1 \sim 1.5 \times 10^6 \text{ cm}^{-1}$) is 5~10% despite the thickness of 0.65 nm. This high absorption in TMDs makes them an ideal candidate to act as thinnest photo-active materials.

Owing to their versatile crystal structures, TMDs can render as insulators, semiconductors, and superconductors. In general, bulk TMDs exhibit indirect bandgap nature, whereas, the band structures transit to direct bandgap when they are thinned from bulk to monolayer.[107] Figure 2.7 shows an example of this band structure transition for multilayer and monolayer MoS₂. [108] This transition from indirect to direct bandgap leads to the enhancement of the PL in monolayer. As shown in Figure 2.8, the PL intensity is strong for monolayer, and the intensity of the peak weakens as the number of layers increases.[109] This characteristic offers the unique advantage of TMDs for layer-dependent optical bandgap.

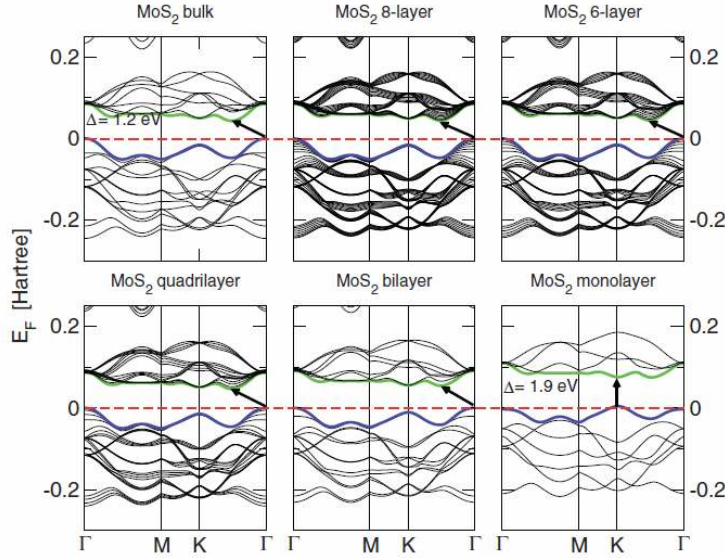


Figure 2.7. Calculated band structures of MoS₂ with different layers, indicating a transition from an indirect to a direct band gap.[108]

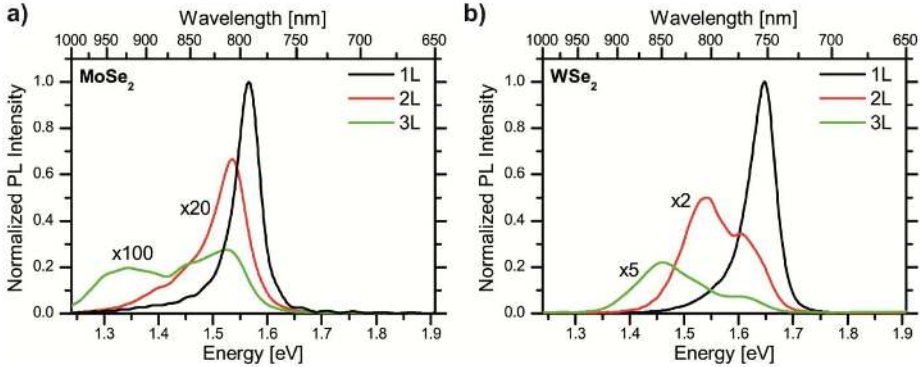


Figure 2.8. Photoluminescence of monolayer and few-layer MoSe₂ (a) and WSe₂ (b).[109]

The ability to control the electrical properties of TMDs, such as carrier density, is crucial in modern electronics. For example, MoS₂ has been realized as a stable p-type semiconductor by substitution Nb doping with a hole density of $3 \times 10^{19} \text{ cm}^{-3}$. [110] Moreover, the atomic thickness nature of the TMDs allows efficient electrostatic doping by the gate voltage which will possibly lead to (1) the improvement of the mobility, (2) the reduced contact resistance and (3) the enhancement of the photoresponsivity.[87, 111, 112]

Different metal contacts to TMDs will lead to the differences in the device performance. For example, Au contact to monolayer MoS_2 , a tunnel barrier will form, which suppresses the electron injection into the MoS_2 , resulting in the low electron mobility of MoS_2 based FETs.[113, 114] Besides, the low work function metal Ti will introduce an ohmic contact to WSe_2 whereas the high work function metal Pd will result in a Schottky contact.[115, 116] Thus, finding an appropriate metal as the contact to TMDs is an active area of research for high-performance electronic devices, which will be discussed in Chapter 4. In conclusion, the unique and tunable physical properties make TMDs as an ideal candidate to solve not only the scientific but also technological challenges, especially in the area of photonics.

2.3 Heterojunctions

As we have mentioned, TMDs are one of the promising candidates for the next generation of optoelectronic devices, especially in the field of photodetection. However, the operational bandwidths of the TMDs based photodetectors are usually limited by the bandgap of the composed materials. For example, the bandgap of monolayer MoS_2 is around 1.8 eV and 1.2 eV for the bulk counterpart.[107] This indicates that the MoS_2 based photodetector can only be used for detection of the photons with the energy larger than 1.2 eV, impeding the application in the infrared (IR) wavelengths. vdW heterojunctions based on TMDs by stacking different individual TMDs offer a way to overcome this drawback. Comparing with the traditional materials based heterojunctions which require not only complex and expensive fabrication processes but also similar lattice structures of each material, the TMDs based heterojunctions can be easily realized by stacked laterally or vertically due to the weak interlayer interaction.[80, 83, 84, 117]

Moreover, due to various work-functions and bandgaps of TMDs, the band alignment of the heterojunction can be artificially determined. As shown in Figure 2.9, the heterojunction can be classified into three categories, type I, type II and type III. [83] The type-I band alignment is usually used in laser and light emitting diodes (LEDs) due to the ability of confinement of the electrons and holes so that the efficient recombination could occur.[118] The type-II band alignment is most extensively studied in the field of optoelectronics due to their excellent electron-hole pair separation efficiency.[78, 81, 119] Type-III band alignment is usually used in tunneling field effect transistors (TFET) due to its enhancement of tunneling current density.[120-123]

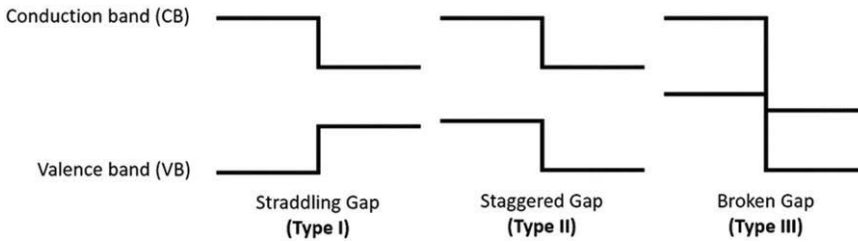


Figure 2.9. Illustration of type I, type II and type III heterojunctions.[124]

Further, thanks to the atomic thickness nature of the composed TMDs, the external electrostatic gating could efficiently tune the carrier density as well as the energy band alignment of the heterojunction. This is quite important in optoelectronics since the band alignment transi-

tion provides the platform of realizing multifunctional devices via electrostatic doping. In addition, various mixed-dimensional heterostructures also offer superior performances, when combining with different low-dimensional nanomaterials.[125-146] In Chapter 5, we discuss the transition of the band alignment from type-II to type-III by properly gating and biasing, providing not only broader photodetection wavelengths but also the enhanced photoresponsivity.

3. Fabrication of two-dimensional layered materials-based devices

The performance of the 2D layered materials-based photonics devices is highly dependent on the preparation and process methods. In this chapter, several synthesis methods and transfer methods for 2D layered materials are presented and compared. Moreover, the microfabrication methods, such as Electron beam lithography (EBL), atomic layer deposition (ALD) and plasma etching, are also reviewed.

3.1 Two-dimensional material synthesis methods

3.1.1 Mechanical exfoliation

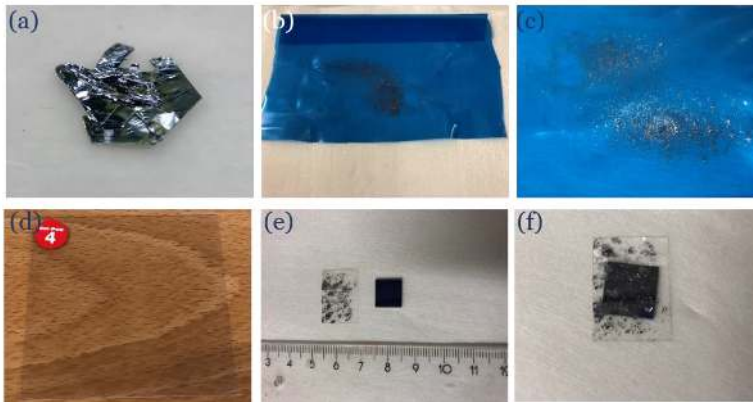


Figure 3.1. (a) MoSe₂ bulk sample. (b-c) Exfoliation of MoSe₂ flakes from MoSe₂ crystal. (d) Image of the polydimethylsiloxane. (e) Transfer exfoliated flakes from a tape to the polydimethylsiloxane film. (f) SiO₂/Si substrate placed against the polydimethylsiloxane to transfer the exfoliated flakes.

The mechanical exfoliation method was developed to obtain monolayer graphene from highly oriented pyrolytic graphite.[1] This method has been demonstrated as an ideal approach to yield high-quality thin layers for fundamental studies of exploring new physics. The number of layers can be identified by optical microscopy, Raman/PL spectroscopy or atomic force microscopy (AFM). The obtained flakes of 2D layered materials remain stable in ambient conditions for a few months. However, the size, uniformity and the thickness of the flakes obtained by this method are uncontrollable as well as the low throughput, suggesting the impractical large-scale applications.[147]

The procedures of the mechanical exfoliation are shown in Figure 3.1. In this section, we use MoSe₂ as an example (Figure 3.1(a)) to present the process of mechanical exfoliation. Scotch

tape is used to repeatedly stick and peel off the bulk into thinner layers until the tape is fully occupied with exfoliated flakes (see Figure 3.1(b)-(c)). Polydimethylsiloxane (PDMS) is used before transfer the exfoliated flakes on the substrate to avoid the contamination from the scotch tape (Figure 3.1(d)). Then, we press the PDMS sheet on the tape to make the exfoliated flakes adhere on the PDMS. (see Figure 3.1(e)). Finally, a pre-cleaned SiO_2/Si wafer is placed against the PDMS and pressed it lightly (Figure 3.1(f)). There will be the lateral movement of the PDMS when too much force is used, which would lead to the broken of the exfoliated flakes. If the thickness of the SiO_2 layer is around 300 nm, it is easy to distinguish single layer of 2D layered materials through the optical microscopy.[1] After the exfoliation, the thickness of the flakes can be checked by AFM.

3.1.2 Chemical vapor deposition

The CVD method is a deposition method which has been used to obtain high quality, wafer-scale and thickness controllable TMDs.[148-151] It possesses many essential benefits compared with the exfoliation method, and is compatible with current semiconductor technologies. Briefly, the CVD process deposits materials onto a heated substrate through chemical reactions of the compounds contained in the gas passing over the substrate. Here we give an example of the growth of the CVD graphene on copper foil.

The schematic of the CVD process for graphene on Cu foil is depicted in Figure 3.2.[152] Due to the low solubility of carbon atoms into the Cu, the growth process is performed through the surface reaction. In this term, the graphene film will be formed along the Cu surface, and graphene can be formed at the grain boundary of Cu. Moreover, the process will be self-terminated once the Cu surface is fully covered by monolayer graphene.

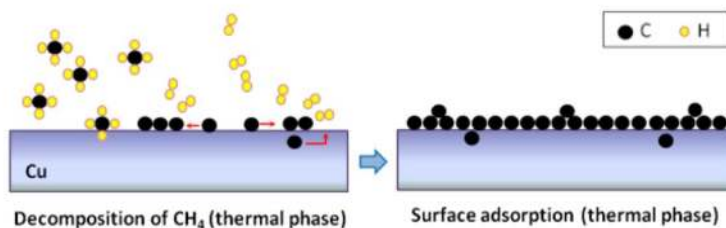


Figure 3.2. Schematic of the CVD process for graphene growth on copper.[152]

3.1.3 Other synthesis methods

There are a few other methods for TMDs synthesis, such as molecular beam epitaxy (MBE), liquid-phase exfoliation, physical vapor deposition (PVD) and ALD, as shown in Figure 3.3.[153-156]

MBE is one of the first scalable methods which was developed for the growth of 2D layered materials. The principle of the operation is shown in Figure 3.3(a). An ultrahigh vacuum chamber contains Mo and Se (in this case) to form molecular beams and the deposition is performed on a GaAs substrate. The thickness and the crystallinity are monitored by reflection high-energy electron diffraction and low-energy electron diffraction.[157] In order to obtain high-quality films, the substrate and the overlayer should be ensured lattice-matched, such as growing MoSe_2 on GaAs and MoS_2 on sapphire.[147, 158] If the condition does not meet, such as grow-

ing MoS₂ on SiO₂, the resulting samples will be polycrystalline and contain many dislocations.[159] Interestingly, the MBE method can be used to grow heterojunctions of 2D materials directly without worrying about the lattice mismatch. Thus, MBE is a powerful tool for scientific research of 2D materials and their heterostructures, although the electrical properties of as-grown films require further improvement and the growth rate is quite smaller than that of CVD (~ 0.1 - 0.3 monolayer/min). [121, 160]

The liquid-phase exfoliation can be divided into two categories: solvent exfoliation and chemical exfoliation. Solvent exfoliation involves the process of powders which are dispersed in an organic solvent together with sonication which is used as the external energy for cleavage. Varieties of 2D layered TMDs have been successfully obtained by this method, such as MoS₂, WS₂, MoSe₂, MoTe₂, and h-BN.[118] The drawbacks of this method are obvious, for example, the poor uniformity and low yields of large flakes. The chemical exfoliation can overcome these drawbacks through the interaction between the materials and the small ions (e.g., lithium ions). In this method, a single layer of the materials can be readily obtained. However, a washing step is needed to remove the lithium ions. The drawbacks of the chemical method are the nonuniformity of the monolayer flakes and the uncontrollable size of the flakes.[161]

PVD describes a method during which the material goes from a condensed phase to a vapor phase and finally changes to a thin film with a condensed phase. Figure 3.3(c) depicts illustrates a PVD setup for the growth of MoS₂. Compared with CVD method, which requires two differences sources for X and M for the growth of MX₂, the PVD method can directly use MX₂ powders as source materials. As heating, MX₂ will be evaporated and transported to the high-temperature zone, followed by depositing onto the insulating substrate.[162] In this method, the major parameters that can be changed are the temperature of the source and the substrate as well as the distance between them. The limitation of this method is the uncontrollable and nonuniform thickness.[160]

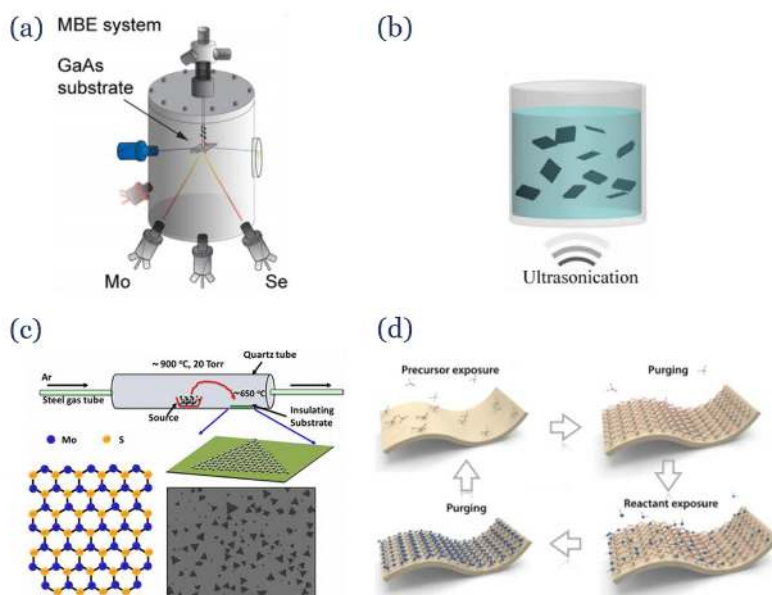


Figure 3.3. Schematic drawings of (a) MBE, (b) liquid-phase exfoliation, (c) PVD and (d) ALD.[147, 163, 164]

ALD is a gas phase chemical process to deposit atomically thin films of various materials layer by layer by using precursors to react with substrate.[165] Since the ALD method has inherently excellent thickness control ability in nanometer scale, it is considered to be a promising candidate to synthesize 2D layered materials. However, the reported ALD grown TMDs flakes show poor physical properties, limiting their electrical and optical applications.[154]

In conclusion, each synthesis method has its own merits. In this manner, one should select the proper synthesis method according to the utilizing purpose. Comparing with MBE, PVD and ALD methods, CVD method owns the ability of producing high quality, uniform, large area and excellent physical property 2D layered materials. In this manner, CVD graphene is chosen in this thesis to make the graphene-based modulators.

3.2 Device fabrication

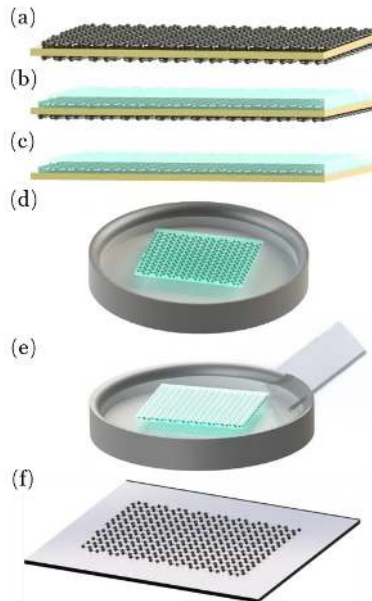


Figure 3.4. Graphene transfer process. (a) CVD graphene on copper. (b) Spin coating PMMA on top of the graphene. (c) The bottom layer of graphene on copper was etched by RIE. (d) The graphene/copper foil was floated on APS to etch the copper. (e) After transferring the graphene/PMMA in the DI water, it then transferred to the pre-cleaned quartz substrate by the fishing method. (f) The transfer graphene device.

Significant attempts have been made in transferring 2D layered materials. In this section, the transfer process of CVD growth graphene and the exfoliated TMDs will be introduced. The schematic of the transfer process is shown in Figure 3.4. Before starting the transfer, the substrate (e.g., quartz) is first cleaned with ultrasound in acetone and isopropanol (IPA) for 5 minutes to remove contamination particles. Since graphene is grown on a copper foil by the CVD method, both sides of the copper foil will be covered by graphene (Figure 3.4(a)). Thus, the graphene layer on the top side of the copper is spin-coated with PMMA (the blue layer in Figure 3.4(b)) to avoid damages from the transfer process. After baking for 1 minute at 90 °C on a hotplate, graphene on the bottom side of the copper foil was etched away in the reactive ion etching (RIE) system with the oxygen gas (gas flow 10 sccm, the pressure of 50 Pa and power of 30 W) as shown in Figure 3.4(c). Then, the graphene/copper foil is floated on the ammonium persulfate (APS) for 8 hours to etch away the copper foil (Figure 3.4(d)). After the

etching process, the CVD grown graphene is then transferred into the deionized (DI) water to remove the APS solvent residue by utilizing the fishing method. Then, the graphene is scooped from below in the DI water container with the substrate (Figure 3.4(e)). The sample is left to dry at ambient condition for 2 hours and bake at 180°C for 10 minutes on the hotplate to remove the trapped DI water. Once the sample is dried, it is immersed in acetone and IPA to remove the PMMA protection layer. After the transfer process is finished, and the CVD graphene flake is left on the quartz substrate.

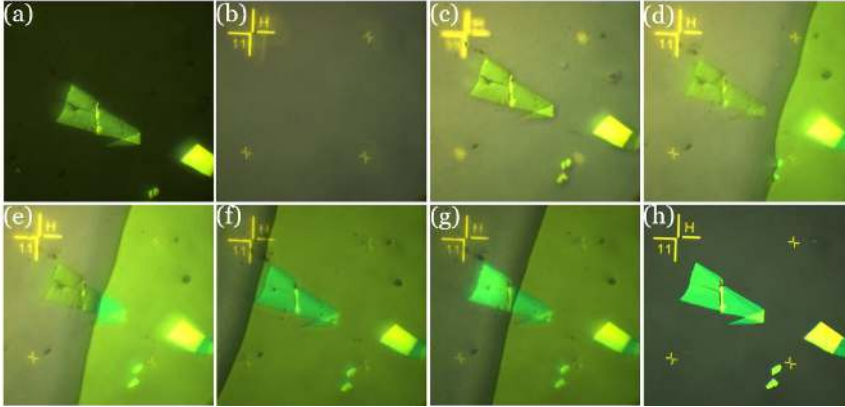


Figure 3.5. The transfer process of a WSe_2 flake to the target position on a SiO_2/Si substrate. (a) The desired flake was selected. (b) Find the desired transfer position on substrate. (c) The flake and the position on the substrate were aligned. (d-f) The flake was brought into contact with the substrate. (g) The PDMS was slowly peeled off from the substrate. (h) The optical image of the transferred flake.

The exfoliated TMDs which are used in this thesis are WSe_2 , MoSe_2 , and SnSe_2 . Here, we use WSe_2 as an example to illustrate the transfer process of these materials. Moreover, this method is also used to make the vdW heterojunctions which will be discussed in Chapter 5. The experimental setup which is used for the transfer is shown in Figure 3.6, which consists of a microscope and a 3D transfer stage.

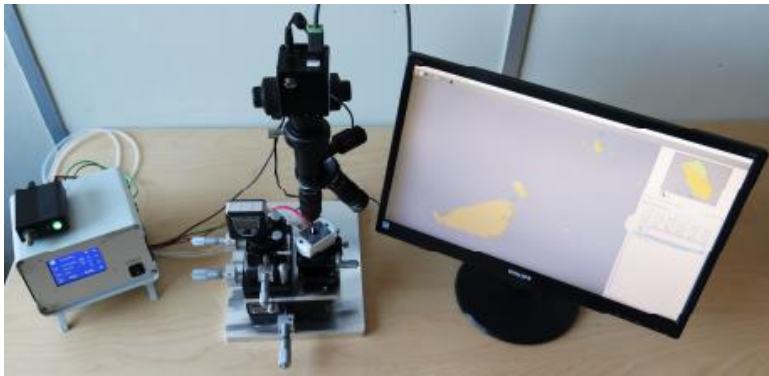


Figure 3.6 Experimental setup employed for the transfer process.

Before transfer, scotch tape is used to obtain few-layer WSe_2 flakes. A Si/SiO_2 substrate is first cleaned in Acetone/IPA for 5 minutes to remove the contamination. Then, a microscope is used to select the desired WSe_2 flake for transferring. After selecting the desired one (usually $20 \times 20 \mu\text{m}^2$), the PDMS film which near the flake is cut by a knife ($1 \times 1 \text{ mm}^2$) and then placed on a glass holder. Another microscope is used to monitor the transfer stage. After moving the

target substrate beneath the transferring stage and selecting the desired position for transfer, the glass holder is then slowly lowering down until it touches the substrate. Then the flake is transferred to the substrate successfully. The corresponding process is shown in Figure 3.5.

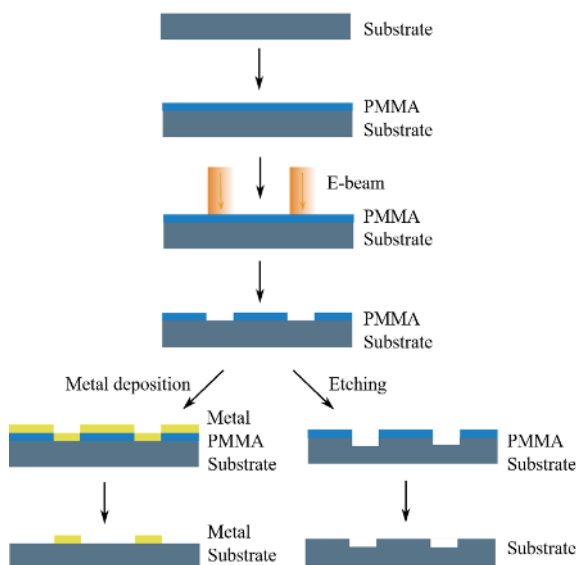


Figure 3.7 Electron beam lithography, metal deposition and etching processes.

In this work, pattern generation is performed by using the standard EBL process in the clean-room. Figure 3.7 shows an example of the standard EBL, metal deposition and etching procedures. The substrate (quartz or SiO_2/Si) is first spin-coated with the photoresist (PMMA) at the speed of 4000 rpm/sec. Then, the substrate is baked on a hot plate at 180 °C for one and a half minutes to evaporate the solvent and adhere the photoresist to the substrate. Next, the substrate is placed on the sample aligner to make sure the wafer is aligned. The pattern is pre-drawn by the CleWin software. The EBL tool (Vistec EPBG5000pES) is carried on to expose the pattern on the sample. After the exposing, the photoresist is then developed by the MIBK/IPA solvent for a few seconds. Then, the developed photoresist is used as a mask either for the etching or for metal deposition. Finally, the sample is immersed in acetone to remove the PMMA mask or do the lift-off process.

ALD is used in this work for fabricating the insulating layers. Due to the large bandgap, high thermal stability and high dielectric constant, HfO_2 is an ideal choice for the insulating layer in graphene-based modulators. The HfO_2 is deposited by pulsing Tetrakis (dimethylamino) hafnium ($\text{TDMAH} \equiv \text{HfN}_4\text{C}_8\text{H}_{24}$) and water in an alternating fashion with ALD. Before the pulsing, the solid TDMAH-precursor is sublimated by heating it at 50 °C. The ALD process is carried out at 170 °C to ensure the high quality of the HfO_2 film. After the deposition, the growth rate ($\sim 0.991 \text{ \AA/cycle}$) and the thickness of the HfO_2 film are measured from a reference silicon substrate by using a commercial ellipsometer.

The plasma is a common tool used during the nanostructure fabrication process of 2D layered materials. The O_2 plasma etcher is used in this work to define the desired area of the graphene modulator and remove the undesired part of the TMDs. The etching process is performed (Plasmlab 80Plus Oxford Instruments) using a low-pressure plasma system. O_2 , the precursor gas, is channeled into the chamber. Then, the high-power radio waves are applied in the

chamber to ionize the O_2 molecules to form the plasma. The O_2 plasma would have physical collisions and chemical reactions with materials realizing the etching process.

4. Characterization of two-dimensional layered materials-based devices

During the fabrication processes of the devices, the 2D layered materials need to be fully characterized. In general, the steps for device characterization are usually performed as follows:

- (1). The thickness of the obtained flake is first measured by AFM.
- (2). Raman and PL spectroscopy are then used to confirm the optical properties of the samples.
- (3). After finishing the fabrication of the devices, the electrical properties (e.g., contact resistance) of the flakes are then characterized.
- (4). The optical properties of the devices, such as photocurrent, are finally being examined.

In this chapter, the tools and methods to characterize the prepared flakes and the methods for electrical and optical characterizations which have been described above are presented.

4.1 Atomic force microscope

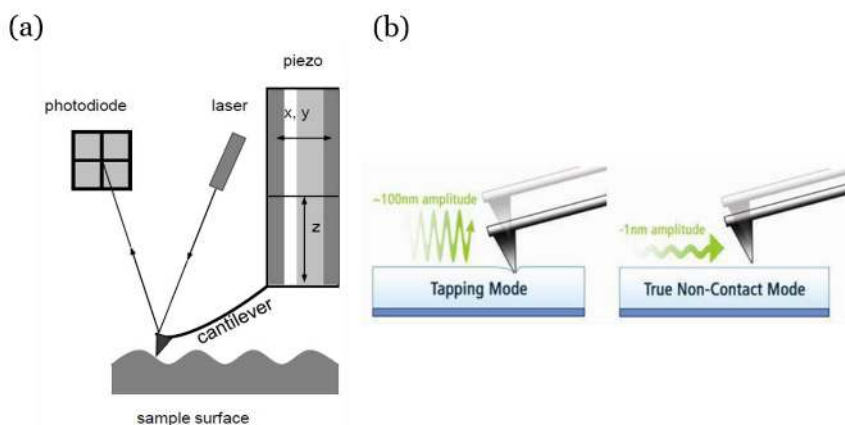


Figure 4.1. (a) Schematic of an AFM tool. (b) Schematic of AFM image modes.

The AFM has been demonstrated as a useful tool for direct measurements of micro structure parameters, especially for 2D materials, at the nanoscale level. The schematic of an AFM device is shown in Figure 4.1(a). In this work, AFM is operated in two modes: tapping mode and non-contact mode (Figure 4.1(b)). The non-contacting mode is usually utilized for testing soft or fluid samples, by putting the probe close to the surface of the sample (1-10 nm) to detect the attractive vdW forces acting between the probe and the sample. In this mode, a small oscillation is given to the probe, and by monitoring the change of amplitude, phase, and frequency of the oscillating cantilever, the weak vdW forces can be detected. The tapping mode usually

yields high-resolution imaging of samples. In this mode, the cantilever oscillates near its resonance frequency. When the probe is not in contact with the surface, the tip is vibrated at a constant amplitude; however, when it contacts with the sample, the vibration amplitude will be decreased due to the less availability vibrating space. By recording the difference in amplitude, a tapping AFM image is produced. In this thesis, NT-MDT Ntegra AFM is used to measure the thickness of the exfoliated flakes with the scanning area of $100 \times 100 \mu\text{m}$. Thus, it is possible to get the thickness of the TMDs accurately using the AFM system. Figure 4.2 shows an AFM image acquired from a $\text{MoSe}_2/\text{WSe}_2$ heterostructure. The thicknesses of the MoSe_2 and WSe_2 can be seen clearly, which are 4 nm and 7 nm respectively.

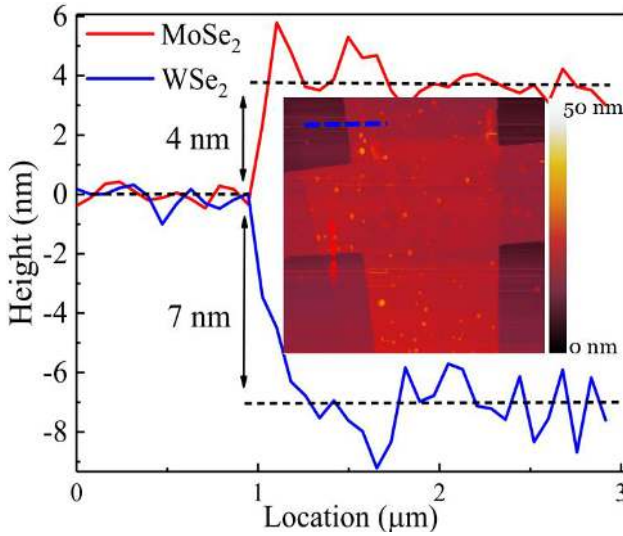


Figure 4.2. The dashed red/ blue lines show line scans of the heterostructure. Inset: AFM image of the $\text{MoSe}_2/\text{WSe}_2$ heterostructure.

4.2 Raman spectroscopy

Raman spectroscopy has been demonstrated as an important tool for 2D layered TMDs characterization owing to its non-disruptive, fast and accurate process. The exact number of layers of exfoliated TMDs flakes can be determined by monitoring the energy, width, and amplitude of the vibrational modes.[166, 167] It uses a laser as the irradiation source which will generate a small amount of scattered light from the sample. By detecting this scattered light (approximately one photon out of a million), the Raman spectrum will be obtained.

The Raman scattering was first experimentally discovered in 1928 by C. V. Raman and K. S. Krishnan in liquid.[168] When light is scattered by matter, most of the scattering is an elastic process (Rayleigh scattering), which means the scattered photons process the same energy as the irradiation photons. However, there still exist a small number of photons scattered inelastic (Raman scattering), meaning the scattered photons have the energy different from the incident light. These two scattering processes are shown in Figure 4.3.[168] The incident light interacts with the molecules and distorts the cloud of electrons to form a virtual state. Since this virtual state is not stable, the excited photons will fall to the ground level quickly. The Rayleigh scattering presents that an electron is excited from ground level and then falls to the same level

(Figure 4.3(a)). The Raman scattering can be classified into two types: Stokes Raman scattering (Figure 4.3(b)) and Anti-Stokes Raman scattering (Figure 4.3(c)).[168] The Stokes Raman scattering represents the process when the electron is excited from the ground level and falls to the vibrational level (with longer wavelength than the incident light), and the Anti-Stokes Raman scattering shows a process when the electron is excited from vibrational level and falls to the ground level (with shorter wavelength than the incident light).

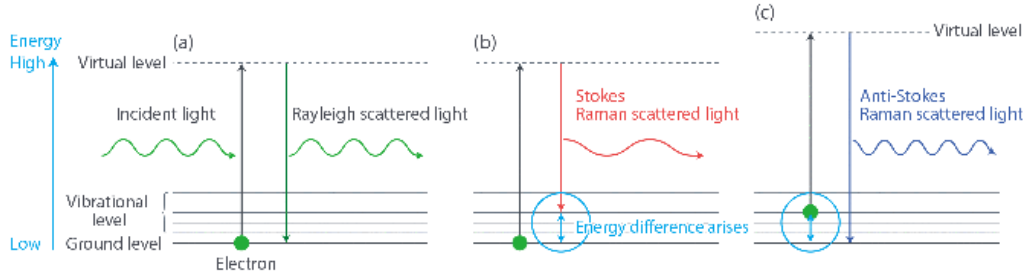


Figure 4.3. Diagram of the (a) Rayleigh and (b-c) Raman Scattering Processes.[168]

In practical Raman measurement, the Rayleigh scattering is usually blocked by a filter, and only Raman scattering will be recorded. Moreover, Raman spectrum is independent of the excitation wavelength, where Raman shift is typically in wavenumber instead of the wavelength. The Raman shift is calculated as $(1/\text{excitation wavelength}) - (1/\text{wavelength of Raman scattered light})$. [168] For example, a graphene Raman peak at 621.23 nm obtained by a 532 nm green laser can be converted into a wavenumber as Raman shift = $1/532 \text{ nm} - 1/621.23 \text{ nm} = 2700 \text{ cm}^{-1}$. Generally speaking, the Raman peak position and the shape are both important because they are derived from a specific molecular vibration or lattice vibration. In this work, the Raman spectroscopy (with a 532 nm excitation laser) is used to identify the thickness and measure the quality of CVD graphene as well as exfoliated MoSe_2 , WSe_2 , and SnSe_2 flakes.

The Raman spectrum of graphene is shown in Figure 4.4. G peak result (1580 cm^{-1}) from the primary in-plane vibrational mode and 2D peak (2690 cm^{-1}) come from second-order overtone of a different in-plane vibration. The number of layers can be derived from the intensity ratio (I_{2D}/I_G) and the positions of these peaks. The D peak is not visible in Figure 4.4 due to the absence of the defects.[167]

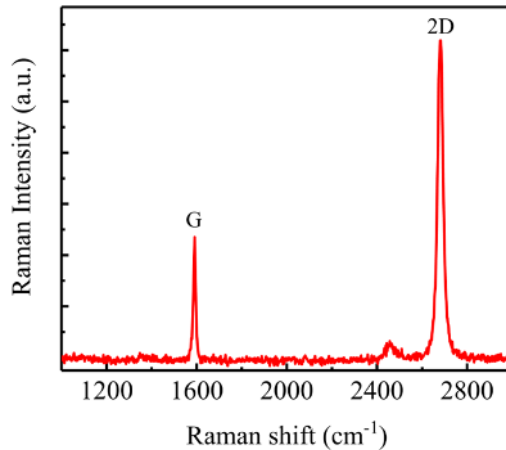


Figure 4.4. Raman spectrum of graphene. Publication VI.

The Raman spectrum of TMDs is shown in Figure 4.5. Here we use a WSe₂/MoSe₂ heterojunction as an example. Figure 4.5(a) shows the optical image of the device where WSe₂ and MoSe₂ are marked in it. Figure 4.5(b) shows the corresponding Raman spectrum obtained from WSe₂, MoSe₂, and heterojunction respectively. Three Raman modes are observed in the Raman spectrum of MoSe₂ close to the wavenumbers of ~ 242 cm⁻¹, ~ 285 cm⁻¹ and ~ 360 cm⁻¹. These peaks originate from the out-of-plane A_{1g}, in-plane E_{2g}ⁱ and B_{2g}ⁱ vibration modes of MoSe₂, respectively.[61]

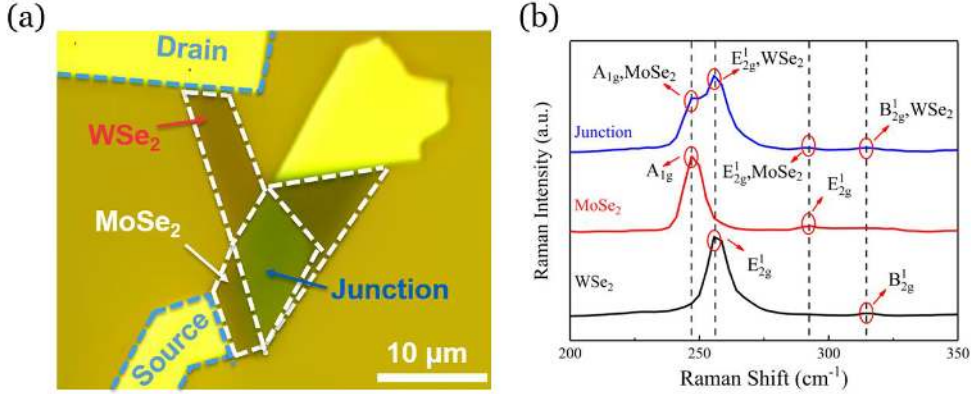


Figure 4.5. (a) The optical image and (b) Raman spectrum of a WSe₂/MoSe₂ heterojunction. Publication II.

On the other hand, two Raman peaks are observed in Raman spectrum of WSe₂ at the wavenumbers of ~ 260 cm⁻¹ and ~ 309 cm⁻¹ and attributed to in-plane E_{2g}ⁱ and B_{2g}ⁱ vibration modes of WSe₂. [61] The observed Raman modes of MoSe₂ and WSe₂ are consistent with previously reported data.[61] Moreover, the Raman peaks of the overlapped region do not change compared to the positions of phonon modes measured from the individual flakes, which indicates that the quality of the flakes after transfer and fabrication processes remains the same.

4.3 Photoluminescence spectroscopy

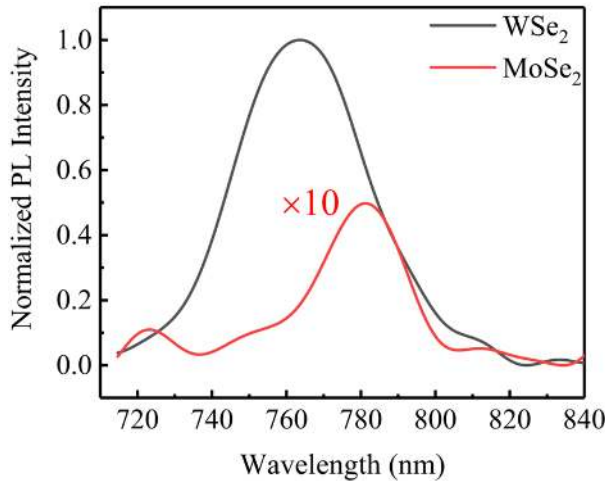


Figure 4.6. PL spectrum of WSe₂ and MoSe₂. Publication II.

PL offers an effective and easy approach to estimate the bandgap of materials. When an external excitation with photon energy larger than the bandgap of TMDs, the photons will be absorbed, and electrons in the valence band will be excited to its conduction band.[109, 169] When electron-hole pairs are relaxing to the band edges and then recombine to emit photons, the PL phenomenon will occur, the energy of which is equal to the optical bandgap. Due to the quantum confinement effect, the layer-dependent PL is prominent in the family of the TMDs. Thus, the PL can be used to estimate the layer number of the exfoliated flakes as well as their quality. Figure 4.6 shows a PL spectrum which was obtained from the device as shown in Figure 4.5(a). According to the PL results and equation $\lambda = hc/E$, where λ is the wavelength, h is the Planck's constant, c is the speed of light and E is the energy of photon, the strong PL peaks appear at 762 nm and 780 nm, corresponding to 1.62 eV and 1.58 eV as a reference for the band gap of multilayer WSe₂ and MoSe₂, respectively.

4.4 Electrical measurement

The performance of the optoelectronic devices is always highly related to their electrical contact properties. For example, contact resistance (CR) always limits the performance of the graphene-based modulators and TMDs based photodetectors. In this section, the contact resistance measurement and the other electrical characterizations of the TMDs based FETs will be introduced.

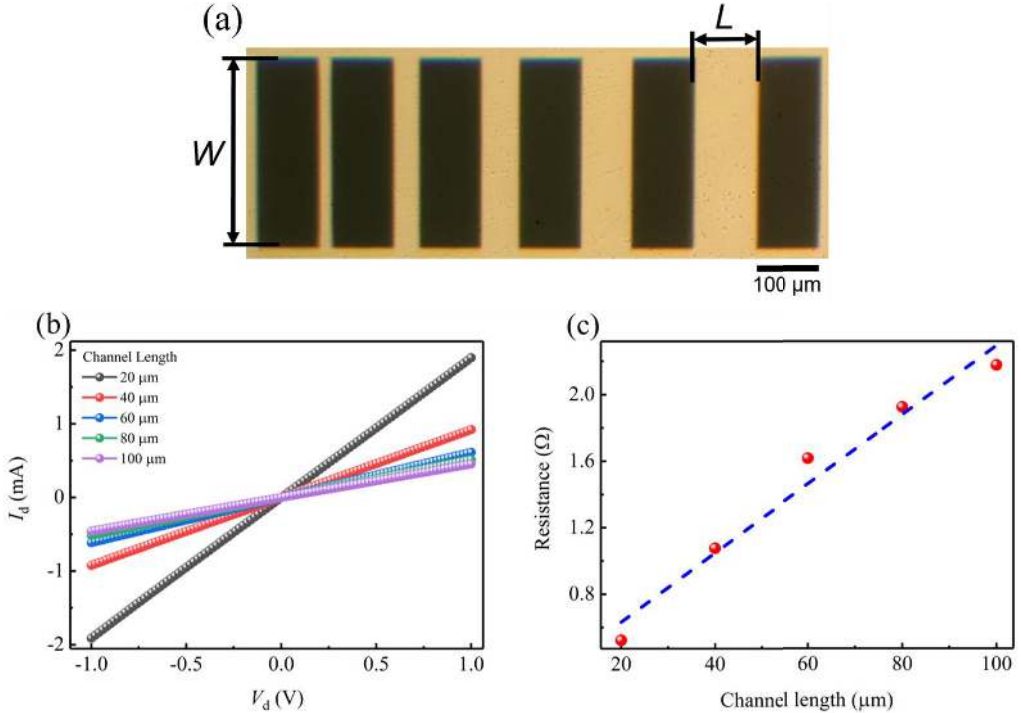


Figure 4.7. Graphene-metal contact resistance measurement. (a) Optical image of the device with yellow regions representing graphene and dark regions representing metal contacts. (b) I-V curves measured between pairs of electrodes at different lengths. (c) Extracted resistance plotted versus length between pairs of electrodes. The blue line is the linear fit of resistance versus L . Publication VI.

CR is a crucial limiting factor of the drain to source current (I_d) in graphene-based field-effect-transistors (FETs). CR is commonly measured through the transfer length method

(TLM).[170-172] Figure 4.7 depicts the corresponding TLM configuration and the optical image of the fabricated graphene-based FET.

The total contact resistance (R_{total}) can be calculated through the equation:

$$R_{\text{total}} = R_{\text{ch}}^s (L/W) + 2R_c$$

where R_{ch}^s is the sheet resistance of the graphene, L is the channel length, W is the channel width, and R_c is the contact resistance.[171] By varying the channel length, R_{total} with different lengths is marked in Figure 4.7 (b). The dashed blue line is the linear fit of R_{total} versus L . The R_{ch}^s can be obtained from the slope of the fitting curve, and R_c is the intercept of the fitting curve on the y-axis. The slope of the fitting curve is 21, namely $R_{\text{ch}}^s/W = 21 \Omega/\mu\text{m}$. Thus $R_{\text{ch}}^s = 6.3 \text{ k}\Omega\cdot\mu\text{m}$. Moreover, the intercept of the line is 217, giving the value of $R_c = 108.5 \Omega$.

The band bending theory was proposed to explain the rectifying effect of the metal-semiconductor junction. In this section, we are mainly focused on the characterization of Schottky contact (TMDs-metal interface) and the TMDs based FETs.

The TMDs-metal contact can be classified into two classes: Schottky contact and ohmic contact. Figure 4.8 gives an example of the band diagram when an n-type semiconductor contacts with different metals. The work function (ϕ_m) of the metal and the work function (ϕ_s) of the semiconductor are depicted in the upper panel of Figure 4.8(a-b).[173]

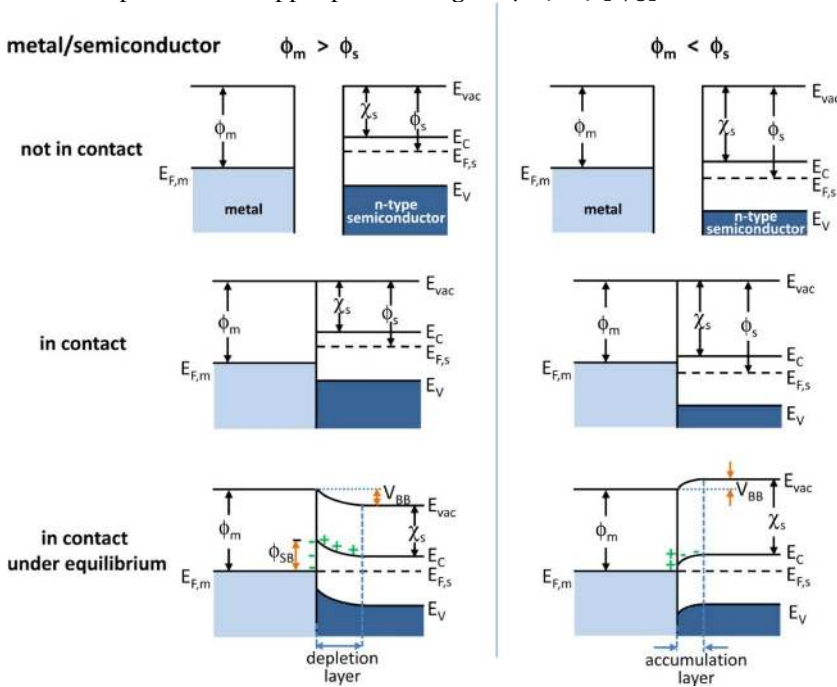


Figure 4.8. Energy band diagrams of metal and n-type semiconductor contacts. E_{vac} , vacuum energy; E_c , energy of conduction band minimum; E_v , energy of valence band maximum; ϕ_m , metal work function; ϕ_s , semiconductor work function; χ_s , the electron affinity of the semiconductor.[173]

Once the metal and semiconductor are in contact, the electrons and holes will transfer between the interface due to the differences in their work functions. If $\phi_m > \phi_s$, the electrons will move from the semiconductor to the metal, as shown in the middle panel of Figure 4.8(a). This transfer will be stopped once the Fermi level of metal (E_{fm}) and the Fermi level of the semiconductor (E_{fs}) are aligned. Due to the electrostatic induction, the metal will be negatively charged, and the semiconductor will be positively charged near their interface. Once the contact is

formed, due to the low carrier density on the semiconductor side (10^{17} cm^{-3}), the electrons are removed from the interface and a certain depth of the semiconductor. This leads to the formation of a depletion region, as shown in the bottom panel of Figure 4.8(a). The positive charge within the depletion region matches the negative charge that residues in metal. In this depletion region, the energy bands of the semiconductor will be bent upward. The degree of the band bending (V_{BB}) can be estimated according to the equation: $V_{BB} = |\phi_m - \phi_s|$. The Schottky barrier (ϕ_{SB}) is giving by the formula: $\phi_{SB} = \phi_m - \chi_s$, where χ_s is the electron affinity of the semiconductor. This barrier will prevent further electrons diffusion from semiconductor to the metal, and the Schottky contact is formed. On the other hand, when $\phi_m < \phi_s$, while the semiconductor and metal are in contact, the electrons will move from metal to the semiconductor and an accumulation region will be formed, as shown in Figure 4.8(b). In the accumulation region, the energy band bends downward toward the interface. Thus, an Ohmic contact is formed. In this matter, the barrier to electrons flow between metal and semiconductor is small and can be overcome by a small voltage.

The TMDs based FETs typically consist of three terminals which are the source, drain, and gate terminals. Drain and source terminals are used to bias the device for current, and the gate terminal is used to control the electrical property of the device. Figure 4.9(a) shows a schematic illustration of a WSe₂ based FET. The electrical properties can be analysed by applying constant drain to source voltage (V_d) and varying the V_g or applying constant V_g and varying the V_d as shown in Figure 4.9(b). When $V_g = 0 \text{ V}$, due to the high Schottky barrier at the WSe₂-metal interface, the drain to source current (I_d) is zero. However, when a $-70 \text{ V } V_g$ is applied, the I_d increases to $14 \mu\text{A}$ at $V_d = -2 \text{ V}$ owing to the electrostatic doping of the flake which decreases the barrier height at the WSe₂-metal interface. The mobility (μ) of the FETs can be obtained according to the equation: $\mu = [dI_d/dV_g] \times [L/(WC_iV_d)]$, where L is the channel length, W is the channel width, C_i is the capacitance between flakes and the gate per unit area.[105]

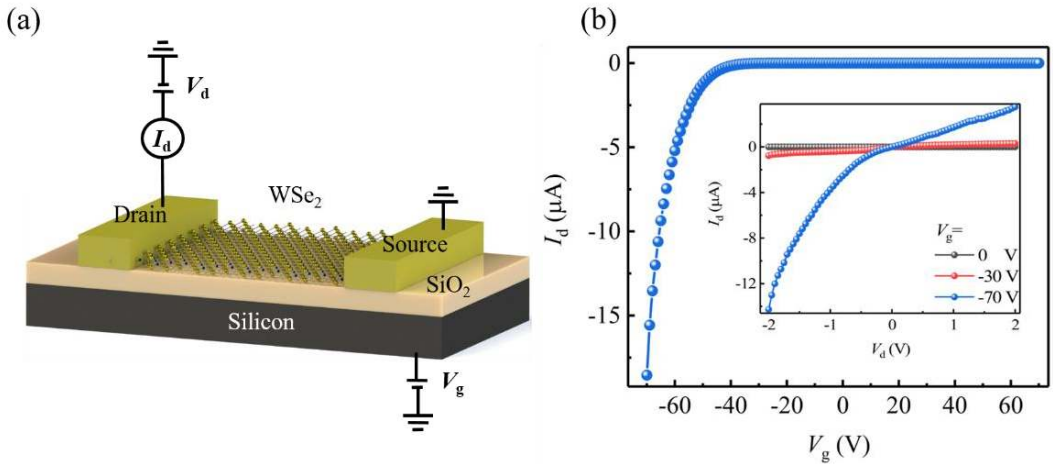


Figure 4.9. (a) Schematic illustration of the WSe₂ based FET. (b) Transfer curve of the WSe₂ based FET at $V_d = -1 \text{ V}$. Inset: I - V curve acquired for V_g values of 0, -30 and -70 V.

4.5 Photocurrent measurement

Photodetectors are devices which possess the ability to convert absorbed photons to the electric signals (i.e., photocurrent (I_{ph})).[174] Three physical processes are typically involved, which

are light harvest, photon-excited carrier separation, and separated carrier collection. [175] Several photodetection mechanisms with 2D materials have been reported, such as photoconductive effect and photovoltaic effect.[176-179]

The photoconductive effect involves a process of photons absorbed by a semiconductor and generating electron-hole pairs. It typically consists of a semiconductor as the channel and two ohmic contacts which serve as the drain and source electrodes.[104, 180] In the darkness, with a small drain to source voltage, a small dark current flows from the drain to the source electrode. Under light excitation (when photon's energy is larger than the intrinsic bandgap of the semiconductor), photon-excited electron-hole pairs will be generated and then separated by the drain to source voltage, resulting in the increasement of the drain to source current. In a photodetector, the transit time of electrons and holes is different due to their different mobilities. The transit time (τ_{transit}) can be expressed as

$$\tau_{\text{transit}} = L^2 / \mu V_d,$$

where L is the length of the channel.[181] If the mobility of the electrons is much larger than that of the holes, which means larger amount of the photon-excited electrons will flow in the channel, a photogain (G) phenomenon will appear (more electrons will be generated by one photon leading to the G larger than unity). The photogain can be referred to the ratio of the photon-excited carrier lifetime (τ_{carrier}) and the transit time (τ_{transit}), expressed as:

$$G = \tau_{\text{carrier}} / \tau_{\text{transit}} = \tau_{\text{carrier}} \mu V_d / L^2.$$

Photodetectors which perform in the photovoltaic effect are usually called photodiode.[179, 182] It relies on the built-in electric field to separate the photon-excited carrier. A photodiode is usually made of p-n diodes (consisting of two opposite doping type of semiconductors) or Schottky diodes (the metal-semiconductor interface).[87, 179] In the darkness, the I - V curves of the photodiodes usually exhibit rectifying characteristics, where I_d is exponential with the V_d under forward bias condition and is usually negligible under reverse bias condition. Under the external illumination and without external bias, the photodetectors work in the photovoltaic mode; the built-in electric field will efficiently separate the photon-excited electron-hole pairs and generate photocurrent (short circuit current, I_{sc}). While with illumination and a reversed bias voltage, the photodetectors work in photoconductive mode; the excited carrier will be swept to the electrodes by the bias voltage, leading to the generation of photo-voltage (open-circle voltage, V_{oc}).[179]

Moreover, under the reverse bias condition, the direction of built-in electric field and external bias is the same, the efficiency of the carrier separation and the speed of the response will be increased, due to the reduced carrier transit time and the capacitance of the junction. The G of the photodetector is usually less than unity when it works in photovoltaic mode and may exceed unity when works in photoconductive mode (with sufficient reversed bias voltage). In this matter, for the photodetector which works under the reversed bias condition, it can be used to detect extremely low power signal.

Figure 4.10 gives an example of photoresponse characterization of a graphene-GaSe heterojunction device. An optical image and a schematic of the device are shown in Figure 4.10(a). First, a white-light source was used to illuminate the device with a laser power (P_{laser}) of 0.16 mW (1.3 mW/cm²). The current measured under illumination ($I_{\text{illuminated}}$) was compared with the current in dark (I_{dark}) in transfer characteristics as shown in Figure 4.10(b). I_{ph} can be observed in the all gate bias regime, which was found varying from 20 nA to 0.4 nA in the top-gate voltage range of -20 V to 10 V at $V_d = -0.5$ V. Figure 4.10(c) shows the relationship of photosensitivity to the λ (i.e., 730 nm, 1330 nm and 1550 nm) of the device. Gate-dependent device

characteristics under the laser excitation with varying laser powers are also shown in Figure 4.10(c). An obvious increase in I_d with laser excitation was observed along the intensity of optical power (red curves for the 730 nm, blue curves for the 1330 nm, and pink curve for 1550 nm laser). When applying $V_d = -1$ V, maximum I_{ph} was 100 nA for the 730 nm laser (with $P_{laser} = 1$ mW), 8 nA for the 1330 nm laser (with $P_{laser} = 10$ mW), and 2 nA for the 1550 nm laser (with $P_{laser} = 5$ mW) at $V_g = -7$ V.

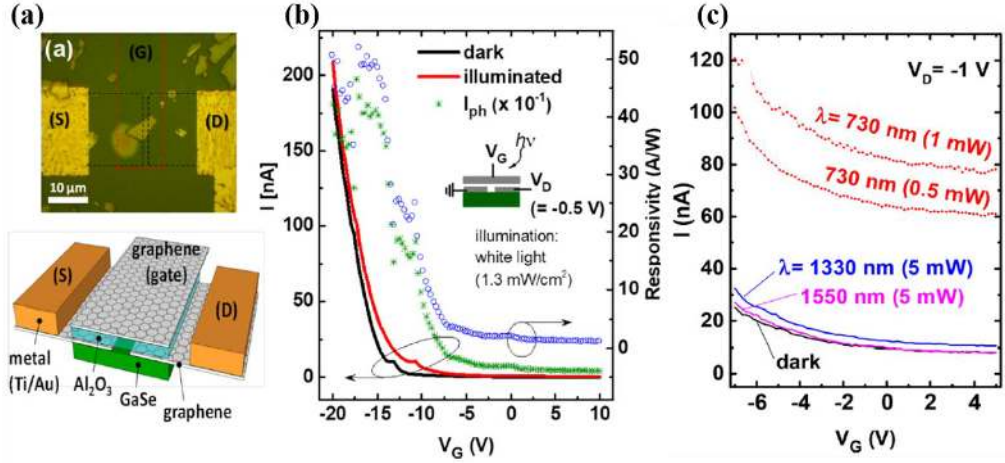


Figure 4.10. (a) Optical image and schematic of a graphene-gated GaSe FET with graphene contacts. Dashed lines in black and red denote a graphene contact and a top-gate, respectively. The GaSe channel size is $1 \mu\text{m} \times 4 \mu\text{m}$ (length \times width). (b) Transfer characteristics of the device measured in dark and under illumination (white light) at $V_d = -0.5$ V. Plots with symbols indicate I_{ph} (green stars) and corresponding responsivity (blue circles). The level of I_{ph} should be divided by 10 for a real value. (c) Transfer characteristics of the device under NIR illumination of 730 nm (red lines), 1330 nm (blue lines), and 1550 nm laser (pink line). (Publication IV)

5. Optoelectronic devices with two dimensional layered materials and their heterostructures

After discussing the synthesis, characterization and fabrication methods for 2D layered materials and their optoelectronics devices, in this chapter, we are going to present a few real examples of optoelectronic devices with 2D layered materials and their heterostructures. First two kinds of graphene based modulators are introduced. After, two broad-band photodetectors are then discussed in detail.

5.1 Graphene based modulators

Optical modulator is a critical component in the field of optoelectronic applications, such as bio-sensing, optical interconnect and security applications.[18, 125, 183] In recent years, lots of efforts have been made to obtain cost-effective, high speed and broadband optical modulators due to their intrinsic advantages compared with nowadays dominant interconnection approaches (i.e., copper cables). The modulators can be classified into several categories: all-optic, electro-optic, thermal-optic and so on.[125] Among them, the electro-optic method is mostly used in current applications. Several figures of merit are utilized to evaluate the performance of the modulators, such as modulation speed, modulation depth, operation wavelength range and insertion loss.[12]

Graphene and other layered 2D materials provide the extraordinary potential for various optoelectronic applications compared with those traditional bulk materials. For example, broadband operation bandwidth (from ultraviolet to microwave regions) has been demonstrated in graphene due to its linear electronic dispersion.[125] Moreover, by applying an external electric field, the Fermi level of graphene can be tuned, which allows adjusting the absorption of the graphene, making graphene an ideal candidate for optical modulators.

In this thesis, two types of graphene electro-optic modulators (GEOMs) with different substrates (i.e., quartz and gold mirror) have been made. The fabrication of the GEOM device with the quartz substrate starts with the transfer of the CVD graphene on a pre-cleaned quartz substrate using the transfer method which has been discussed in Chapter 3. After the transfer process, we spin-coat the device with a layer of PMMA (~400 nm) as the RIE etching mask. Standard EBL method is utilized to define the graphene channel ($500 \times 500 \mu\text{m}^2$). Later, the undesired part of graphene was etched away by the RIE. The bottom contact (Ti/Au) is then patterned on the bottom layer of graphene by an EBL process followed by a lift-off process. ALD process is used to directly deposit HfO_2 (30 nm), the material of high dielectric constant, as the insulator layer. The top layer graphene is then transferred on the HfO_2 layer and patterned by the same methods which have been mentioned before to fabricate the graphene channel and the metal contact. A cross-section schematic and an optical image of the device are shown in Figure 5.1(a) and (b).

The quality of the graphene before and after fabrication is monitored by Raman spectroscopy. After the device fabrication, three prominent peaks can be observed, which are D, G, and 2D peaks, as shown in Figure 5.1(c). The 2D peak is still a single sharp Lorentzian with a full width at half maximum (FWHM) $\sim 29 \text{ cm}^{-1}$, indicating that monolayer graphene was transferred. The ratio of D and G peaks ($I(D)/I(G)$) ≈ 0.06 , showing negligible defects in graphene.

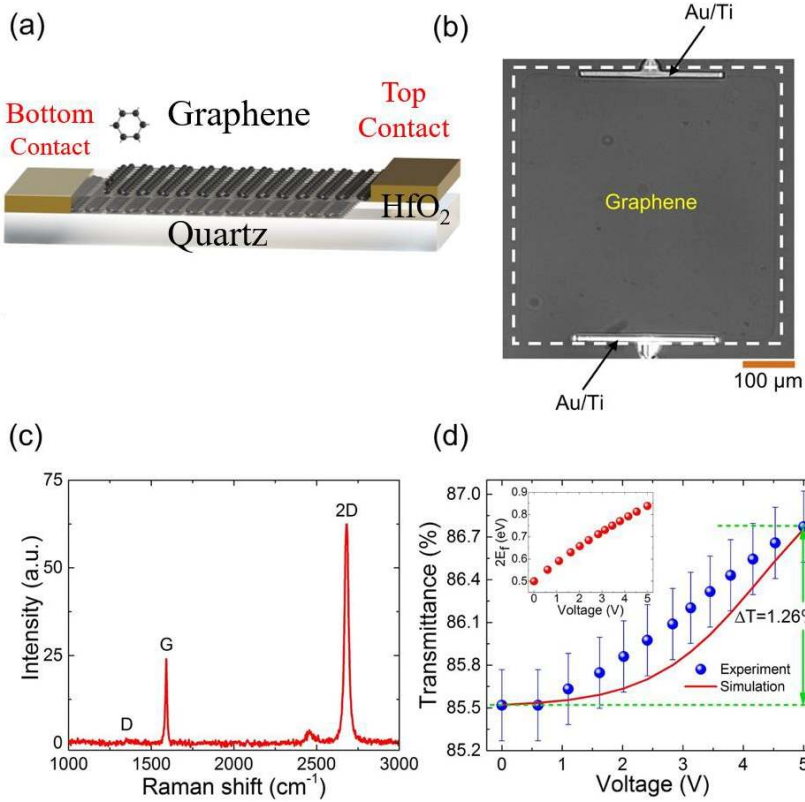


Figure 5.1. Schematic illustration and characterization of the GEOM device on the quartz substrate. (a) Three-dimensional sketch and (b) Optical microscopic image of our GEOM device. (c) Raman spectrum of graphene after device fabrication. (d) Optical transmittance as a function of the electrical voltage from experimental results (blue dots) and theoretical calculation (red curve). Inset: Calculated Fermi energy as a function of the electrical voltage. Publication VI.

The Fermi level of graphene can be tuned by applying the electric field, which will result in the changing of the absorption spectrum. We characterize the light modulation performance by measuring the transmittance spectrum as a function of applied voltages at the wavelength of 1550 nm, which is shown as the blue dots in Figure 5.1(d). The measured optical transmittance varies from 85.51% to 86.77 % as the applied voltage increases from 0 V to 5 V, presenting 1.26 % changing in the absorption. The transmittance loss at 5 V ($\sim 13.23 \%$) can be attributed to the optical loss of the quartz substrate ($\sim 8 \%$ Fresnel loss) and the insulator layer (2 % insert loss) as well as the absorption of the double layer graphene (3.3 % at 5 V). For theoretical calculation of the absorption as a function of the applied voltage, the Fresnel transfer matrix method is utilized, as shown in Figure 5.1(d). The calculated transmittance (red curve) is 85.52 % at 0 V and 86.77 % at 5 V, presenting 1.23 % changing in the absorption which is very close to the experimental results. A relatively low offset between the fitted curve and experimental results ($< 0.25\%$ difference in transmittance, figure 1(d)) is in a reasonable range

considering the inevitable deviation in the experiments. The inset of Figure 5.1(d) shows the Fermi level of the graphene layer varies as a function of the applied voltage. A 0.17 eV shift of the Fermi level can be observed, which can be further improved by optimization of the device fabrication methods, such as the quality of the HfO_2 layer and metal contacts.

The fabrication of the GEOM with a gold mirror starts with the substrate cleaning, where the Si/SiO₂ substrate is cleaned with ultrasonic in acetone and IPA for 5 minutes. The bottom metal reflection coating (Ti/Au, 5/130 nm) is first patterned by standard EBL process followed by metal deposition and a lift-off process. ALD method is then utilized to deposit a 187-nm thick HfO_2 film as the high dielectric constant insulating layer. Next, the CVD grown graphene is then transferred on the substrate using the same method as described in Chapter 3. The graphene disk (diameter of 80 μm) is then defined by EBL and ion etching processes. Finally, metal contact to the graphene sheet is fabricated by EBL and metal deposition processes.

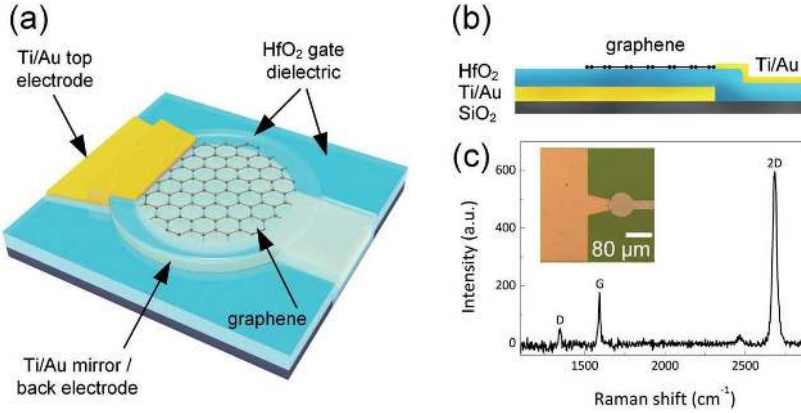


Figure 5.2. Schematic illustration and characterization of the GEOM device on the gold mirror. (a) 3D schematic illustration and (b) cross-section of the graphene modulator. (c) Raman spectrum of the graphene layer after device fabrication. Inset: microscope image of the fabricated graphene device. Publication III.

The schematic setup and the cross-section of the device are shown in Figure 5.2(a) and (b). The corresponding Raman spectrum and optical image are shown in Figure 5.2(c). The 2D peak is a single sharp Lorentzian with FWHM $\sim 29 \text{ cm}^{-1}$, confirming that monolayer graphene was transferred. The ratio of D and G peaks ($I(\text{D})/I(\text{G})$) ≈ 0.3 , showing defects might be induced during the device fabrication. The defect may come from the unintentional damage to graphene during the fabrication, such as when the graphene disks were defined by the EBL and RIE process and the tensile strain on the graphene/substrate interface during the transfer process. As for the reflective graphene-based modulator, the thickness of the insulating layer is a critical parameter, due to the standing wave at the surface by the incoming and reflected waves. The modulation depth can be modified by adjusting the position of the graphene layer along the standing wave. The linear absorption of the monolayer graphene can be varied from 0% (when placed in the node) to 9.2 % (when placed in the antinode, $\sim \lambda/4$) by adjusting the thickness of the HfO_2 film. The light field distribution can be calculated by the Fresnel transfer matrix method, as shown in Figure 5.3(a). The graphene layer is close to the antinode of the standing wave. The insertion loss of the fabricated device is 12.85% perfectly matching the calculated value (12.9%), as drawn in Figure 5.3(b).

Moreover, the reflectance as a function of the applied voltage is also shown in Figure 5.3(b), where a 1550-nm laser is utilized. The observed modulation depth is $\sim 1.94\%$ when the applied voltage varies from -5 to 5 V, which fits well with the theoretical calculations, confirming the

operation principle of our proposed device. The modulation bandwidth is investigated with the 1550 nm laser together with a lock-in amplifier connected with a 22 GHz photodetector. Our device shows a flat response with a 3 dB bandwidth of 13.2 MHz, as shown in Figure 5.3(c), which may be limited by the capacitance and resistance of the modulator, where $f_{3dB} = 1/(2\pi RC)$. The estimate capacitance of the device to be around 6 pF and the resistance is 2 k Ω . The R is affected by the contact resistance of the electrodes and the graphene sheet resistance, and C is affected by the geometry of the device. Further improvement of the quality of graphene and metal contact as well as the geometry of the modulator will increase the bandwidth.

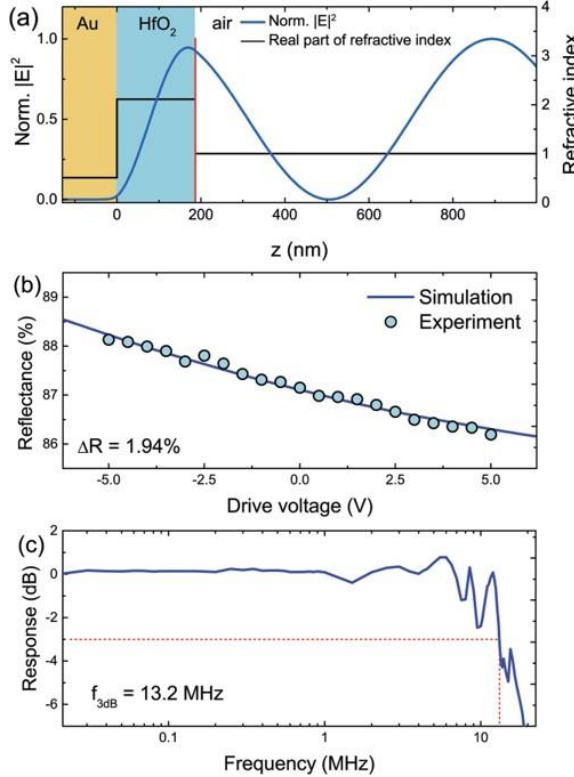


Figure 5.3. Characterization of the GEOM on the gold mirror. (a) Normalized electric field intensity calculation ($|E|^2$, blue line) and refractive index distribution (black lines) in the modulator. The wavelength is 1.55 μm . The red line indicates the position of the graphene layer. (b) The reflectance of the GEOM at different gate voltages. (c) Electrooptic frequency characteristic at 1.55 μm , indicating a flat response with a 3 dB bandwidth of 13.2 MHz. Publication III.

5.2 Transition metal dichalcogenide heterostructures based photodetectors

Photodetectors are the crucial device of the nowadays optoelectronic applications, such as remote control, imaging, monitoring, and telecommunications. a photodetector is a device which converts the absorbed photons into electrical signals. Traditional semiconductors, such as Si, InGaAs, and HgCdTe, are widely used in photodetector market due to their excellent performance and mature production and integration methods. However, the operational bandwidth of the photodetectors is usually limited by the bandgap of the composed materials, for example, Si, which shows negligible photoresponse in the infrared wavelength range, where the photon energy is lower than its bandgap. Most commercial IR photodetectors are based on Ge and

InGaAs, which possess obvious obstacles, such as low flexibility, miniaturization difficulty, and complex fabrication processes. Moreover, due to the lattice and thermal expansion coefficient mismatch, intergrating Ge or InGaAs with transitional Si technologies is a long-term challenge.[184, 185] The creation of vdW heterojunctions, formed by stacking different individual semiconducting TMDs, offers a new dimension in making various high-performance electronic and optoelectronic devices. [22, 58, 79, 119, 186-194] For instance, TMDs are covalently bonded in-plane and held together out-of-plane by van der Waals force, which are easily exfoliated and transferred to arbitrary substrates or stacked together to form heterojunctions in spite of lattice mismatch.[80] Among the various vdW heterostructures, type-II band alignment based heterostructures allow the efficient separation of the photon-excited electron-hole pairs, and thus improve the light to electrical signal conversion efficiency.[195] Recently it has been proved that this type heterostructure can facilitate the interlayer transition of sub-band gap photons for light detection at near-infrared (NIR) wavelengths.[196, 197] However, thus far, the demonstrated TMD heterostructures based photodetectors suffer from the relatively small photoresponsivity (e.g. 40 nA/W at $\lambda = 1550$ nm [198]) possibly because of the high Schottky barrier at the contact regions and insufficient band bending in the overlapping regions. In summary, TMD heterostructures based photodetectors need to be further explored, in particular for the sub-bandgap photodetection at telecommunication bands.

5.2.1 WSe₂/MoSe₂ heterojunction based photodetector

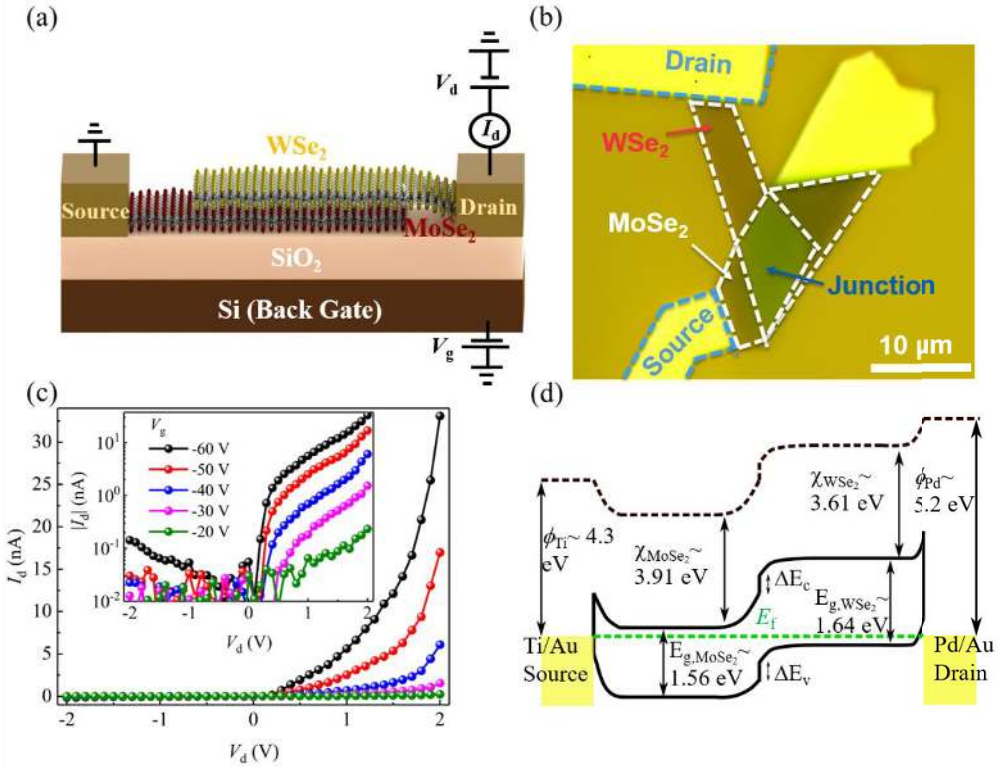


Figure 5.4. WSe₂/MoSe₂ heterojunction based photodetector. (a) Schematic illustration of the heterojunction device together with the electrical connections used to characterize the device. (b) Optical microscope image of the device. (c) I - V characteristics measured with variable back-gate voltages in dark. Inset: I - V characteristics on the logarithmic scale. (d) The schematic band diagrams of the device, where ϕ is the work function of metal; χ is the electron affinity of the flakes; E_f is the Fermi level and E_g is the band-gap. Publication II.

Figure 5.4(a) and (b) depict a schematic illustration and optical image of the proposed MoSe₂/WSe₂ heterostructure device. Few-layer MoSe₂ and WSe₂ flakes are mechanically exfoliated separately and then transferred onto a 280 nm Si/SiO₂ substrate. Using the transfer method which has been mentioned in Chapter 3, an overlapping region is formed by precisely controlling their locations. After, Pd/Au and Ti/Au electrodes are patterned and deposited on to WSe₂ and MoSe₂ flakes respectively. To facilitate the carrier transport, different metals are utilized here, where Pd can efficiently inject the holes to WSe₂ and Ti favor the injection of electrons to MoSe₂. The thickness of the transferred flakes is characterized by AFM spectroscopy, which gives the value of ~4 nm and ~7 nm. Raman and PL measurements are employed to ensure the quality of the flakes before and after fabrication. The device is biased in the configuration as shown in Figure 5.4(b), where drain to source voltage is applied on the WSe₂ side, and the back gate voltage is applied through the Si/SiO₂ substrate.

The I - V characteristics of the device are shown in Figure 5.4(c), which shows a typical feature as a p-n junction diode. The lowest reverse current of 100 pA and a highest forward current of 3 μ A can be observed. The rectification ratio of the device can be well controlled by varying the V_g , which increases as V_g decreases. The largest rectification ratio of our device reaches 10^4 at $V_g = -60$ V, indicating a p-n junction is formed. The operation mechanisms of the device can be understood through the corresponding schematic band diagram which is depicted in Figure 5.4(d). The values of the work function of Pd, Ti, WSe₂, and MoSe₂ are obtained from Reference [199]. According to Anderson's rule, after they contact each other, the band alignment is established as shown in Figure 5.4(d). The bottom of the conduction band and the top of the valence band of WSe₂ (MoSe₂) are 3.61 eV (3.91 eV) and 5.25 eV (5.47 eV), and thus the offsets of the conduction band (ΔE_c) and valence band (ΔE_v) are about ~0.3 eV and 0.22 eV respectively.

Several figures of the merit are usually used to evaluate the performance of photodetectors, such as responsivity (R), detectivity (D), external quantum efficiency (EQE), normalized photocurrent-to-dark current ratio ($NPDR$), speed and the operational bandwidth.[90, 175, 177, 200-202]

The I_{ph} can be defined as

$$I_{ph} = I_{total} - I_{dark} = \Gamma \eta e G = \Gamma \eta e G \tau_{carrier} \mu V_d / L^2$$

where I_{total} is the I_d which is measured under the exposure, Γ is the absorbed number of photons per unit time, η is the quantum efficiency of a photon to electron excitation, e is the charge of an electron.[177, 200] From the equation we can obtain the linear dependence of I_{ph} on photon flux, carrier lifetime, carrier mobility and the external bias voltage.

The R is the ratio of I_{ph} and P_{laser} . It indicates the ability of a photodetector that can convert from the defined optical excitation power to the electric signal. It can be expressed as:

$$R = I_{ph} / P_{laser} = \Gamma \eta e G \tau_{carrier} \mu V_d / L^2 / (\Gamma_{total} / \lambda)$$

D is the parameter for comparing the detection performance of different photodetectors.[13] It can be expressed as

$$D = A^{1/2} R / (2eI_d)^{1/2}$$

where A is the efficient photodetection area.

The EQE is the ratio of the photon-excited carriers (n_e) and the total incident photon flux (n_{total}) and can be expressed as

$$EQE = n_e / n_{total} = (I_{ph} / e) / (P_{laser} / hv) = R h c / e \lambda$$

where ν is the frequency of the incident light, h is the Plank constant.[13] Generally speaking, the EQE of the photoconductive mode is determined by the $\tau_{transist}$ and the $\tau_{carrier}$. In this term,

the EQE larger than unity is possible if the $\tau_{\text{carrier}} > \tau_{\text{transist}}$, where the excess carrier will circulate in the channel many times before they recombine. For the photovoltaic mode, the EQE is usually smaller than the unity when the device is zero biased or forward biased. However, when the device is biased with sufficient large reverse bias voltage, the breakdown will occur, the photon-excited carrier will gain sufficient energy initial impact ionization, resulting in the EQE larger than unity.

The $NPDR$ is the parameter that indicates the ability which suppresses the dark current without sacrificing the R of a photodetector.[203] It can be expressed as

$$NPDR = (I_{\text{ph}}/I_{\text{dark}})/P_{\text{laser}}$$

The speed of the photodetector is assessed by the rise time (τ_r) and the fall time (τ_f) of its response to a pulse signal.[204] The τ_r/τ_f is the time interval for the response to rise/decay from 10 to 90%/90 to 10% of its peak value.[205] The speed of the commercial Si photodetector is in the range of 50 ps.[206] Fast response of the photodetector is important in the field of telecommunication, whereas, in the field of sensing imaging, moderate speed is enough.

The photodetection operational bandwidth indicates which part of the electromagnetic spectrum can be detected. It limits by the bandgap of the active material; for example, the commercial Si photodetector cannot detect the wavelengths which are longer than 1100 nm.

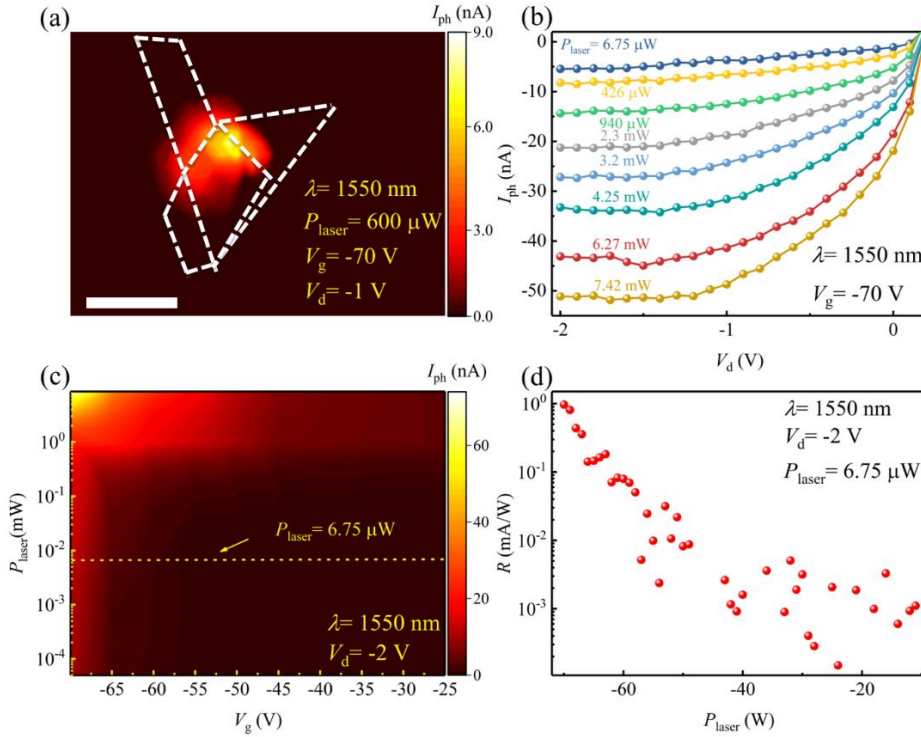


Figure 5.5. (a) Photocurrent mapping of the heterostructure. The white dotted regions represent the flakes in Figure 5.4(b). (b) $I_{\text{ph}}-V_d$ of the $\text{MoSe}_2/\text{WSe}_2$ heterojunction. (c) Photocurrent dependences on the V_g and P_{laser} . (d) Responsivity dependence on the gate voltage. The scale bar is 10 μm . Publication II.

The photoresponse characteristics of our device are then studied. Scanning photocurrent measurement with a 1550-nm laser is carried out firstly with a confocal optical microscope (Objective 100 X, NA= 0.75). As shown in Figure 5.5(a), a pronounced photocurrent generation can be observed from the heterojunction ($V_d = -1$ V, $V_g = -70$ V and $P_{\text{laser}} = 600$ μW). Note that,

there is no detectable photocurrent when the device is forward bias due to the lower band-bending level of the heterojunction. The non-uniform photocurrent can be attributed to the inhomogeneous contacts between the two flakes. All the following measurements are carried out by locating the laser spot at the position where the largest photocurrent generates.

The I_{ph} - V_d characteristics of the device under various laser powers, ranging from 6.75 μ W to 7.42 mW with a fixed gate voltage of -70 V, is depicted in Figure 5.5(b). Two photocurrent generation mechanisms can be observed from Figure 5.5(b) which are photoconductive effect and photovoltaic effect. The photocurrent shows a strong dependence on the drain voltage due to the increased photo-excited carrier drift velocity. The relationship between photocurrent and laser power as well as the gate voltage is shown in Figure 5.5(c), where the magnitude of the photocurrent increases with decreasing gate voltage and increasing laser power. For example, only when the gate voltage is smaller than -62 V, the photocurrent becomes prominent. The performance of the photodetector can be evaluated through several figures of the merits, such as photoresponsivity and the normalized photocurrent-to-dark current ratio. The relationship between gate voltage and photoresponsivity at $P_{laser} = 6.75 \mu$ W and $V_d = -2$ V is depicted in Figure 5.5(d). The R decreases as gate increases indicating the larger R can be easily achieved by decreasing the gate voltage.

The photoresponse of the device at 980 nm is also analyzed. Photoresponse at 980 nm is quite similar to that at 1550 nm indicates that the absorption of the heterostructure at these two wavelengths should be almost the same. This is then confirmed from measured absorption results. The comparisons of the photoresponsivity at 532 nm, 980 nm and 1550 nm with the same bias conditions are depicted in Figure 5.6(a).

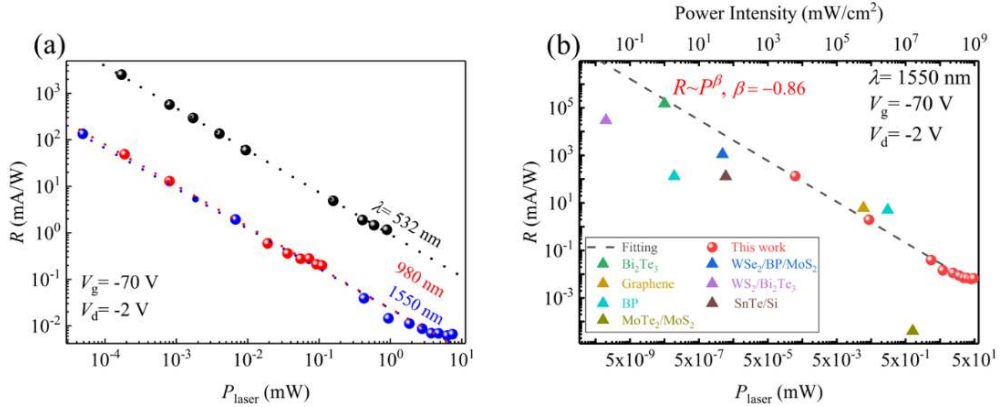


Figure 5.6. (a) Summary of responsivity dependence of incident power at the wavelengths of 532 nm, 980 nm, and 1550 nm. (b) Responsivity comparison of this work and typical published results (i.e. Bi_2Te_3 , [207] Graphene, [208] WS_2/Bi_2Te_3 , [209] $WSe_2/BP/MoS_2$, [210] $SnTe/Si$, [211] $MoTe_2/MoS_2$, [198] and BP [212, 213]) at the wavelength of 1550 nm. Publication II.

The saturation of electron-hole pair generation at higher incident laser powers and the increased surface recombination in the underlying SiO_2 result in R decreases with increasing P_{laser} . The maximum responsivity of our photodetector is 2 A/W at 532 nm ($P_{laser} = 100$ nW), 150 mA/W at 980 nm ($P_{laser} = 50$ nW) and 127 mA/W at 1550 nm ($P_{laser} = 50$ nW), when $V_g = -70$ V and $V_d = -2$ V. A 40-time difference of R at 532 nm and 1550 nm according to the fitted results is observed. It is because the absorption of the heterojunction at 532 nm is higher than that at 1550 nm. The maximum NPDR is $\sim 2 \times 10^9$ mW $^{-1}$ at 532 nm, 2.5×10^4 mW $^{-1}$ at 980 nm and 1.9×10^4 mW $^{-1}$ at 1550 nm, respectively. By fitting the curve of Figure 5.6(b) with the equation

of $R \sim P^\beta$, the term β is obtained as -0.9 for 532 nm, -0.88 for 980 nm, and -0.86 for 1550 nm. The deviation of β from 1 indicates the loss of photon-excited carriers, possibly due to the defects at the interface of the heterojunction. Through the comparison (Figure 5.6 (b)) between our proposed devices with those published with small band-gap materials, our device shows promising performance in IR wavelengths.

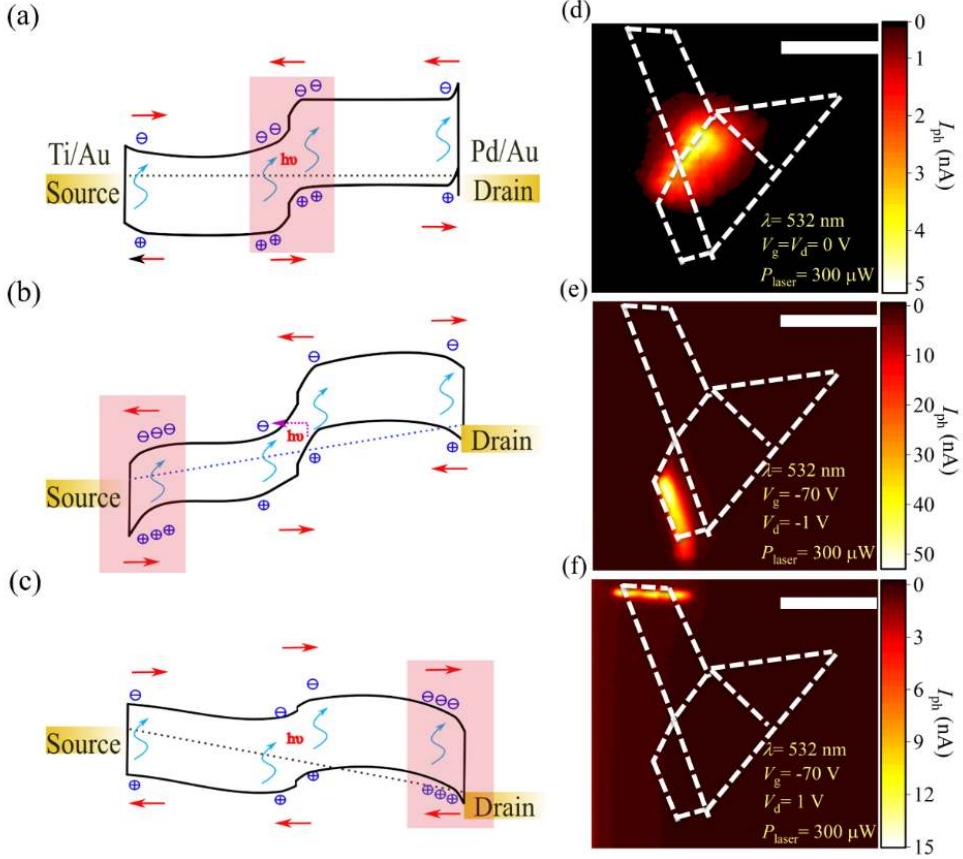


Figure 5.7. (a-c) Band diagram of heterojunction and Schottky junctions, where (a) $V_g = V_d = 0$ V, (b) $V_g = -70$ V, $V_d = -1$ V and (c) $V_g = -70$ V, $V_d = 1$ V. The red arrows indicate the carrier movement direction. The blue arrows indicate the electron-hole pairs separation process. The pink rectangle regions indicate the position of the strongest built-in electric field. (d-f) Photocurrent mapping of the heterojunction under different bias conditions. The dashed lines outline the flakes and heterojunction. Publication II.

Photocurrent mapping at 532 nm of the heterojunction and corresponding band diagrams are plotted to help us understand the photocurrent generation mechanisms. When there is no external bias (i.e., $V_d = V_g = 0$ V) and the laser is on, photo-generated electron-hole pairs are generated and separated at the heterojunction region, due to the existing of the built-in electric field (Figure 5.7(a)). The photo-excited electrons move towards MoSe₂ and holes towards WSe₂ separately, resulting in the positive V_{oc} and negative I_{sc} . Corresponding photocurrent mapping result is shown in Figure 5.7(d), showing the prominent photocurrent is generated in the overlapped region. No obvious photocurrent is observed at the heterojunction region due to the low band-bending in these regions when the device is reversed biased at the gate voltage of -70 V (Figure 5.7(b)). The prominent photocurrent generation position shifts to the source contact

region. This is because the Schottky diode of the source contact is forward biased and the direction of the built-in electric field is in the same direction as the external field. However, when the device is forward biased (Figure 5.7(c)), the maximum photocurrent generation position moves to the drain part, due to the same direction of the built-in electric field and external field, leading to the more efficiently dissociating of the electron-hole pairs.

The gate-tunable photoresponse of our device at the telecommunication wavelengths can be explained by the above analysis. Although the band gap of the two individual flakes and the interlayer band gap of the heterojunction are far beyond 0.8 eV, by properly gating and biasing the device, the sub-bandgap photodetection can be achieved through the tunneling-assisted transition. The increased band-bending which results from the reverse bias and large negative gate voltage has the potential to allow the photo-excited electrons of the WSe_2 to the conduction band of MoSe_2 . The high electrostatic field, leading to the edges of the conduction band and valence band is tilted along the direction of the electric field, and thus the wave functions have a tail extending into the bandgap region. Since the absorption coefficient is proportional to the magnitude square of the overlap integral of the e - h wave functions, the tunneling tails significantly enhance the e - h interactions with sub-bandgap photons, contributing to the tunneling-assisted transition in the band-bending heterojunction area. In our device, when a 10^5 - 10^6 V/cm electrical field is applied together with the high built-in electric field, the tunneling-assisted transition occurs, resulting in the sub-band response.

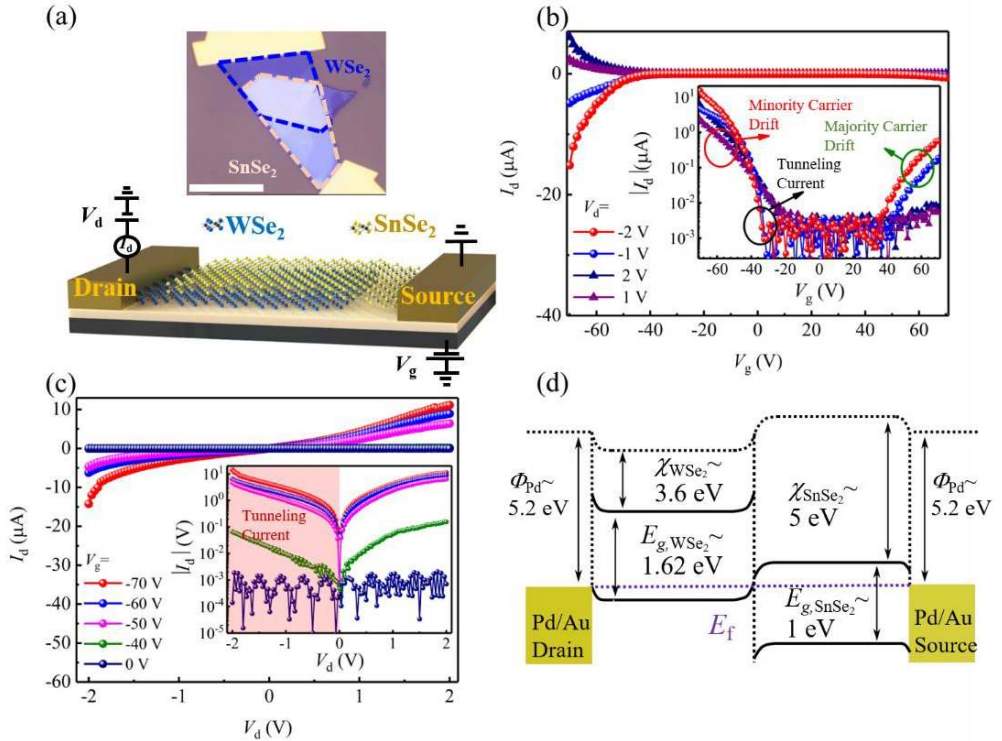


Figure 5.8. WSe₂/SnSe₂ heterojunction-based photodetector. (a) Microscopic image (upper panel) and schematic illustration (bottom panel) of the heterojunction device. (b) I_d - V_g characteristics measured with variable V_d in dark. Inset: $|I_d|$ - V_g characteristics on the logarithmic scale. (c) I_d - V_d characteristics measured with variable V_g in dark. Inset: $|I_d|$ - V_d characteristics on the logarithmic scale. (d) The schematic band diagrams of the heterojunction. Publication I.

5.2.2 WSe₂/SnSe₂ heterojunction based photodetector

Although the MoSe₂/WSe₂ based heterostructure enables the photodetection at the telecommunication wavelengths, the performance of the photodetector (such as photoresponsivity and detectivity) still needs further improvement. According to the differences of the interfaces, band alignments can be classified into three types: type-I, type-II, and type-III band alignment.[78, 80] Most of the reported photodetectors are based on type-II band alignment mainly due to its high electron-hole pair separation efficiency. Recently, type-III band alignment has been explored as a platform for tunneling field effect transistors (TFETs) due to the enhanced tunneling current density (e.g., 5.7 A/W under 660 nm,[214] 244 A/W under 550 nm,[215] 180 A/W under 405 nm[216]).[121, 217, 218] However, the applications of the type-III band alignment TFETs in the field of broadband photodetection are rarely reported.

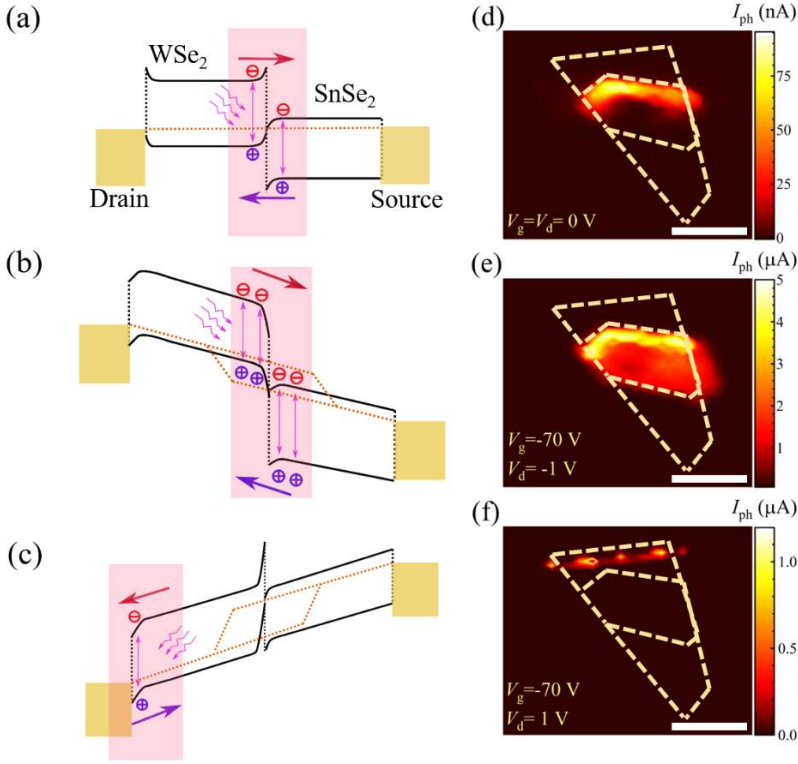


Figure 5.9. (a-c) Band diagram of heterojunction and Schottky junctions, where (a) $V_g = V_d = 0$ V, (b) $V_g = -70$ V, $V_d = -1$ V and (c) $V_g = -70$ V, $V_d = 1$ V. The red/purple arrows indicate the carrier movement direction. The magenta arrows indicate the electron-hole pairs separation process. The pink rectangle regions indicate the position of the strongest built-in electric field. (d-f) Photocurrent mapping of the heterojunction under different bias conditions at 532 nm. $P_{\text{laser}} = 50 \mu\text{W}$ ($8.5 \times 10^3 \text{ W/cm}^2$). The dashed lines outline the flakes and heterojunction. The scale bar is 10 μm . Publication I.

A WSe₂ multi-layer flake is firstly prepared by mechanical exfoliation method from a bulk crystal. The exfoliated WSe₂ flake is transferred to a Si/SiO₂ substrate. A multi-layer SnSe₂ flake is then exfoliated with the same method and stacked on top of the WSe₂ flake. Pd/Au metal electrodes are then patterned on the flakes as the drain and source contacts. Here, Pd will efficiently inject holes to WSe₂ and electrons to SnSe₂ separately. The optical image and the schematic illustration are shown in Figure 5.8(a). The thickness of the exfoliated flakes are

measured by AFM, giving the value of 6 nm for WSe₂ and 15 nm for SnSe₂. Raman spectrum is employed to characterize the quality of the fabricated device.

The electrical properties of the device are shown in Figure 5.8(b), where p-type transport characteristics can be observed. The gate-controlled drain to source current shows an on-off ratio of 10⁴, due to the ultrathin nature of the transferred flakes of which the carriers can be tuned by the external gate voltage. With reverse bias, the band-to-band tunneling current can be observed when the gate voltage smaller than -30 V, of which the magnitude decreases with decreasing gate voltage, while the reverse current at gate voltage larger than 40 V could be attributed to the majority carriers drifting. The forward current observed at gate voltage smaller than -30 V is owing to the minority carrier drifting. Both positive and negative gate voltage leads to the increasement of the reverse current and the maximum value of 15 μ A I_d is found at $V_d=-2$ V, $V_g=-70$ V. The gate-dependent current-voltage (I_d - V_d) characteristics are shown in Fig. 5.8(c), where two important features can be observed. First, owing to the ultrathin nature of the heterojunction, the magnitude of both $I_{forward}$ and $I_{reverse}$ can be significantly controlled by modifying the gate voltage. Second, since the breakdown voltage (i.e., 0.01 V) is too much less than $4E_g/q$, where E_g is the band gap of the semiconductors (1.62 eV of WSe₂ and 1 eV of SnSe₂), and q is the electron charge, the tunneling current (red region in the inset of Fig. 1c) can be attributed to the Zener tunneling.[219]

The qualitative band alignment of the device at zero bias is shown in Figure 5.8(d) based on the reported work function of Pd and electron affinity values of WSe₂ and SnSe₂. The Fermi level of the WSe₂ locates at the valence band maximum, and that of SnSe₂ locates at the conduction band minimum. Thus, the near-broken band alignment is formed. The bottom of the conduction band and the top of the valence band of WSe₂ (SnSe₂) are 3.6 eV (5.22 eV) and 5 eV (6 eV) so that the offsets of the conduction band and valence band are about 1.7 eV and 1.5 eV, respectively.

The electrical property can be understood through the corresponding band diagrams (Figure 5.9(a-c)). The high Schottky barrier at the drain part (Pd-WSe₂) restrains the carries flowing when there is no gate voltage, as shown in Figure 5.9(a). The device under this condition can be seen as a p-n junction in series with a Schottky contact. When a negative gate voltage is applied, a near-ohmic contact is formed at the drain part, and the direction of the band-bending at this part shifts down. When a reverse bias voltage is applied, the valence band maximum shifts above the conduction minimum of the SnSe₂, where the electrons in the valence band of WSe₂ can tunnel to the conduction band of SnSe₂, leading to the band to band tunneling (BTBT) current (Figure 5.9(b)). The tunneling current can be further enlarged by increasing the reverse bias voltage. When a forward bias is applied, however, the barrier height at the overlapped region is lowered, the majority carriers of the SnSe₂ can overcome the interface barrier and drift to the WSe₂, resulting in the forward current (Figure 5.9(c)).

To verify the analysis of the electric properties of the device, scanning photocurrent mapping is then performed, as shown in Figure 5.9(d-f). First the 532 nm laser is utilized under a confocal optical microscopy (Objective 100X, NA=0.75, $P_{laser}=50$ μ W (corresponding to a power intensity of 8.5×10^6 mW/cm²)). The spot size of the laser spot is estimated as 0.6 μ m², which is smaller than the size of the heterojunction. When there is no external bias, and the laser is on, the electron-hole pairs are generated and separated mainly at the heterojunction, as shown in Figure 5.9(d). The photon-excited electrons move to SnSe₂ and holes move to WSe₂. With reverse bias and a negative gate voltage, as have mentioned, the reverse current is dominated by the BTBT effect, and the band alignment goes from type-II to type-III band alignment. The

photocurrent which generates at this condition is around 50 times larger than that generated at the zero bias condition, due to the enlarged band-bending at the heterojunction (Figure 5.9(e)). However, when the device is forward bias with the negative gate voltage, the band-bending at the overlapped region is realized, and that at drain part is increased. Thus, the prominent photocurrent generation shifts to the drain part, as shown in Figure 5.9(f).

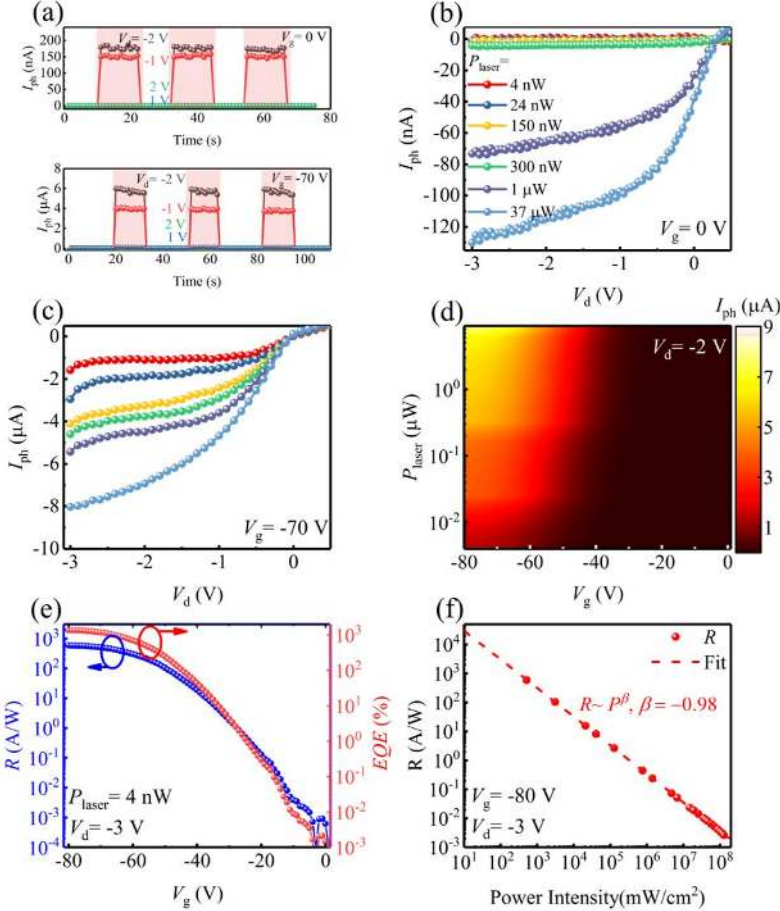


Figure 5.10. (a) Photo switching characteristics of the WSe₂/SnSe₂ heterojunction device at different V_d . I_{ph} - V_d characterization of the WSe₂/SnSe₂ heterojunction at (b) $V_g = 0$ V and (c) $V_g = -70$ V at 532 nm. (d) I_{ph} dependence of the V_g and P_{laser} . (e) R and EQE dependence of V_g . (f) R measured with different input power intensities. Publication 1.

We further investigate the photoresponse of our device under 532 nm laser. The measurement is conducted when the laser spot is located at the heterojunction position where the largest photocurrent is generated. The time-dependent photocurrent under chopped laser ($P_{laser} = 10 \mu W$) is first tested at zero gate voltage and -70 V gate voltage, respectively. The fast photoresponse can be observed from Figure 5.10(a) where the rise and fall edges are steep. Moreover, when the device is reversed biased, the generated photocurrent is more significant than that of the forward bias, due to the increased band-bending. This perfectly matches the photocurrent mapping results. The magnitude of I_{ph} at $V_g = -70$ V is around 38 times larger than that of $V_g = 0$ V at $P_{laser} = 10 \mu W$, indicating that the V_g plays a crucial role in the generation

of I_{ph} . Since the device shows photodiode behavior, in the next paragraph we will only focus on the photocurrent at the reversed bias condition.

The I_{ph} - V_d curves of the heterostructure with fixed gate voltages ($V_g = 0$ V and $V_g = -70$ V) under the $\lambda = 532$ nm laser with the laser power varying from 4 nW to 37 μ W are shown in Figure 5.10(b-c). The photocurrent increases as the decreasing of the V_d , due to the increased carrier drift velocity and electron-hole pair separation efficiency. When the incident laser power is increased, the photocurrent is increased and a value of 8 μ A at $V_d = -3$ V and $V_g = -70$ V is achieved. A 62-fold increase of photocurrent can be observed in Figure 5.10(b-c), suggesting the gate voltage is a key part for the photocurrent generation. The photocurrent as a function of laser power and the gate voltage is shown in Figure 5.10(d), where photocurrent increases as the gate voltage decreases and laser power increase. For example, when $P_{laser} = 0.1$ μ W, the photocurrent is remarkable (~ 2 μ A) only when $V_g < -55$ V, confirming that smaller V_g leads to a larger photocurrent.

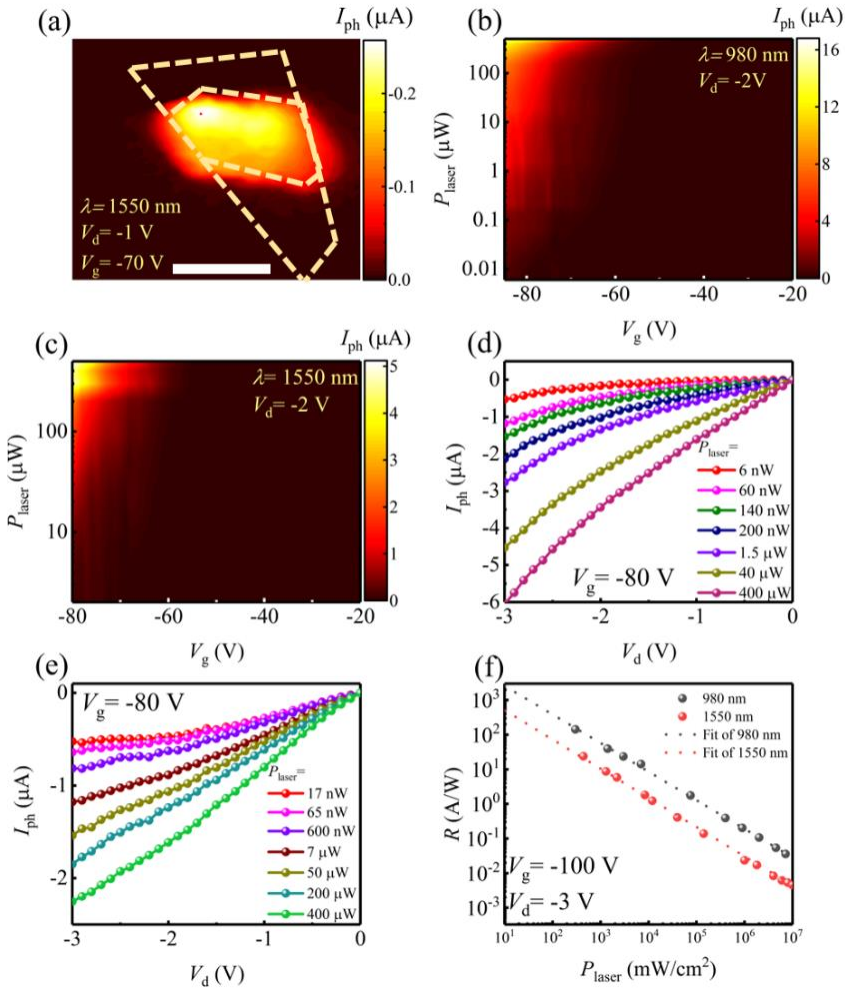


Figure 5.11. (a) Photocurrent mapping of the heterojunction under different bias conditions at 1550 nm. $P_{laser} = 10$ μ W (2×10^5 mW/cm²). I_{ph} dependence of the V_g and P_{laser} at (b) 980 nm and (c) 1550 nm. I_{ph} - V_d characterization of the WSe₂/SnSe₂ heterojunction at (d) 980 nm and (e) 1550 nm. (f) R at different input power intensities. The scale bar is 10 μ m. Publication I.

Again, several figures of merits (R , D , and EQE) are used to evaluate the performance of our device. The gate-dependent R and EQE are shown in Figure 5.10(e), where the largest R and EQE could reach to 588 A/W and 1367% at $V_g = -80$ V, respectively. The highest D is estimated to be 1×10^{11} Jones. The corresponding R as a function of incident power intensity is summarized in Figure 5.10(f). It is clearly that the R linearly changes with the P_{laser} in log scale. By fitting the experimental data with the equation of $R \sim P^\beta$, the term β is obtained at -0.98 for 532 nm, indicating the superior photocurrent capability and excellent separation efficiency of photo-induced charge carriers.

Finally, infrared photodetection is analyzed. The corresponding photocurrent mapping under 1550 nm laser with $V_d = -1$ V, $V_g = -70$ V and $P_{\text{laser}} = 10$ mW is shown in Figure 5.11(a). The prominent photocurrent is generated at the heterojunction, matching well with our previous analysis. The gate-dependent photoresponse of the device under 980 nm and 1550 nm lasers are shown in Figure 5.11(b-c). A clear threshold for the IR photoresponse can be observed. For example, at the bias condition $V_d = -2$ V and $P_{\text{laser}} = 10$ μ W, for $\lambda = 980$ nm, the photocurrent is not detectable when the V_g is higher than -60 V. As for the incident light at $\lambda = 1550$ nm, at the same bias condition, this threshold voltage shifts to $V_g = -70$ V. This fascinating phenomenon can be attributed to the tunneling-assisted transition in the band-bending heterojunction. An extremely negative gate voltage and a high reverse bias voltage increase the built-in electric field at the heterojunction, and the edges of the conduction band and valence band are tilted along the direction of the electric field. The electron and hole wave functions will have a tail which will extend into the bandgap, which enhances the e-h interactions with sub-bandgap photons. Thus, under such high built-in electric field, our device has the potential to allow that the photo-excited carriers are generated with photon energy smaller than the intrinsic bandgap of WSe₂ and transferred to the conduction band of SnSe₂. The magnitude of the photocurrent under the 980 nm laser is around 2.6 times larger than that generated under the 1550 nm laser due to that the photon energy of 980 nm is higher than that of 1550 nm. Note that there is no photoresponse of our device when it is forward biased even when the device is exposed with an intense light. Figures 5.11(d-e) show the $I_{\text{ph}}-V_d$ curves of the heterostructure with a fixed gate voltage ($V_g = -70$ V) under the $\lambda = 980$ nm and 1550 nm lasers with the laser power varying from 6 nW to 400 μ W and 17 nW to 400 μ W, respectively. The magnitude of the I_{ph} shows a strong dependence on the reversed bias voltage. This results from the larger built-in electric field at the larger reversed bias voltage. Figure 5.11(f) depicts the R of the device under $\lambda = 980$ and 1550 nm as the function of the laser intensity.

The maximum R of our device (according to the fitting results) is 396 A/W at 980 nm and is 80 A/W at 1550 nm ($P_{\text{laser}} = 100$ mW/cm²), which is superior to the previously reported 2D materials based photodetectors (see Figure 5.12(a-b)). The highest detectivities at these two wavelengths are 4.4×10^{10} Jones and 1.4×10^{10} Jones, respectively. The time-dependent I_{ph} under a pulsed light illumination (at 1550 nm) is performed (Figure 5.12(c)). The rise time and the decay time are 16 and 45 ms, respectively. We believe the speed of the device can be further improved by improving the quality of the fabricated device.

Comparing our WSe₂/SnSe₂ with WSe₂/MoSe₂ heterojunction device, a 10 times larger photoresponsivity is observed in the wavelength of 1550 nm. This should be contributed to the WSe₂/SnSe₂ based photodetector possesses a higher built-in electric field at the heterojunction than that of WSe₂/MoSe₂ photodetector under the same bias conditions. In this term, by properly choosing 2D layered materials to form a type-III band alignment based heterojunctions, one can obtain a high performance broadband photodetector. This could also enable a deep

understanding of the band engineering technology in the vdW heterostructures possible for other applications (e.g., modulators).

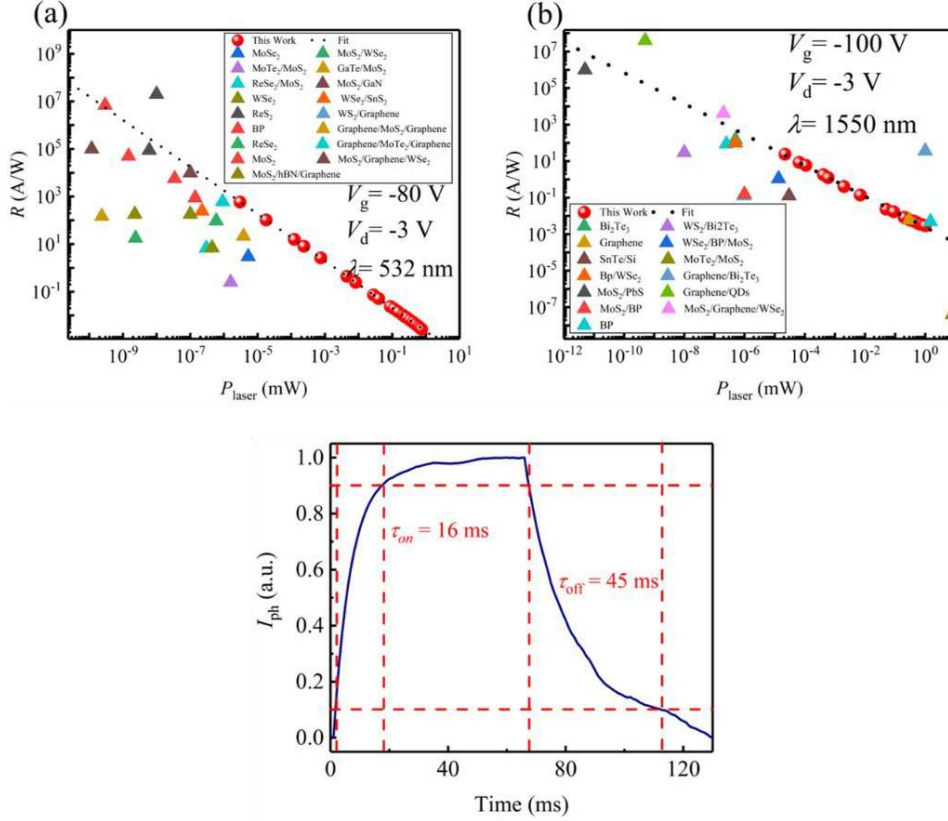


Figure 5.12. (a) Photoresponsivity comparison of the WSe₂/SnSe₂ heterojunction device and typical previous results (i.e. MoS₂, [220-222] MoSe₂, [223] MoS₂/WSe₂, [224] MoTe₂/MoS₂, [198] GaTe/MoS₂, [225] ReSe₂/MoS₂, [226] MoS₂/GaN, [227] WSe₂, [228] WSe₂/SnS₂, [215] WS₂/Graphene, [229] ReS₂, [230, 231] BP, [232] ReSe₂, [233] Graphene/MoS₂/WS₂/Graphene, [234] MoS₂/Graphene/WSe₂, [86] and MoS₂/hBN/Graphene [216]) at $\lambda = 532$ nm. (b) Photoresponsivity comparison of this work and typical previous results (i.e. WSe₂/BP/MoS₂, [210], Bi₂Te₃, [207] WS₂/Bi₂Te₃, [209] Graphene, [208] BP, [212, 213, 232, 235] SnTe/Si, [211] MoTe₂/MoS₂, [198] BP/WSe₂, [236] Graphene/Bi₂Te₃, [237] MoS₂/PbS, [238] MoS₂/BP, [239] and MoS₂/Graphene/WSe₂ [86]) at $\lambda = 1550$ nm. Publication I.

The compelling demand for high-performance, low power consumption and easiness of fabrication in current integrated photonics systems is the main driving force of industry's quest for new materials. In my thesis, the gate controlled tunneling mechanism of Type-III band alignment leads to subthreshold swings below the thermionic MOSFET limit at room temperature, which allows the reduction of power supply voltage while maintaining a comparable performance. In this manner, TMDs heterostructures with a Type-III band alignment is a promising candidate for the next generation of photonic systems due to their potential to reduce power consumption and the easiness in fabrication. Currently, the huge research efforts have been given on 2D materials-based photonics and optoelectronics, which will solve the challenges, such as scaling-down of the FETs, the device integration process, and power consumption issues which are facing by the state-of-the-art silicon technologies.

6. Summary and outlook

2D layered materials, such as graphene and TMDs, have become one of the hottest research topics since the discovery of graphene in 2004.[95, 240, 241] They exhibit remarkable optical and electrical properties. Moreover, these excellent properties can be tuned by applying external electrostatic fields, doping, and strain. They can even be stacked together to form the heterojunctions with desired functions regardless of the thermal and lattice mismatch problems. Owing to these, different kinds of optoelectronic devices based on 2D layered materials have been demonstrated, including photodetectors, optical modulators, ultrafast lasers, and LEDs.

In this thesis, the production methods of 2D layered materials are introduced. Specifically, the transfer methods of CVD graphene and exfoliated TMDs are carefully discussed. The EBL, ALD and RIE processes which are used for optoelectronic device integration are also introduced. The Raman and PL spectra are used to identify the quality of the exfoliated TMDs before and after the fabrication process. AFM is employed to identify the thickness of the exfoliated TMD flakes. The characterization methods of electrical and optical properties of the proposed devices are examined.

Utilizing monolayer CVD graphene, graphene-based electro-optic modulators are fabricated. For the GEOM which is made on the quartz substrate, the measured single-pass optical transmittance increases from 85.51% to 86.77% (corresponding to 1.26% absorption change) when the electrical voltage varies from 0 to 5 V. As for the GEOM which is made as a reflective multilayer structure with a dielectric layer placed between a mirror and graphene, it increases the modulation depth at a low drive voltage. By carefully adjusting the thickness of the insulating layer (HfO_2), it allows tailored linear absorption of graphene from almost 0% (when graphene is placed in the node) up to 9.2% (when placed precisely in the antinode of the standing wave, which corresponds to a $\lambda/4$ distance). The modulation depth of 1.94% is obtained, when the voltage changes from -5 up to 5 V. A 3 dB bandwidth is measured as 13.2 MHz.

Photodetectors based on TMD vdW heterojunctions are also studied in this thesis. The photodetectors which are one of the most important optoelectronic devices have been widely employed in communication, imaging, security, and sensing. However, the operation bandwidth of photodetector is typically limited by the bandgap of the used materials. By stacking different individual materials, a vdW heterojunction can be formed, offering a new dimension in breaking this intrinsic bandgap barrier.

In this work, by using the transfer stage, a $\text{WSe}_2/\text{MoSe}_2$ heterojunction was prepared. With proper electrical gating and bias, the heterojunction exhibits high-sensitivity photodetection with the operation wavelength extended up to the telecommunication band (i.e., 1550 nm). The photoresponsivity and normalized photocurrent-to-dark current ratio reach up to 127 mA W^{-1} and $1.9 \times 10^4 \text{ mW}^{-1}$, respectively. To further improve the performance of the broadband photodetector, a $\text{WSe}_2/\text{SnSe}_2$ photodetector was also demonstrated. By applying a large negative

back gate voltage and a reversed bias voltage, the heterojunction band structure changes from type-II to type-III band alignment and a band to band tunneling phenomenon appears. The increased band bending at the heterojunction results in the tunneling-assisted transition which allows that the photons with energy smaller than the bandgap of the WSe_2 tunnel to the conduction band of SnSe_2 for effective photodetection. Under the type-III band alignment condition, our heterojunction device shows ultrahigh photo-responsivity up to ~ 588 A/W at the wavelength of 532 nm and ~ 88 A/W at the wavelength of 1550 nm. The corresponding photo-detectivity reaches 4.4×10^{10} Jones and 1.4×10^{10} Jones for visible and near-infrared wavelengths, respectively.

2D layered materials based optoelectronic devices have shown various encouraging performances. However, there are still many challenges left in their applications. For example, in the field of photodetection, where most common photodetectors are based on p-n junctions, they always exhibit fast response speed but low responsivity due to the low carrier concentration. The TFETs based photodetectors can overcome this shortcoming. However, it highly depends on the quality of the interfaces of the vdW heterojunction, which is not easily controllable at the moment. Hence, to obtain high-performance TFETs based photodetectors, the controllable fabrication methods for the interface should be further studied.

As an outlook of this thesis, we list some of the valuable research directions in the relevant fields:

- (1) Modulators with 2D layered materials other than graphene, such as black phosphorus and TMDs demand more attentions due to their unique band structures and spectral responses.
- (2) By integrating with the waveguides, plasmonic structures or nanocavities, the performance of the photodetectors can be dramatically improved, deserving further investigation.
- (3) By carefully controlling the twist angles and the quality of the interface, the heterostructure based devices may offer new dimensions for optoelectronic applications.

References

- [1] A. K. Geim and K. S. Novoselov, "The rise of graphene," *Nat. Mater.*, vol. 6, no. 3, pp. 183-91, Mar. 2007.
- [2] F. Bonaccorso, Z. Sun, T. Hasan, and A. C. Ferrari, "Graphene photonics and optoelectronics," *Nat. Photonics*, vol. 4, no. 9, pp. 611-22, Sep. 2010.
- [3] C. Lee, X. D. Wei, J. W. Kysar, and J. Hone, "Measurement of the elastic properties and intrinsic strength of monolayer graphene," *Science*, vol. 321, no. 5887, pp. 385-8, Jul. 2008.
- [4] A. A. Balandin, "Thermal properties of graphene and nanostructured carbon materials," *Nat. Mater.*, vol. 10, no. 8, pp. 569-81, Aug. 2011.
- [5] G. G. Naumis, S. Barraza-Lopez, M. Oliva-Leyva, and H. Terrones, "Electronic and optical properties of strained graphene and other strained 2D materials: a review," *Rep. Prog. Phys.*, vol. 80, no. 9, pp. 1-62, Sep. 2017.
- [6] K. S. Novoselov, V. I. Fal'ko, L. Colombo, P. R. Gellert, M. G. Schwab, and K. Kim, "A roadmap for graphene," *Nature*, vol. 490, no. 7419, pp. 192-200, Oct. 2012.
- [7] A. C. Ferrari *et al.*, "Science and technology roadmap for graphene, related two-dimensional crystals, and hybrid systems," *Nanoscale*, vol. 7, no. 11, pp. 4598-810, Mar. 2015.
- [8] T. Mueller, F. Xia, and P. Avouris, "Graphene photodetectors for high-speed optical communications," *Nat. Photonics*, vol. 4, no. 5, pp. 297-301, May 2010.
- [9] X. Huang *et al.*, "Graphene-Based Materials: Synthesis, Characterization, Properties, and Applications," *Small*, vol. 7, no. 14, pp. 1876-902, Jul. 2011.
- [10] S. J. Kim, K. Choi, B. Lee, Y. Kim, and B. H. Hong, "Materials for Flexible, Stretchable Electronics: Graphene and 2D Materials," *Annu. Rev. Mater. Res.*, vol. 45, no. 1, pp. 63-84, Apr. 2015.
- [11] A. Kumar and C. W. Zhou, "The Race To Replace Tin-Doped Indium Oxide: Which Material Will Win?," *ACS Nano*, vol. 4, no. 1, pp. 11-14, Jan. 2010.
- [12] S. Yu, X. Wu, Y. Wang, X. Guo, and L. Tong, "2D Materials for Optical Modulation: Challenges and Opportunities," *Adv. Mater.*, vol. 29, no. 14, p. 1606128, Apr. 2017.
- [13] Z. H. Sun and H. X. Chang, "Graphene and Graphene-like Two-Dimensional Materials in Photodetection: Mechanisms and Methodology," *ACS Nano*, vol. 8, no. 5, pp. 4133-56, May 2014.
- [14] Z. K. Liu, S. P. Lau, and F. Yan, "Functionalized graphene and other two-dimensional materials for photovoltaic devices: device design and processing," *Chem. Soc. Rev.*, vol. 44, no. 15, pp. 5638-79, Dec. 2015.
- [15] Z. P. Sun, "Electrically tuned nonlinearity," *Nat. Photonics*, vol. 12, no. 7, pp. 383-5, Jul. 2018.
- [16] S. Aksimsek, H. Jussila, and Z. P. Sun, "Graphene-MoS₂-metal hybrid structures for plasmonic biosensors," *Opt. Commun.*, vol. 428, pp. 233-9, Dec. 2018.
- [17] H. Hu, X. Guo, D. Hu, Z. Sun, X. Yang, and Q. Dai, "Flexible and Electrically Tunable Plasmons in Graphene-Mica Heterostructures," *Adv. Sci.*, vol. 5, no. 8, p. 1800175, Aug. 2018.
- [18] A. Autere, H. Jussila, Y. Dai, Y. Wang, H. Lipsanen, and Z. Sun, "Nonlinear Optics with 2D Layered Materials," *Adv. Mater.*, vol. 30, no. 24, p. 1705963, Jun. 2018.

- [19] X. Yang *et al.*, "Nanomaterial-Based Plasmon-Enhanced Infrared Spectroscopy," *Adv. Mater.*, vol. 30, no. 20, p. e1704896, May 2018.
- [20] T. Juntunen *et al.*, "Inkjet Printed Large-Area Flexible Few-Layer Graphene Thermoelectrics," *Adv. Funct. Mater.*, vol. 28, no. 22, p. 1800480, May 2018.
- [21] R. D. Wang *et al.*, "All-Optical Intensity Modulator by Polarization-Dependent Graphene-Microfiber Waveguide," *IEEE Photonics J.*, vol. 9, no. 6, Dec. 2017.
- [22] Z. P. Sun, A. Martinez, and F. Wang, "Optical modulators with 2D layered materials," *Nature Photonics*, vol. 10, no. 4, pp. 227-238, Apr. 2016.
- [23] J. Z. Wang *et al.*, "High-energy and efficient Raman soliton generation tunable from 1.98 to 2.29 μm in an all-silica-fiber thulium laser system," *Opt. Lett.*, vol. 42, no. 18, pp. 3518-21, Sep. 2017.
- [24] H. Jussila *et al.*, "New Approach for Thickness Determination of Solution-Deposited Graphene Thin Films," *ACS Omega*, vol. 2, no. 6, pp. 2630-8, Jun. 2017.
- [25] H. Hu *et al.*, "Far-field nanoscale infrared spectroscopy of vibrational fingerprints of molecules with graphene plasmons," *Nat. Commun.*, vol. 7, p. 12334, Jul. 2016.
- [26] X. H. Li *et al.*, "Single-wall carbon nanotubes and graphene oxide-based saturable absorbers for low phase noise mode-locked fiber lasers," *Sci. Rep.*, vol. 6, p. 25266, Apr. 2016.
- [27] X. H. Li *et al.*, "High-power graphene mode-locked Tm/Ho co-doped fiber laser with evanescent field interaction," *Sci. Rep.*, vol. 5, p. 16624, Nov. 2015.
- [28] X. Yang *et al.*, "Far-Field Spectroscopy and Near-Field Optical Imaging of Coupled Plasmon-Phonon Polaritons in 2D van der Waals Heterostructures," *Adv. Mater.*, vol. 28, no. 15, pp. 2931-8, Apr. 2016.
- [29] X. M. Liu, Y. D. Cui, D. D. Han, X. K. Yao, and Z. P. Sun, "Distributed ultrafast fibre laser," *Sci. Rep.*, vol. 5, p. 9101, Mar. 2015.
- [30] H. Jussila, H. Yang, N. Granqvist, and Z. P. Sun, "Surface plasmon resonance for characterization of large-area atomic-layer graphene film," *Optica*, vol. 3, no. 2, pp. 151-8, Feb. 2016.
- [31] L. F. Li *et al.*, "High repetition rate Q-switched radially polarized laser with a graphene-based output coupler," *Appl. Phys. Lett.*, vol. 105, no. 22, p. 221103, Dec. 2014.
- [32] C. M. Huang, F. W. Ye, Z. P. Sun, and X. F. Chen, "Tunable subwavelength photonic lattices and solitons in periodically patterned graphene monolayer," *Opt. Express*, vol. 22, no. 24, pp. 30108-17, Dec. 2014.
- [33] B. Fu, Y. Hua, X. S. Xiao, H. W. Zhu, Z. P. Sun, and C. X. Yang, "Broadband Graphene Saturable Absorber for Pulsed Fiber Lasers at 1, 1.5, and 2 μm ," *IEEE J. Sel. Top. Quantum Electron.*, vol. 20, no. 5, pp. 411-5, Sep. 2014.
- [34] T. J. Echtermeyer *et al.*, "Photothermoelectric and photoelectric contributions to light detection in metal-graphene-metal photodetectors," *Nano Lett.*, vol. 14, no. 7, pp. 3733-42, Jul. 2014.
- [35] L. F. Li *et al.*, "High-power diode-side-pumped Nd:YAG solid laser mode-locked by CVD graphene," *Opt. Commun.*, vol. 315, pp. 204-7, Mar. 2014.
- [36] C. A. Zaugg *et al.*, "Ultrafast and widely tuneable vertical-external-cavity surface-emitting laser, mode-locked by a graphene-integrated distributed Bragg reflector," *Opt. Express*, vol. 21, no. 25, pp. 31548-59, Dec. 2013.
- [37] R. Mary *et al.*, "Evanescent-wave coupled right angled buried waveguide: Applications in carbon nanotube mode-locking," *Appl. Phys. Lett.*, vol. 103, no. 22, p. 221117, Nov. 2013.
- [38] J. Mertens *et al.*, "Controlling Subnanometer Gaps in Plasmonic Dimers Using Graphene," *Nano Lett.*, vol. 13, no. 11, pp. 5033-8, Nov. 2013.
- [39] A. Martinez and Z. P. Sun, "Nanotube and graphene saturable absorbers for fibre lasers," *Nat. Photonics*, vol. 7, no. 11, pp. 842-5, Nov. 2013.
- [40] L. F. Li *et al.*, "Passively Mode-Locked Radially Polarized Nd-Doped Yttrium Aluminum Garnet Laser Based on Graphene-Based Saturable Absorber," *Appl. Phys. Express*, vol. 6, no. 8, p. 082701, Aug. 2013.
- [41] R. Mary *et al.*, "1.5 GHz picosecond pulse generation from a monolithic waveguide laser with a

- graphene-film saturable output coupler," *Opt. Express*, vol. 21, no. 7, pp. 7943-50, Apr. 2013.
- [42] A. A. Lagatsky *et al.*, "2 μm solid-state laser mode-locked by single-layer graphene," *Appl. Phys. Lett.*, vol. 102, no. 1, p. 013113, Jan. 2013.
- [43] M. Zhang *et al.*, "Tm-doped fiber laser mode-locked by graphene-polymer composite," *Opt. Express*, vol. 20, no. 22, pp. 25077-84, Oct. 2012.
- [44] Z. Sun, T. Hasan, and A. C. Ferrari, "Ultrafast lasers mode-locked by nanotubes and graphene," *Physica E-Low-Dimensional Systems & Nanostructures*, vol. 44, no. 6, pp. 1082-91, Mar. 2012.
- [45] Z. P. Sun and A. C. Ferrari, "NONLINEAR OPTICS Fibre sources in the deep ultraviolet," *Nat. Photonics*, vol. 5, no. 8, pp. 446-7, Aug. 2011.
- [46] D. Popa, Z. Sun, T. Hasan, F. Torrisi, F. Wang, and A. C. Ferrari, "Graphene Q-switched, tunable fiber laser," *Appl. Phys. Lett.*, vol. 98, no. 7, p. 073106, Feb. 2011.
- [47] Z. P. Sun *et al.*, "Graphene Mode-Locked Ultrafast Laser," *ACS Nano*, vol. 4, no. 2, pp. 803-10, Feb. 2010.
- [48] Z. P. Sun *et al.*, "A stable, wideband tunable, near transform-limited, graphene-mode-locked, ultrafast laser," *Nano Res.*, vol. 3, no. 9, pp. 653-60, Sep. 2010.
- [49] D. Popa, Z. Sun, F. Torrisi, T. Hasan, F. Wang, and A. C. Ferrari, "Sub 200 fs pulse generation from a graphene mode-locked fiber laser," *Appl. Phys. Lett.*, vol. 97, no. 20, p. 203106, Nov. 2010.
- [50] T. Hasan *et al.*, "Solution-phase exfoliation of graphite for ultrafast photonics," *Phys. Status Solidi B*, vol. 247, no. 11-12, pp. 2953-2957, Dec. 2010.
- [51] T. Hasan *et al.*, "Nanotube-Polymer Composites for Ultrafast Photonics," *Adv. Mater.*, vol. 21, no. 38-39, pp. 3874-99, Oct. 2009.
- [52] S. Z. Butler *et al.*, "Progress, Challenges, and Opportunities in Two-Dimensional Materials Beyond Graphene," *ACS Nano*, vol. 7, no. 4, pp. 2898-926, Apr. 2013.
- [53] X. Duan, C. Wang, A. Pan, R. Yu, and X. Duan, "Two-dimensional transition metal dichalcogenides as atomically thin semiconductors: opportunities and challenges," *Chem. Soc. Rev.*, vol. 44, no. 24, pp. 8859-76, Dec. 2015.
- [54] H. J. Chuang *et al.*, "High mobility WSe₂ p- and n-type field-effect transistors contacted by highly doped graphene for low-resistance contacts," *Nano Lett.*, vol. 14, no. 6, pp. 3594-601, Jun. 2014.
- [55] P. R. Pudasaini *et al.*, "High performance top-gated multilayer WSe₂ field effect transistors," *Nanotechnology*, vol. 28, no. 47, p. 475202, Nov. 2017.
- [56] C. Gong *et al.*, "Electronic and Optoelectronic Applications Based on 2D Novel Anisotropic Transition Metal Dichalcogenides," *Adv. Sci.*, vol. 4, no. 12, p. 1700231, Dec. 2017.
- [57] B. W. Baugher, H. O. Churchill, Y. Yang, and P. Jarillo-Herrero, "Optoelectronic devices based on electrically tunable p-n diodes in a monolayer dichalcogenide," *Nat. Nanotechnol.*, vol. 9, no. 4, pp. 262-7, Apr. 2014.
- [58] R. Cheng *et al.*, "Electroluminescence and photocurrent generation from atomically sharp WSe₂/MoS₂ heterojunction p-n diodes," *Nano Lett.*, vol. 14, no. 10, pp. 5590-7, Oct. 2014.
- [59] W. Choi *et al.*, "High-detectivity multilayer MoS₂ phototransistors with spectral response from ultraviolet to infrared," *Adv. Mater.*, vol. 24, no. 43, pp. 5832-6, Nov. 2012.
- [60] J. Ronn *et al.*, "Ultra-high on-chip optical gain in erbium-based hybrid slot waveguides," *Nat. Commun.*, vol. 10, p. 432, Jan. 2019.
- [61] A. Autere *et al.*, "Optical harmonic generation in monolayer group-VI transition metal dichalcogenides," *Phys. Rev. B*, vol. 98, no. 11, p. 115426, Sep. 2018.
- [62] S. Li *et al.*, "Vapour-liquid-solid growth of monolayer MoS₂ nanoribbons," *Nat. Mater.*, vol. 17, no. 6, pp. 535-42, Jun. 2018.
- [63] J. Liang *et al.*, "Monitoring Local Strain Vector in Atomic-Layered MoSe₂ by Second-Harmonic Generation," *Nano Lett.*, vol. 17, no. 12, pp. 7539-43, Dec. 2017.
- [64] D. Hu *et al.*, "Probing optical anisotropy of nanometer-thin van der waals microcrystals by near-field imaging," *Nat. Commun.*, vol. 8, no. 1, p. 1471, Nov. 2017.

- [65] A. Saynatjoki *et al.*, "Ultra-strong nonlinear optical processes and trigonal warping in MoS₂ layers," *Nat. Commun.*, vol. 8, no. 1, p. 893, Oct. 2017.
- [66] J. D. Yin *et al.*, "Large-area highly crystalline WSe₂ atomic layers for ultrafast pulsed lasers," *Opt. Express*, vol. 25, no. 24, pp. 30020-31, Nov. 2017.
- [67] H. Chen *et al.*, "Transition-metal dichalcogenides heterostructure saturable absorbers for ultrafast photonics," *Opt. Lett.*, vol. 42, no. 21, pp. 4279-82, Nov. 2017.
- [68] G. Hu *et al.*, "Black phosphorus ink formulation for inkjet printing of optoelectronics and photonics," *Nat. Commun.*, vol. 8, no. 1, Aug. 2017.
- [69] H. Yang *et al.*, "Optical Waveplates Based on Birefringence of Anisotropic Two-Dimensional Layered Materials," *ACS Photonics*, vol. 4, no. 12, pp. 3023-30, Dec. 2017.
- [70] L. Karvonen *et al.*, "Rapid visualization of grain boundaries in monolayer MoS₂ by multiphoton microscopy," *Nat. Commun.*, vol. 8, p. 15714, Jun. 2017.
- [71] A. Autere *et al.*, "Rapid and Large-Area Characterization of Exfoliated Black Phosphorus Using Third-Harmonic Generation Microscopy," *J. Phys. Chem. Lett.*, vol. 8, no. 7, pp. 1343-50, Apr. 2017.
- [72] P. Yan *et al.*, "Large-area tungsten disulfide for ultrafast photonics," *Nanoscale*, vol. 9, no. 5, pp. 1871-7, Feb. 2017.
- [73] D. Mao *et al.*, "Ultrafast all-fiber based cylindrical-vector beam laser," *Appl. Phys. Lett.*, vol. 110, no. 2, p. 021107, Jan. 2017.
- [74] D. Li *et al.*, "Black phosphorus polycarbonate polymer composite for pulsed fibre lasers," *Appl. Mater. Today*, vol. 4, pp. 17-23, Sep. 2016.
- [75] Z. Q. Luo *et al.*, "Two-dimensional material-based saturable absorbers: towards compact visible-wavelength all-fiber pulsed lasers," *Nanoscale*, vol. 8, no. 2, pp. 1066-72, Nov. 2016.
- [76] D. A. Li *et al.*, "Polarization and Thickness Dependent Absorption Properties of Black Phosphorus: New Saturable Absorber for Ultrafast Pulse Generation," *Sci. Rep.*, vol. 5, p. 15899, Oct. 2015.
- [77] F. Bonaccorso and Z. P. Sun, "Solution processing of graphene, topological insulators and other 2d crystals for ultrafast photonics," *Opt. Mater. Express*, vol. 4, no. 1, pp. 63-78, Jan. 2014.
- [78] M. H. Chiu *et al.*, "Determination of band alignment in the single-layer MoS₂/WSe₂ heterojunction," *Nat. Commun.*, vol. 6, p. 7666, Jul. 2015.
- [79] C. Huang *et al.*, "Lateral heterojunctions within monolayer MoSe₂-WSe₂ semiconductors," *Nat. Mater.*, vol. 13, no. 12, pp. 1096-101, Dec. 2014.
- [80] A. K. Geim and I. V. Grigorieva, "Van der Waals heterostructures," *Nature*, vol. 499, no. 7459, pp. 419-25, Jul. 2013.
- [81] V. O. Ozcelik, J. G. Azadani, C. Yang, S. J. Koester, and T. Low, "Band alignment of two-dimensional semiconductors for designing heterostructures with momentum space matching," *Phys. Rev. B*, vol. 94, no. 3, p. 035125, Jul. 2016.
- [82] Y. Guo and J. Robertson, "Band engineering in transition metal dichalcogenides: Stacked versus lateral heterostructures," *Appl. Phys. Lett.*, vol. 108, no. 23, p. 233104, Jun. 2016.
- [83] J. Shim *et al.*, "Recent progress in Van der Waals (vdW) heterojunction-based electronic and optoelectronic devices," *Carbon*, vol. 133, pp. 78-89, Mar. 2018.
- [84] W. Xia *et al.*, "Recent progress in van der Waals heterojunctions," *Nanoscale*, vol. 9, no. 13, pp. 4324-65, Mar. 2017.
- [85] Q. Zeng and Z. Liu, "Novel Optoelectronic Devices: Transition-Metal-Dichalcogenide-Based 2D Heterostructures," *Adv. Electron. Mater.*, vol. 4, no. 2, p. 1700335, Jan. 2018.
- [86] M. Long *et al.*, "Broadband Photovoltaic Detectors Based on an Atomically Thin Heterostructure," *Nano Lett.*, vol. 16, no. 4, pp. 2254-9, Apr. 2016.
- [87] Z. Wang *et al.*, "Electrostatically tunable lateral MoTe₂ p-n junction for use in high-performance optoelectronics," *Nanoscale*, vol. 8, no. 27, pp. 13245-50, Jul. 2016.
- [88] Y. Xue *et al.*, "Scalable Production of a Few-Layer MoS₂/WS₂ Vertical Heterojunction Array and Its Application for Photodetectors," *ACS Nano*, vol. 10, no. 1, pp. 573-80, Jan. 2016.

- [89] T. Yang *et al.*, "Van der Waals epitaxial growth and optoelectronics of large-scale WSe₂/SnS₂ vertical bilayer p-n junctions," *Nat. Commun.*, vol. 8, no. 1, p. 1906, Dec. 2017.
- [90] M. Long, P. Wang, H. Fang, and W. Hu, "Progress, Challenges, and Opportunities for 2D Material Based Photodetectors," *Adv. Funct. Mater.*, p. 1803807, Sep. 2018.
- [91] H. Xue *et al.*, "A MoSe₂/WSe₂ Heterojunction-Based Photodetector at Telecommunication Wavelengths," *Adv. Funct. Mater.*, p. 1804388, Sep. 2018.
- [92] R. Peierls, "Quelques propriétés typiques des corps solides," in *Ann. Henri Poincaré*, 1935, vol. 5, no. 3, pp. 177-222.
- [93] J. Hass, W. A. de Heer, and E. H. Conrad, "The growth and morphology of epitaxial multilayer graphene," *J. Phys. Condens. Matter*, vol. 20, no. 32, p. 323202, Aug. 2008.
- [94] A. H. Castro Neto, F. Guinea, N. M. R. Peres, K. S. Novoselov, and A. K. Geim, "The electronic properties of graphene," *Rev. Mod. Phys.*, vol. 81, no. 1, pp. 109-62, Jan. 2009.
- [95] A. Bablich, S. Kataria, and M. Lemme, "Graphene and Two-Dimensional Materials for Optoelectronic Applications," *Electronics*, vol. 5, no. 4, Mar. 2016.
- [96] C. Dean *et al.*, "Graphene based heterostructures," *Solid State Commun.*, vol. 152, no. 15, pp. 1275-82, May 2012.
- [97] J. Kim *et al.*, "Highly Sensitive, Gate-Tunable, Room-Temperature Mid-Infrared Photodetection Based on Graphene-Bi₂Se₃ Heterostructure," *ACS Photonics*, vol. 4, no. 3, pp. 482-8, Mar. 2017.
- [98] F. Schwierz, "Graphene transistors," *Nat. Nanotechnol.*, vol. 5, no. 7, p. 487, May 2010.
- [99] X. Li *et al.*, "Graphene and related two-dimensional materials: Structure-property relationships for electronics and optoelectronics," *Appl. Phys. Rev.*, vol. 4, no. 2, Jun. 2017.
- [100] Y. M. Lin *et al.*, "100-GHz transistors from wafer-scale epitaxial graphene," *Science*, vol. 327, no. 5966, p. 662, Feb. 2010.
- [101] X. Li and H. Zhu, "The graphene-semiconductor Schottky junction," *Phys. Today*, vol. 69, no. 9, pp. 46-51, Sep. 2016.
- [102] A. Allain, J. Kang, K. Banerjee, and A. Kis, "Electrical contacts to two-dimensional semiconductors," *Nat. Mater.*, vol. 14, no. 12, pp. 1195-205, Dec. 2015.
- [103] H. J. Chuang *et al.*, "Low-Resistance 2D/2D Ohmic Contacts: A Universal Approach to High-Performance WSe₂, MoS₂, and MoSe₂ Transistors," *Nano Lett.*, vol. 16, no. 3, pp. 1896-902, Mar. 2016.
- [104] M. M. Furchi, D. K. Polyushkin, A. Pospischil, and T. Mueller, "Mechanisms of photoconductivity in atomically thin MoS₂," *Nano Lett.*, vol. 14, no. 11, pp. 6165-70, Nov. 2014.
- [105] B. Radisavljevic, A. Radenovic, J. Brivio, V. Giacometti, and A. Kis, "Single-layer MoS₂ transistors," *Nat. Nanotechnol.*, vol. 6, no. 3, pp. 147-50, Mar. 2011.
- [106] N. Dong *et al.*, "Optical Limiting and Theoretical Modelling of Layered Transition Metal Dichalcogenide Nanosheets," *Sci. Rep.*, vol. 5, p. 14646, Sep. 2015.
- [107] K. F. Mak, C. Lee, J. Hone, J. Shan, and T. F. Heinz, "Atomically Thin MoS₂: A New Direct-Gap Semiconductor," *Phys. Rev. Lett.*, vol. 105, no. 13, p. 136805, Sep. 2010.
- [108] A. Kuc, N. Zibouche, and T. Heine, "Influence of quantum confinement on the electronic structure of the transition metal sulfide TS₂," *Phys. Rev. B*, vol. 83, no. 24, p. 245213, Jun. 2011.
- [109] P. Tonndorf *et al.*, "Photoluminescence emission and Raman response of monolayer MoS₂, MoSe₂, and WSe₂," *Opt. Express*, vol. 21, no. 4, pp. 4908-16, Feb. 2013.
- [110] S. Das, M. Demarteau, and A. Roelofs, "Nb-doped single crystalline MoS₂ field effect transistor," *Appl. Phys. Lett.*, vol. 106, no. 17, p. 173506, Apr. 2015.
- [111] S. Lin *et al.*, "Gate tunable monolayer MoS₂/InP heterostructure solar cells," *Appl. Phys. Lett.*, vol. 107, no. 15, p. 153904, Oct. 2015.
- [112] A. Abderrahmane, P. J. Ko, T. V. Thu, S. Ishizawa, T. Takamura, and A. Sandhu, "High photosensitivity few-layered MoSe₂ back-gated field-effect phototransistors," *Nanotechnology*, vol. 25, no. 36, p. 365202, Sep. 2014.
- [113] M. Fontana *et al.*, "Electron-hole transport and photovoltaic effect in gated MoS₂ Schottky junctions," *Sci. Rep.*, vol. 3, p. 1634, Apr. 2013.

- [114] A. Bolognesi, A. Di Carlo, and P. Lugli, "Influence of carrier mobility and contact barrier height on the electrical characteristics of organic transistors," *Appl. Phys. Lett.*, vol. 81, no. 24, pp. 4646-8, Dec. 2002.
- [115] W. Zhang, M.-H. Chiu, C.-H. Chen, W. Chen, L.-J. Li, and A. T. S. Wee, "Role of metal contacts in high-performance phototransistors based on WSe₂ monolayers," *ACS Nano*, vol. 8, no. 8, pp. 8653-61, Aug. 2014.
- [116] W. Liu, J. Kang, D. Sarkar, Y. Khatami, D. Jena, and K. Banerjee, "Role of metal contacts in designing high-performance monolayer n-type WSe₂ field effect transistors," *Nano Lett.*, vol. 13, no. 5, pp. 1983-90, May 2013.
- [117] J. Y. Lee, J. H. Shin, G. H. Lee, and C. H. Lee, "Two-Dimensional Semiconductor Optoelectronics Based on van der Waals Heterostructures," *Nanomater. (Basel)*, vol. 6, no. 11, Oct. 2016.
- [118] Z. Lin *et al.*, "2D materials advances: from large scale synthesis and controlled heterostructures to improved characterization techniques, defects and applications," *2D Mater.*, vol. 3, no. 4, p. 042001, Dec. 2016.
- [119] H. M. Hill, A. F. Rigosi, K. T. Rim, G. W. Flynn, and T. F. Heinz, "Band Alignment in MoS₂/WS₂ Transition Metal Dichalcogenide Heterostructures Probed by Scanning Tunneling Microscopy and Spectroscopy," *Nano Lett.*, vol. 16, no. 8, pp. 4831-7, Aug. 2016.
- [120] T. Roy, M. Tosun, M. Hettick, G. H. Ahn, C. Hu, and A. Javey, "2D-2D tunneling field-effect transistors using WSe₂/SnSe₂ heterostructures," *Appl. Phys. Lett.*, vol. 108, no. 8, p. 083111, Feb. 2016.
- [121] K. E. Aretouli *et al.*, "Epitaxial 2D SnSe₂/ 2D WSe₂ van der Waals Heterostructures," *ACS Appl. Mater. Interfaces*, vol. 8, no. 35, pp. 23222-29, Sep. 2016.
- [122] R. Yan *et al.*, "Esaki Diodes in van der Waals Heterojunctions with Broken-Gap Energy Band Alignment," *Nano Lett.*, vol. 15, no. 9, pp. 5791-8, Sep. 2015.
- [123] L. Esaki, M. Kitamura, S. Iwamoto, and Y. Arakawa, "Esaki diodes live and learn," *Proceedings Of the Japan Academy Series B-Physical And Biological Sciences*, vol. 86, no. 4, pp. 451-3, Apr. 2010.
- [124] A. Pant *et al.*, "Fundamentals of lateral and vertical heterojunctions of atomically thin materials," *Nanoscale*, vol. 8, no. 7, pp. 3870-87, Feb. 2016.
- [125] Z. Sun, A. Martinez, and F. Wang, "Optical modulators with 2D layered materials," *Nat. Photonics*, vol. 10, no. 4, pp. 227-38, Mar. 2016.
- [126] F. R. Yao *et al.*, "Measurement of complex optical susceptibility for individual carbon nanotubes by elliptically polarized light excitation," *Nat. Commun.*, vol. 9, p. 3387, Aug. 2018.
- [127] Q. C. Yuan *et al.*, "Low-Power Continuous-Wave Second Harmonic Generation in Semiconductor Nanowires," *Laser & Photonics Reviews*, vol. 12, no. 10, p. 1800126, Oct. 2018.
- [128] H. Yang *et al.*, "Nanowire network-based multifunctional all-optical logic gates," *Sci. Adv.*, vol. 4, no. 7, p. 7954, Jul. 2018.
- [129] M. M. Wang *et al.*, "172 fs, 24.3 kW peak power pulse generation from a Ho-doped fiber laser system," *Opt. Lett.*, vol. 43, no. 19, pp. 4619-22, Oct. 2018.
- [130] C. Li *et al.*, "Quiver-quenched optical-field-emission from carbon nanotubes," *Appl. Phys. Lett.*, vol. 111, no. 13, p. 133101, Sep. 2017.
- [131] K. F. Lee *et al.*, "Photon-Pair Generation with a 100 nm Thick Carbon Nanotube Film," *Adv. Mater.*, vol. 29, no. 24, p. 1605978, Jun. 2017.
- [132] T. Haggren *et al.*, "Nanowire encapsulation with polymer for electrical isolation and enhanced optical properties," *Nano Res.*, vol. 10, no. 8, pp. 2657-66, Aug. 2017.
- [133] J. Ronn *et al.*, "Atomic Layer Engineering of Er-Ion Distribution in Highly Doped Er:Al₂O₃ for Photoluminescence Enhancement," *ACS Photonics*, vol. 3, no. 11, pp. 2040-48, Nov. 2016.
- [134] S. Kujala, A. Mannila, L. Karvonen, K. Kieu, and Z. P. Sun, "Natural Silk as a Photonics Component: a Study on Its Light Guiding and Nonlinear Optical Properties," *Sci. Rep.*, vol. 6, p. 22358, Mar. 2016.

- [135] A. Autere *et al.*, "Slot waveguide ring resonators coated by an atomic layer deposited organic/inorganic nanolaminate," *Opt. Express*, vol. 23, no. 21, pp. 26940-51, Oct. 2015.
- [136] H. Yang *et al.*, "Broadband laser polarization control with aligned carbon nanotubes," *Nanoscale*, vol. 7, no. 25, pp. 11199-205, May 2015.
- [137] J. Z. Wang *et al.*, "Pulse dynamics in carbon nanotube mode-locked fiber lasers near zero cavity dispersion," *Opt. Express*, vol. 23, no. 8, pp. 9947-58, Apr. 2015.
- [138] T. Hasan *et al.*, "Double-Wall Carbon Nanotubes for Wide-Band, Ultrafast Pulse Generation," *ACS Nano*, vol. 8, no. 5, pp. 4836-47, May. 2014.
- [139] X. M. Liu *et al.*, "Versatile multi-wavelength ultrafast fiber laser mode-locked by carbon nanotubes," *Sci. Rep.*, vol. 3, Sep. 2013.
- [140] M. Zhang *et al.*, "Mid-infrared Raman-soliton continuum pumped by a nanotube-mode-locked sub-picosecond Tm-doped MOPFA," *Opt. Express*, vol. 21, no. 20, pp. 23261-71, Oct. 2013.
- [141] E. J. R. Kelleher *et al.*, "Generation and direct measurement of giant chirp in a passively mode-locked laser," *Opt. Lett.*, vol. 34, no. 22, pp. 3526-8, Nov. 2009.
- [142] E. J. R. Kelleher *et al.*, "Nanosecond-pulse fiber lasers mode-locked with nanotubes," *Appl. Phys. Lett.*, vol. 95, no. 11, p. 111108, Sep. 2009.
- [143] Z. Sun *et al.*, "L-band ultrafast fiber laser mode locked by carbon nanotubes," *Appl. Phys. Lett.*, vol. 93, no. 6, p. 061114, Aug. 2008.
- [144] F. Wang *et al.*, "Wideband-tuneable, nanotube mode-locked, fibre laser," *Nat. Nanotechnol.*, vol. 3, no. 12, pp. 738-42, Dec. 2008.
- [145] V. Scardaci *et al.*, "Carbon Nanotube Polycarbonate Composites for Ultrafast Lasers," *Adv. Mater.*, vol. 20, no. 21, pp. 4040-3, Nov. 2008.
- [146] J. P. Kakko *et al.*, "Measurement of Nanowire Optical Modes Using Cross-Polarization Microscopy," *Sci. Rep.*, vol. 7, p. 17790, Dec. 2017.
- [147] F. Bonaccorso, A. Lombardo, T. Hasan, Z. Sun, L. Colombo, and A. C. Ferrari, "Production and processing of graphene and 2d crystals," *Mater. Today*, vol. 15, no. 12, pp. 564-89, Dec. 2012.
- [148] H. Tan, Y. Fan, Y. Zhou, Q. Chen, W. Xu, and J. H. Warner, "Ultrathin 2D Photodetectors Utilizing Chemical Vapor Deposition Grown WS₂ With Graphene Electrodes," *ACS Nano*, vol. 10, no. 8, pp. 7866-73, Aug. 2016.
- [149] Y. Gong *et al.*, "Two-Step Growth of Two-Dimensional WSe₂/MoSe₂ Heterostructures," *Nano Lett.*, vol. 15, no. 9, pp. 6135-41, Sep. 2015.
- [150] C. Jung *et al.*, "Highly Crystalline CVD-grown Multilayer MoSe₂ Thin Film Transistor for Fast Photodetector," *Sci. Rep.*, vol. 5, p. 15313, Oct. 2015.
- [151] K. Liu *et al.*, "Elastic properties of chemical-vapor-deposited monolayer MoS₂, WS₂, and their bilayer heterostructures," *Nano Lett.*, vol. 14, no. 9, pp. 5097-103, Sep. 2014.
- [152] W. Kim, "Fabrication and characterization of graphene-based electronic devices," 2015.
- [153] J. R. Brent, N. Savjani, and P. O'Brien, "Synthetic approaches to two-dimensional transition metal dichalcogenide nanosheets," *Prog. Mater. Sci.*, vol. 89, pp. 411-78, Jun. 2017.
- [154] S. Das, M. Kim, J.-w. Lee, and W. Choi, "Synthesis, Properties, and Applications of 2-D Materials: A Comprehensive Review," *Crit. Rev. Solid State Materials Sci.*, vol. 39, no. 4, pp. 231-52, Apr. 2014.
- [155] S. A. Han, R. Bhatia, and S.-W. Kim, "Synthesis, properties and potential applications of two-dimensional transition metal dichalcogenides," *Nano Convergence*, vol. 2, no. 1, Sep. 2015.
- [156] F. Wang *et al.*, "Synthesis, properties and applications of 2D non-graphene materials," *Nanotechnology*, vol. 26, no. 29, p. 292001, Jul. 2015.
- [157] S. Manzeli, D. Ovchinnikov, D. Pasquier, O. V. Yazyev, and A. Kis, "2D transition metal dichalcogenides," *Nature Reviews Materials*, vol. 2, no. 8, p. 17033, 2017.
- [158] D. Dumcenco *et al.*, "Large-Area Epitaxial Monolayer MoS₂," *ACS Nano*, vol. 9, no. 4, pp. 4611-20, Apr. 2015.
- [159] O. Lehtinen *et al.*, "Atomic scale microstructure and properties of Se-deficient two-dimensional MoSe₂," *ACS Nano*, vol. 9, no. 3, pp. 3274-83, Mar. 2015.

- [160] R. Lv *et al.*, "Transition Metal Dichalcogenides and Beyond: Synthesis, Properties, and Applications of Single- and Few-Layer Nanosheets," *Acc. Chem. Res.*, vol. 48, no. 1, pp. 56-64, Jan. 2015.
- [161] J. Wang, G. Li, and L. Li, "Synthesis Strategies about 2D Materials," in *Two-dimensional Materials - Synthesis, Characterization and Potential Applications*, 2016.
- [162] S. F. Wu, C. M. Huang, G. Aivazian, J. S. Ross, D. H. Cobden, and X. D. Xu, "Vapor-Solid Growth of High Optical Quality MoS₂ Monolayers with Near-Unity Valley Polarization," *ACS Nano*, vol. 7, no. 3, pp. 2768-2772, Mar. 2013.
- [163] M. W. Chen *et al.*, "Highly Oriented Atomically Thin Ambipolar MoSe₂ Grown by Molecular Beam Epitaxy," *ACS Nano*, vol. 11, no. 6, pp. 6355-61, Jun. 2017.
- [164] H. G. Kim and H.-B.-R. Lee, "Atomic Layer Deposition on 2D Materials," *Chem. Mater.*, vol. 29, no. 9, pp. 3809-26, Apr. 2017.
- [165] W. Choi, N. Choudhary, G. H. Han, J. Park, D. Akinwande, and Y. H. Lee, "Recent development of two-dimensional transition metal dichalcogenides and their applications," *Materials Today*, vol. 20, no. 3, pp. 116-130, 2017.
- [166] R. Saito, Y. Tatsumi, S. Huang, X. Ling, and M. S. Dresselhaus, "Raman spectroscopy of transition metal dichalcogenides," *J. Phys. Condens. Matter*, vol. 28, no. 35, p. 353002, Sep. 2016.
- [167] L. M. Malard, M. A. Pimenta, G. Dresselhaus, and M. S. Dresselhaus, "Raman spectroscopy in graphene," *Phys. Rep.*, vol. 473, no. 5-6, pp. 51-87, Mar. 2009.
- [168] A. Tiberj and J. Camassel, "Raman Imaging in Semiconductor Physics: Applications to Microelectronic Materials and Devices," in *Raman Imaging* (Springer Series in Optical Sciences, 2012, pp. 39-83.
- [169] W. Shi, M.-L. Lin, Q.-H. Tan, X.-F. Qiao, J. Zhang, and P.-H. Tan, "Raman and photoluminescence spectra of two-dimensional nanocrystallites of monolayer WS₂ and WSe₂," *2D Mater.*, vol. 3, no. 2, p. 025016, Apr. 2016.
- [170] F. Giubileo *et al.*, "Contact Resistance and Channel Conductance of Graphene Field-Effect Transistors under Low-Energy Electron Irradiation," *Nanomater. (Basel)*, vol. 6, no. 11, Nov. 2016.
- [171] J. A. Robinson *et al.*, "Contacting graphene," *Appl. Phys. Lett.*, vol. 98, no. 5, p. 053103, Feb. 2011.
- [172] Y. Xu *et al.*, "Contacts between Two- and Three-Dimensional Materials: Ohmic, Schottky, and p-n Heterojunctions," *ACS Nano*, vol. 10, no. 5, pp. 4895-919, May 2016.
- [173] Z. Zhang and J. T. Yates, Jr., "Band bending in semiconductors: chemical and physical consequences at surfaces and interfaces," *Chem. Rev.*, vol. 112, no. 10, pp. 5520-51, Oct. 2012.
- [174] G. Konstantatos and E. H. Sargent, "Nanostructured materials for photon detection," *Nat. Nanotechnol.*, vol. 5, no. 6, pp. 391-400, Jun. 2010.
- [175] C. Xie, C. Mak, X. Tao, and F. Yan, "Photodetectors Based on Two-Dimensional Layered Materials Beyond Graphene," *Adv. Funct. Mater.*, vol. 27, no. 19, p. 1603886, Nov. 2017.
- [176] M. Buscema *et al.*, "Photocurrent generation with two-dimensional van der Waals semiconductors," *Chem. Soc. Rev.*, vol. 44, no. 11, pp. 3691-718, Jun. 2015.
- [177] B. Nabet, A. Cola, A. Cataldo, X. Y. Chen, and F. Quaranta, "Photodetectors based on heterostructures for optoelectronic applications," *IEEE Trans. Microw. Theory Tech.*, vol. 49, pp. 306-16, Jul. 2002.
- [178] Y. Li, C. Y. Xu, J. Y. Wang, and L. Zhen, "Photodiode-like behavior and excellent photoresponse of vertical Si/monolayer MoS₂ heterostructures," *Sci. Rep.*, vol. 4, p. 7186, Nov. 2014.
- [179] D. J. Groenendijk *et al.*, "Photovoltaic and photothermoelectric effect in a double-gated WSe₂ device," *Nano Lett.*, vol. 14, no. 10, pp. 5846-52, Oct. 2014.
- [180] F. W. Zhuge *et al.*, "Nanostructured Materials and Architectures for Advanced Infrared Photodetection," *Adv. Mater. Technol.*, vol. 2, no. 8, p. 1700005, Aug. 2017.
- [181] Q. S. Wang, J. W. Lai, and D. Sun, "Review of photo response in semiconductor transition metal

- dichalcogenides based photosensitive devices," *Opt. Mater. Express*, vol. 6, no. 7, pp. 2313-27, Jul. 2016.
- [182] M. Buscema, D. J. Groenendijk, G. A. Steele, H. S. van der Zant, and A. Castellanos-Gomez, "Photovoltaic effect in few-layer black phosphorus PN junctions defined by local electrostatic gating," *Nat. Nanotechnol.*, vol. 5, no. Nat. Commun., p. 4651, Aug. 2014.
- [183] J. Boguslawski *et al.*, "Graphene Actively Mode-Locked Lasers," *Adv. Funct. Mater.*, vol. 28, no. 28, p. 1801539, May 2018.
- [184] J. F. Liu *et al.*, "Ge-on-Si optoelectronics," *Thin Solid Films*, vol. 520, no. 8, pp. 3354-60, Feb. 2012.
- [185] X. Sun *et al.*, "High spectral response of self-driven GaN-based detectors by controlling the contact barrier height," *Sci. Rep.*, vol. 5, no. 1, p. 16819, Nov. 2015.
- [186] F. Ceballos, M. Z. Bellus, H. Y. Chiu, and H. Zhao, "Probing charge transfer excitons in a MoSe₂-WS₂ van der Waals heterostructure," *Nanoscale*, vol. 7, no. 41, pp. 17523-8, Nov. 2015.
- [187] A. Nourbakhsh, A. Zubair, M. S. Dresselhaus, and T. Palacios, "Transport Properties of a MoS₂/WSe₂ Heterojunction Transistor and Its Potential for Application," *Nano Lett.*, vol. 16, no. 2, pp. 1359-66, Feb. 2016.
- [188] P. Rivera *et al.*, "Observation of long-lived interlayer excitons in monolayer MoSe₂-WSe₂ heterostructures," *Nat. Commun.*, vol. 6, p. 6242, 2015.
- [189] Y. Son *et al.*, "Observation of Switchable Photoresponse of a Monolayer WSe₂-MoS₂ Lateral Heterostructure via Photocurrent Spectral Atomic Force Microscopic Imaging," *Nano Lett.*, vol. 16, no. 6, pp. 3571-7, Jun. 2016.
- [190] S. Tongay *et al.*, "Tuning interlayer coupling in large-area heterostructures with CVD-grown MoS₂ and WS₂ monolayers," *Nano Lett.*, vol. 14, no. 6, pp. 3185-90, Jun. 2014.
- [191] P. Vabbina *et al.*, "Highly sensitive wide bandwidth photodetector based on internal photoemission in CVD grown p-type MoS₂/graphene Schottky junction," *ACS Appl. Mater. Interfaces*, vol. 7, no. 28, pp. 15206-13, Jul. 2015.
- [192] V. O. Ozcelik, J. G. Azadani, C. Yang, S. J. Koester, and T. Low, "Band alignment of two-dimensional semiconductors for designing heterostructures with momentum space matching," *Phys. Rev. B*, vol. 94, no. 3, Jul. 2016.
- [193] A. Autere, H. Jussila, Y. Dai, Y. Wang, H. Lipsanen, and Z. Sun, "Nonlinear Optics with 2D Layered Materials," *Adv. Mater.*, p. 1705963, 2018.
- [194] X. Yang *et al.*, "Nanomaterial-Based Plasmon-Enhanced Infrared Spectroscopy," *Adv Mater*, vol. 30, no. 20, p. e1704896, May 2018.
- [195] F. Ceballos, M. Z. Bellus, H. Y. Chiu, and H. Zhao, "Ultrafast charge separation and indirect exciton formation in a MoS₂-MoSe₂ van der Waals heterostructure," *ACS Nano*, vol. 8, no. 12, pp. 12717-24, Dec. 2014.
- [196] K. Swaminathan, T. J. Grassman, L. M. Yang, Q. Gu, M. J. Mills, and S. A. Ringel, "Optically-aligned visible/near-infrared dual-band photodetector materials and devices on GaAs using metamorphic epitaxy," *J. Appl. Phys.*, vol. 110, no. 6, Sep. 2011.
- [197] G. Wang *et al.*, "Interlayer Coupling Induced Infrared Response in WS₂/MoS₂ Heterostructures Enhanced by Surface Plasmon Resonance," *Adv. Funct. Mater.*, p. 1800339, 2018.
- [198] K. Zhang *et al.*, "Interlayer Transition and Infrared Photodetection in Atomically Thin Type-II MoTe₂/MoS₂ van der Waals Heterostructures," *ACS Nano*, vol. 10, no. 3, pp. 3852-8, Mar. 2016.
- [199] J. Kang, S. Tongay, J. Zhou, J. Li, and J. Wu, "Band offsets and heterostructures of two-dimensional semiconductors," *Appl. Phys. Lett.*, vol. 102, no. 1, p. 012111, Jan. 2013.
- [200] F. H. Koppens, T. Mueller, P. Avouris, A. C. Ferrari, M. S. Vitiello, and M. Polini, "Photodetectors based on graphene, other two-dimensional materials and hybrid systems," *Nat. Nanotechnol.*, vol. 9, no. 10, pp. 780-93, Oct. 2014.
- [201] X. Wei, F.-G. Yan, C. Shen, Q.-S. Lv, and K.-Y. Wang, "Photodetectors based on junctions of two-dimensional transition metal dichalcogenides," *Chinese Phys. B*, vol. 26, no. 3, p. 038504, Feb. 2017.

- [202] Z. Lou, Z. Liang, and G. Shen, "Photodetectors based on two dimensional materials," *J. Semiconductors*, vol. 37, no. 9, Sep. 2016.
- [203] X. Wang, Z. Cheng, K. Xu, H. K. Tsang, and J.-B. Xu, "High-responsivity graphene/silicon-heterostructure waveguide photodetectors," *Nat. Photonics*, vol. 7, no. 11, pp. 888-91, Sep. 2013.
- [204] Y.-Q. Yu *et al.*, "High-speed ultraviolet-visible-near infrared photodiodes based on p-ZnS nanoribbon-n-silicon heterojunction," *CrystEngComm*, vol. 15, no. 8, pp. 1635-42, Nov. 2013.
- [205] J. S. Jie, W. J. Zhang, Y. Jiang, X. M. Meng, Y. Q. Li, and S. T. Lee, "Photoconductive characteristics of single-crystal CdS nanoribbons," *Nano Lett.*, vol. 6, no. 9, pp. 1887-92, Sep. 2006.
- [206] M. Casalino, G. Coppola, M. Iodice, I. Rendina, and L. Sirleto, "Near-infrared sub-bandgap all-silicon photodetectors: state of the art and perspectives," *Sensors (Basel)*, vol. 10, no. 12, pp. 10571-600, Nov. 2010.
- [207] A. Sharma, A. K. Srivastava, T. D. Senguttuvan, and S. Husale, "Robust broad spectral photodetection (UV-NIR) and ultra high responsivity investigated in nanosheets and nanowires of Bi₂Te₃ under harsh nano-milling conditions," *Sci. Rep.*, vol. 7, no. 1, p. 17911, Dec. 2017.
- [208] T. Mueller, F. Xia, and P. Avouris, "Graphene photodetectors for high-speed optical communications," *Nat. Photon.*, vol. 4, no. 5, pp. 297-301, 2010.
- [209] J. Yao, Z. Zheng, and G. Yang, "Layered-material WS₂/topological insulator Bi₂Te₃ heterostructure photodetector with ultrahigh responsivity in the range from 370 to 1550 nm," *J. Mater. Chem. C*, vol. 4, no. 33, pp. 7831-40, Jul. 2016.
- [210] H. Li, L. Ye, and J. B. Xu, "High-Performance Broadband Floating-Base Bipolar Phototransistor Based on WSe₂/BP/MoS₂ Heterostructure," *ACS Photon.*, vol. 4, no. 4, pp. 823-829, Apr. 2017.
- [211] S. H. Gu *et al.*, "Self-driven, broadband and ultrafast photovoltaic detectors based on topological crystalline insulator SnTe/Si heterostructures," *J. Mater. Chem. A*, vol. 5, no. 22, pp. 11171-8, Jun. 2017.
- [212] M. Engel, M. Steiner, and P. Avouris, "Black Phosphorus Photodetector for Multispectral, High-Resolution Imaging," *Nano Lett.*, vol. 14, no. 11, pp. 6414-6417, Nov. 2014.
- [213] N. Youngblood, C. Chen, S. J. Koester, and M. Li, "Waveguide-integrated black phosphorus photodetector with high responsivity and low dark current," *Nat. Photon.*, vol. 9, no. 4, pp. 247-252, Apr. 2015.
- [214] C. Lan *et al.*, "Zener Tunneling and Photoresponse of a WS₂/Si van der Waals Heterojunction," *ACS Appl. Mater. Interfaces*, vol. 8, no. 28, pp. 18375-82, Jul. 2016.
- [215] X. Zhou *et al.*, "Tunneling Diode Based on WSe₂/SnS₂ Heterostructure Incorporating High Detectivity and Responsivity," *Adv. Mater.*, vol. 30, no. 7, p. 1703286, Feb. 2018.
- [216] Q. A. Vu *et al.*, "Tuning Carrier Tunneling in van der Waals Heterostructures for Ultrahigh Detectivity," *Nano Lett.*, vol. 17, no. 1, pp. 453-9, Jan. 2017.
- [217] C. Li *et al.*, "WSe₂/MoS₂ and MoTe₂/SnSe₂ van der Waals heterostructure transistors with different band alignment," *Nanotechnology*, vol. 28, no. 41, p. 415201, Oct. 2017.
- [218] M. Li, D. Esseni, J. J. Nahas, D. Jena, and H. G. Xing, "Two-Dimensional Heterojunction Interlayer Tunneling Field Effect Transistors (Thin-TFETs)," *IEEE Trans. Electron Devices*, vol. 3, no. 3, pp. 206-13, May 2015.
- [219] J. I. Pankove, *Optical processes in semiconductors* (Prentice-Hall electrical engineering series). Englewood Cliffs, N.J: Prentice Hall: Prentice-Hall, **1971**.
- [220] O. Lopez-Sanchez, D. Lembke, M. Kayci, A. Radenovic, and A. Kis, "Ultrasensitive photodetectors based on monolayer MoS₂," *Nat. Nanotechnol.*, vol. 8, no. 7, pp. 497-501, Jul. 2013.
- [221] D. Kufer and G. Konstantatos, "Highly Sensitive, Encapsulated MoS₂ Photodetector with Gate Controllable Gain and Speed," *Nano Lett.*, vol. 15, no. 11, pp. 7307-13, Nov. 2015.
- [222] D. H. Kang *et al.*, "High-Performance Transition Metal Dichalcogenide Photodetectors Enhanced by Self-Assembled Monolayer Doping," *Adv. Funct. Mater.*, vol. 25, no. 27, pp. 4219-27, Jul. 2015.

- [223] Y. Jin, D. H. Keum, S. J. An, J. Kim, H. S. Lee, and Y. H. Lee, "A Van Der Waals Homo Junction: Ideal p-n Diode Behavior in MoSe₂," *Adv. Mater.*, vol. 27, no. 37, pp. 5534-40, Oct. 2015.
- [224] M. Sun *et al.*, "Novel Transfer Behaviors in 2D MoS₂/WSe₂ Heterotransistor and Its Applications in Visible-Near Infrared Photodetection," *Adv. Electron. Mater.*, vol. 3, p. 1600502, 2017.
- [225] F. Wang *et al.*, "Tunable GaTe-MoS₂ van der Waals p-n Junctions with Novel Optoelectronic Performance," *Nano Lett.*, vol. 15, no. 11, pp. 7558-66, Nov. 2015.
- [226] X. Wang *et al.*, "Enhanced rectification, transport property and photocurrent generation of multilayer ReSe₂/MoS₂ p-n heterojunctions," *Nano Res.*, vol. 9, no. 2, pp. 507-516, 2015.
- [227] M. Moun, M. Kumar, M. Garg, R. Pathak, and R. Singh, "Understanding of MoS₂/GaN Heterojunction Diode and its Photodetection Properties," *Sci. Rep.*, vol. 8, no. 1, p. 11799, Aug. 2018.
- [228] N. R. Pradhan *et al.*, "High Photoresponsivity and Short Photoresponse Times in Few-Layered WSe₂ Transistors," *ACS Appl. Mater. Interfaces*, vol. 7, no. 22, pp. 12080-8, Jun. 2015.
- [229] C. Y. Lan *et al.*, "Highly responsive and broadband photodetectors based on WS₂-graphene van der Waals epitaxial heterostructures," *J. Mater. Chem. C*, vol. 5, no. 6, pp. 1494-500, Feb. 2017.
- [230] J. Shim *et al.*, "High-Performance 2D Rhenium Disulfide (ReS₂) Transistors and Photodetectors by Oxygen Plasma Treatment," *Adv. Mater.*, vol. 28, no. 32, pp. 6985-92, Aug. 2016.
- [231] E. F. Liu *et al.*, "High Responsivity Phototransistors Based on Few-Layer ReS₂ for Weak Signal Detection," *Adv. Funct. Mater.*, vol. 26, no. 12, pp. 1938-44, Mar. 2016.
- [232] M. Huang *et al.*, "Broadband Black-Phosphorus Photodetectors with High Responsivity," *Adv. Mater.*, vol. 28, no. 18, pp. 3481-5, May 2016.
- [233] S. X. Yang *et al.*, "Layer-dependent electrical and optoelectronic responses of ReSe₂ nanosheet transistors," *Nanoscale*, vol. 6, no. 13, pp. 7226-31, May 2014.
- [234] Q. Lv, F. Yan, X. Wei, and K. Wang, "High-Performance, Self-Driven Photodetector Based on Graphene Sandwiched GaSe/WS₂ Heterojunction," *Adv. Opt. Mater.*, vol. 6, no. 2, p. 1700490, Oct. 2018.
- [235] Q. Guo *et al.*, "Black Phosphorus Mid-Infrared Photodetectors with High Gain," *Nano Lett.*, vol. 16, no. 7, pp. 4648-55, Jul. 2016.
- [236] L. Ye *et al.*, "Highly polarization sensitive infrared photodetector based on black phosphorus-on-WSe₂ photogate vertical heterostructure," *Nano Energy*, vol. 37, pp. 53-60, Jul. 2017.
- [237] H. Qiao *et al.*, "Broadband Photodetectors Based on Graphene-Bi₂Te₃ Heterostructure," *ACS Nano*, vol. 9, no. 2, pp. 1886-94, Feb. 2015.
- [238] D. Kufer, I. Nikitskiy, T. Lasanta, G. Navickaite, F. H. Koppens, and G. Konstantatos, "Hybrid 2D-oD MoS₂-PbS quantum dot photodetectors," *Adv. Mater.*, vol. 27, no. 1, pp. 176-80, Jan. 2015.
- [239] L. Ye, H. Li, Z. Chen, and J. Xu, "Near-Infrared Photodetector Based on MoS₂/Black Phosphorus Heterojunction," *ACS Photonics*, vol. 3, no. 4, pp. 692-9, Mar. 2016.
- [240] R. Mas-Balleste, C. Gomez-Navarro, J. Gomez-Herrero, and F. Zamora, "2D materials: to graphene and beyond," *Nanoscale*, vol. 3, no. 1, pp. 20-30, Jan. 2011.
- [241] R. K. Joshi, M. Yoshimura, and A. Kumar, "Graphene," *J. Nanomater.*, 2010.



ISBN 978-952-60-8894-5 (printed)

ISBN 978-952-60-8895-2 (pdf)

ISSN 1799-4934 (printed)

ISSN 1799-4942 (pdf)

Aalto University
School of Electrical Engineering
Department of Electronics and Nanoengineering
www.aalto.fi

**BUSINESS +
ECONOMY**

**ART +
DESIGN +
ARCHITECTURE**

**SCIENCE +
TECHNOLOGY**

CROSSOVER

**DOCTORAL
DISSERTATIONS**